PHASED ARRAY TECHNIQUE FOR BRAIN SOURCE LOCALIZATION

A THESIS IN ELECTRICAL ENGINEERING
Master of Science in Electrical Engineering

Presented to the faculty of the American University of Sharjah
College of Engineering
in partial fulfillment of
the requirements for the degree

MASTER OF SCIENCE

by

TAHEREH SADAT ZARGHAMI
B.S. 2008

Sharjah, UAE

January 2012

PHASED ARRAY TECHNIQUE FOR BRAIN

SOURCE LOCALIZATION

Tahereh Sadat Zarghami, Candidate for the Master of Science Degree

American University of Sharjah, 2012

ABSTRACT

Magnetoencephalography (MEG) and Electroencephalography (EEG) are two popular non-invasive techniques that *directly* measure the magnetic/electric signals generated from the brain's electrical activity, unlike functional measures such as fMRI, SPECT, and PET which reflect blood flow or brain metabolism.

Using appropriate volume conductor models for the head, one can theoretically obtain the electric/magnetic fields that would appear outside the scalp as a result of brain neural activity (modeled as current dipoles). This derivation of electric/magnetic fields is known as the *forward problem.* Finding a proper solution to the forward problem is the first step covered in this thesis.

The *inverse problem* on the other hand is locating the neural activity of the brain which has produced a specific set of measured electric potentials/magnetic fields. The inverse problem is widely known as an ill-posed one, with no unique solution. Moreover, there are major challenges in estimating cerebral sources from EEG/MEG recordings. The effect of physical parameters such as the thickness of skull, conductivity anisotropy, and inhomogeneity of the head affect EEG signals extensively. MEG readings, though

less affected by head geometry, are extremely weak and need expensive superconductive sensors and shielded rooms to be acquired.

This thesis shows the procedure used for obtaining appropriate forward solutions from the available and dedicated software, using various spherical and realistic head models. Further, to solve the inverse problem, a direction of arrival (DOA) technique recently used in RADAR field is adapted and applied to solving brain source localization problem. This is accomplished through the use of the ReIterative Super-Resolution (RISR) algorithm which is based on a recursive implementation of minimum mean-square error (MMSE) estimation. It is demonstrated that this algorithm can determine the model order, respective DOAs of sources, and their amplitudes from very few samples of data. Results show superior spatial resolution and robustness to correlation between sources. These are important features that are examined through extensive simulations using MEG and EEG data obtained from different head models developed on two different head anatomies. Moreover, the effect of skull thickness and conductivity variations on the localization is investigated for EEG signals. Finally, two calibration techniques have been applied to this algorithm, which improve the localization results in the presence of two types of calibration errors.

CONTENTS

LIST OF ILLUSTRATIONS

LIST OF TABLES

LIST OF ABBREVIATIONS

EEG	-	Electroencephalography
MEG	-	Magnetoencephalography
DOA	-	Direction of Arrival
MSE	-	Mean Square Error
SNR	-	Signal to Noise Ratio
RISR	-	Reiterative Super-Resolution Algorithm
SAFFIRE	-	Source Affine Image Reconstruction Algorithm
MUSIC	-	Multiple Signal Classification Algorithm

ACKNOWLEDGEMENTS

بسم الله الرحمن الرحيم

First I would like to thank God for blessing me in so many ways in my life. Then I would like to thank myself for having faith in me and trying hard to get what I want. I would also like to thank my parents for giving me the best education throughout my life, and cherishing my achievements. I want to express my gratitude towards all my teachers who taught me the fundamentals way before I came to university. And I want to thank my amazing professors in the Electrical Engineering Department of AUS for teaching me so well. My special thanks to Dr. Mohamed El-Tarhuni, Dr. Khaled Assaleh, Dr. Naser Qaddoumi, Dr. Hasan Mir, Dr. Hasan Al-Nashash, Dr. Mohamed Hassan, Dr. Lutfi Albasha, Dr. Aymen El-Hag, Dr. Rached Dhaouadi, Eng. Ibrahim Abu Saif, Eng. Wasil El-Tahir, and Eng. Narayanan for all they taught me throughout my Bachelors and Masters education. And thanks to the Electrical Engineering Department of AUS for granting me a generous assistantship package which supported my Masters education.

I also want to thank my dear friends, who made my experience at AUS a memorable one; my friends who supported me from near and far throughout my undergraduate and graduate studies at AUS. Thank you Omniyah Noory, Ayman Jundi, Yara Fayad, Rimas Zrae, Monireh Vamegh, Yasmin Hasan, Mai Ali, Sanabel AlNoorani, and all others. Your friendship made the difficult days much easier, and the good days much brighter.

Saving the best for last, I would like to thank my kind professors and advisors, Dr. Hasan Mir and Dr. Hasan Al-Nashash for all their help and support. Thank you Drs. for meeting with me every week for a year, responding to every email, checking every code, and reviewing every draft of my work. Thank you and God bless you.

To my parents who helped me get where I am.

CHAPTER 1

INTRODUCTION

In this chapter, the problem of brain source localization is introduced and some of the existing challenges in this field are explained. More specifically, the drawbacks of the currently used phased array techniques in this application are pointed out. Furthermore, the objective of this thesis and its contributions are summarized. Finally, the outline of this thesis is presented.

1.1 Brain source localization

The human brain and its functionality has always been an exciting topic for researchers. Various attempts have been made over the years to map the human brain function in healthy and impaired brains. Functional brain imaging is a multidisciplinary research that improves our understanding of the human brain through noninvasive imaging of the electrophysiological, hemodynamic, metabolic, and neuro-chemical processes that underlie normal and pathological brain function [1].

Clinical applications include improved understanding and treatment of serious neurological and neuropsychological disorders such as epilepsy, schizophrenia, depression, Parkinson's and Alzheimer's diseases [1]. Also, deep brain stimulation is a field that can benefit greatly from studies of brain functional imaging. Furthermore, localization of brain cells activities in different situations will help improve performance of Brain-Computer Interface (BCI) machines, which is another active field these days.

But none of these applications truly reflects the significance of understanding the brain, especially the human brain. Human brain is the most complex structure known to man. Together with the spinal cord and peripheral nerves, the brain makes up a complex, integrated information-processing and control system that governs virtually all our activities. It controls both involuntary (or "lower" actions) such as heart rate, respiration, and digestion, and also complex (or "higher" mental activity) such as thought, reason, and

abstraction. It should be clear by now why we are so enthusiastic about understanding our brains.

Neuroimaging includes the use of various techniques to image the structure and/or function of the brain [2]. Two popular noninvasive methods to study the brain signals are electroencephalography (EEG) and magnetoencephalography (MEG). To understand their principles of operation, we should know how brain signals are generated. In fact, the activity of brain neural cells produces small electric and magnetic fields in the brain. EEG measures the electric potential differences on the scalp, while MEG records very weak magnetic fields produced by neurons, outside the head. Both of these fields are created by the same neurophysiological events in the brain that will be explained in more detail later on in this thesis. Thus, spontaneous and evoked brain activities can be monitored non-invasively and in real time using MEG and EEG recorders

Neurons that produce the abovementioned electric and magnetic fields are usually modeled as current dipoles. Using proper volume conductor models for the head, one can obtain the electric/magnetic fields that appear on/outside the scalp as a result of such neural activity. Such derivation of electric/magnetic fields is known as the *forward problem.* The *inverse problem* on the other hand is when we have a specific set of measured electric/magnetic brain signals, and we are trying to locate the neural activity inside the brain that has resulted in these measured fields.

The inverse problem is widely known as an ill-posed one, with no unique solution. The reason is that, many source configurations can result in the same measured electric/magnetic fields. Hence, it's usually necessary to include a-priori knowledge about the current sources to constrain the solution. For example, one can start by assuming a specific number of dipolar sources within the brain [3]. Then, one has to determine the location, amplitude and orientation of each current dipole within the brain.

Several signal processing techniques have been suggested to accomplish the above, and the primary ones are mentioned in Chapter 4 of this thesis. These methods are divided into parametric and non-parametric approaches, each bearing its advantages and challenges. Moreover, in order to appreciate the concept and advantages of the algorithm utilized in this thesis for brain source localization, Chapter 5 is dedicated to explaining the principles of array signal processing.

1.2 Motivation and Problem Statement

Many high resolution direction of arrival (DOA) techniques (used for localization purposes) are based on the formation and exploitation of a sample covariance matrix (SCM). That is, when the signals originating from active sources impinge on an array of sensors, a set of spatial snapshots is collected from each array element. When these snapshots are put together in a matrix and the covariance of that matrix is formed, it is called the sample covariance matrix (SCM). In order for those DOA methods based on SCM to perform well, an accurate estimation of the SCM is required, which requires adequate number of snapshots (data samples). However, if the DOAs of the sources change very fast with time, the number of available data samples (sample support) is very limited. Hence, the estimated SCM in this case is less accurate, which in turn degrades the performance of the corresponding SCM-based methods. Moreover, SCM-based techniques don't perform well when there is temporal correlation between the sources, which happens in reality. They also require prior knowledge about the number of the underlying sources (model order). Other challenges faced in these techniques include high sensitivity to array modeling errors, and inability to provide information about the amplitude of the localized sources.

The objective of this thesis is to apply a phased array DOA technique to EEG/MEG brain signals and localize the underlying neural activity with higher spatial resolution, while tackling the common abovementioned challenges encountered in similar localization techniques.

1.3 Methodology

The methodology adopted in this thesis is explained in detail in CHAPTER 6. However, a general outline is provided here. First, literature review has been conducted to compare the existing software for the purpose of brain signal modeling. Certain criteria have been set for the appropriate software, and based on those, two dedicated software have been picked for solving the *forward problem* of brain signals. The neural activity of the brain has been modeled as *current dipoles* in a conductive medium. The head itself has been modeled as a sphere, concentric spheres, and a realistic head model derived

from boundary element methods, respectively. The arrays of sensors have been defined separately for EEG and MEG signals, based on actual devices available in the market. Next, certain parts of the brain were assumed to be active, and specific activity waveforms were assigned to them. Using the source and head models and making some restrictive assumptions, synthetic EEG and MEG signals were generated.

A high resolution phased array technique that originated in RADAR application has been investigated [4]. This algorithm has recently been adapted to the application of brain source localization using MEG signals [5]. The performance of this technique has been verified on synthetic MEG signals in this thesis. Moreover, the algorithm has been applied to artificial EEG signals. The localization results have been quantified in terms of probability of detection of a few proximate sources in the brain, and the mean square error (MSE) in localization, for different signal to noise ratio (SNR) values.

The effect of forward model uncertainties (in form of skull thickness and conductivity variations) on the source localization from EEG signals has also been examined for this technique. Furthermore, the effect of calibration errors on the performance of this method has been studied and two calibration techniques have been implemented to improve localization in presence of different forms of modeling errors.

Finally, the sources have been reconstructed in space and time and mapped onto the brain.

1.4 Thesis contribution and outline

In this thesis the performance of a phased array radar technique has been investigated for a biomedical application. Using this technique, proximate sources of activity within the brain have been localized with high spatial resolution from synthetic MEG and EEG signals. Different head models (spherical and realistic) have been developed on two different head anatomies for comparison purposes. Only a few samples of data have been utilized in the localization process, and the results have been presented in terms of the probability of detection of the sources and the mean square error for a practical range of SNR. Moreover, the effect of the conductivity profile and skull thickness variations has been investigated on the performance of this algorithm for EEG signals. Also, different modeling errors have been induced on the forward problem

solution and the effect on the localization has been studied. Further, two calibration techniques have been used to improve the detection rate of the algorithm in the presence of modeling errors. Finally, in addition to the location, the amplitude of the detected sources has been reconstructed. And the resolution of the algorithm has been compared to a well known brain source localization technique.

The rest of this thesis is organized as follows:

Chapter 2 includes the biomedical background for this topic. The origin of the brain signals in the cerebral cortex of the brain is explained. Next, EEG and MEG techniques are introduced and compared with some functional brain imaging techniques in terms of spatial and temporal resolution.

Chapter 3 is devoted to bioelectromagnetuc modeling of the fields of brain. The forward and inverse problems are more formally introduced in this chapter. Moreover, Maxwell's equations are reviewed and a quasi-static approximation for them is derived for this application. The rest of this chapter includes the famous Biot-Savart law of electromagnetics and the current dipole model. Furthermore, various possible head models, used in bioelectromagnetic studies, are presented. Finally, closed form analytical solutions for electric potential and magnetic field are presented for the simple case of a current dipole in a homogeneous infinite volume conductor.

Chapter 4 presents the literature review conducted on existing signal processing techniques for solving the bioelectromagnetic inverse problem. Two general approaches (parametric and non-parametric techniques) are introduced and prominent examples of each method are reviewed. Main advantages and shortcomings of each technique are briefly mentioned.

Chapter 5 is an introduction to array signal processing. The basics of array processing are explained using a simple scenario of a uniform linear array, in the far-field of a narrowband signal. Also a few classical and subspace methods for direction of arrival (DOA) estimation are introduced.

CHAPTER 6 contains the methodology of this thesis. The chosen software, as well as the source and head models is introduced. The procedure of developing a forward solution and generating synthetic brain signals thereafter is explained. Moreover, the mathematical basis of algorithm used in this thesis to tackle the inverse problem is

presented, and a sample run of this algorithm on MEG data is demonstrated. The assumptions made throughout the thesis and the performance metrics are also introduced in this chapter.

Chapter 7 is dedicated to brain source localization from MEG data using the proposed technique. Different head models and anatomies are developed and tested in the algorithm. Results are quantified in terms of probability of detection and mean square error in localization.

Chapter 8 investigates the performance of the proposed algorithm on synthetic EEG data for different head models and anatomies. Results are quantified in terms of probability of detection and mean square error in localization of a few proximate sources. Also, the effect of skull thickness and conductivity variations are investigated on the localization performance using EEG signals.

CHAPTER 9 includes the effect of calibration errors on brain source localization. Two forms of calibration errors are induced on the forward problem solutions and two calibration techniques are implemented to improve the performance for each scenario.

CHAPTER 10 presents reconstruction of the localized sources in space and time for MEG and EEG application. The resolution of the method used in this thesis is compared against that of weighted minimum norm estimate method.

CHAPTER 11 includes the conclusions of this thesis and some recommendations for future work.

CHAPTER 2

BIOMEDICAL BACKGROUND

2.1 The Origin of Brain Signals

Electric and magnetic fields inside the brain rise from the electrical currents that flow in neurons of the brain. A typical neuron comprises of (1) dendrites (which receive chemical signals from other neurons); (2) a cell body (or soma) including the nucleus; (3) an axon along which the electrical signal of neuron (action potential) travels; and (4) synaptic terminals that pass chemical signals (neurotransmitters) on to dendrites of the next neuron. In Figure 2.1 below you can see different parts of a neuron and how it communicates with the next neuron. Note that in brain, each neuron influences and is influenced by many other neurons [6].

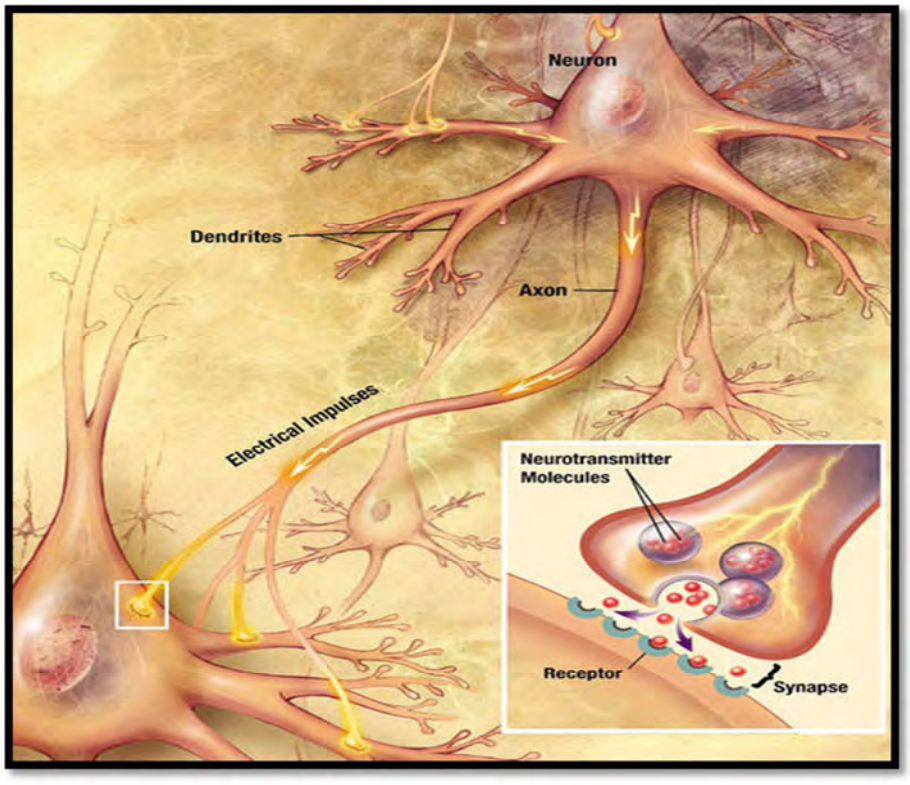

Figure 2.1: Different parts of neurons and their connections [7]

Like all biological cells, neurons have a membrane around them, which is selectively permeable to ions. Normally, the concentration of these ions such as potassium (K+), chloride (Cl-) and sodium (Na+) is different inside of the cell from that of the outside. In the resting state of a neuron, the cell membrane has low permeability for sodium ions, hence they cannot flow from outside to inside. However, potassium can leak out of the cell membrane due to diffusion gradient. This outflow of potassium causes the inside of the cell to have a more negative potential compared to outside of the cell, in resting state. This potential is called *resting potential* and its value is around -70 mV with respect to outside of the cell [6]. Note that, since the cell membrane is so thin (only few nanometers) and potential difference across it is about 70 mV, a large electric field exists on the order of 10^7 V/m across the cell membrane [6].

Once the cell is excited, the permeability of membrane for certain ions changes. If the excitation source is large enough and raises the membrane potential (V_m) to about -55 mV (*threshold voltage*), sodium channels open up and sodium ions flow from outside to inside of the cell. This inflow of sodium ions increases the cell membrane potential (V_m) further, which in turn causes even more sodium channels to open, hence more inward current, and again higher membrane potential. This *positive feedback* continues until the sodium channels are fully open and the membrane potential V_m is closer to sodium equivalent voltage ($E_{\mathrm{Na}} \approx +55$ mV), resulting in a large upswing in the membrane potential [8].

At this point, the sodium channels close, and from here on no more sodium enters the cell. Instead, sodium ions get actively transported out of the cell by the sodium potassium pump. At the same time, potassium channels open and let potassium ions flow out of the cell, hence returning the electrochemical gradient to the resting state. This whole process takes only a few milliseconds and creates the *action potential* of the neuron [8], depicted in Figure 2.2

The currents flowing inwards at a point on the axon depolarize the adjacent sections of its membrane, and if sufficiently strong, this depolarization provokes a similar action potential at the neighboring membrane patches. Thus, the generated action potential propagates as a wave along the axon. It's important to note that each action

potential is followed by a *refractory period*. During an *absolute refractory period* it is impossible to evoke another action potential in the neuron membrane, but later during a *relative refractory period*, using a stronger-than-usual stimulus we can excite the membrane again. The refractory period is the mechanism which forces the action potential to move forward along the axon and not to travel back the way it just came [8].

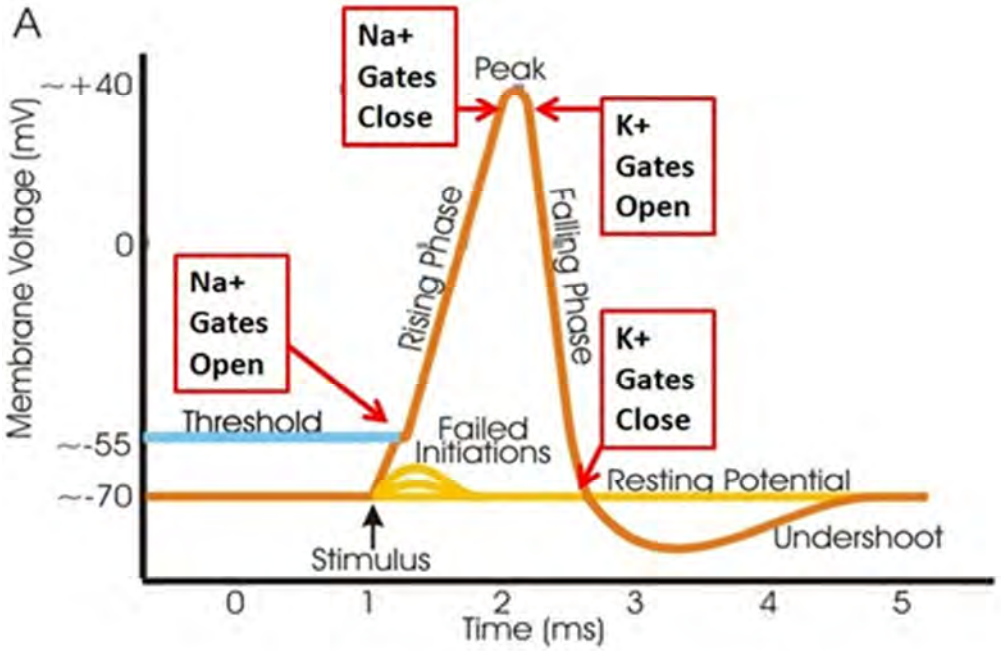

Figure 2.2 : Generation of action potential in an excited cell (adapted from [7])

There's another point to keep in mind about excitation of neurons. A neuron may receive synaptic inputs from hundreds or thousands of other neurons, with varying amounts of simultaneous input. If the combined activity of these neurons increases the membrane potential, it is called an *excitatory postsynaptic potential* (EPSP). If this EPSP *depolarizes* the postsynaptic cell sufficiently (above threshold value), an *action potential* will occur [9].

However, an overall postsynaptic potential may also decrease the membrane potential and move it away from its firing threshold (*hyperpolarization*). In this case we call this postsynaptic potential an *inhibitory postsynaptic potential* (IPSP) [9].

Later in this report we'll see that an action potential can be described by a *quadrupole*, whose magnetic and electric fields decay more rapidly than those of a dipole

[6]. Also, the postsynaptic potential (PSP) can be described by a *current dipole*, giving rise to currents in the surrounding tissues, which can exist for several tens of milliseconds causing the so called volume conductor currents [10].

MEG mainly records the magnetic field generated by the currents flowing in dendrites of the pyramidal neurons due to the PSP's [6] and the EEG records the potential due to volume conductor currents flowing in brain as a result of the mentioned postsynaptic activity [6].

In an excited neuron, in addition to the intracellular currents (*primary current*), passive ohmic currents are also set up in the surrounding medium to complete the loop of ionic flow such that there is no buildup of charge. These are called secondary or *volume conductor currents.* Figure 2.3 shows a schematic of both current types.

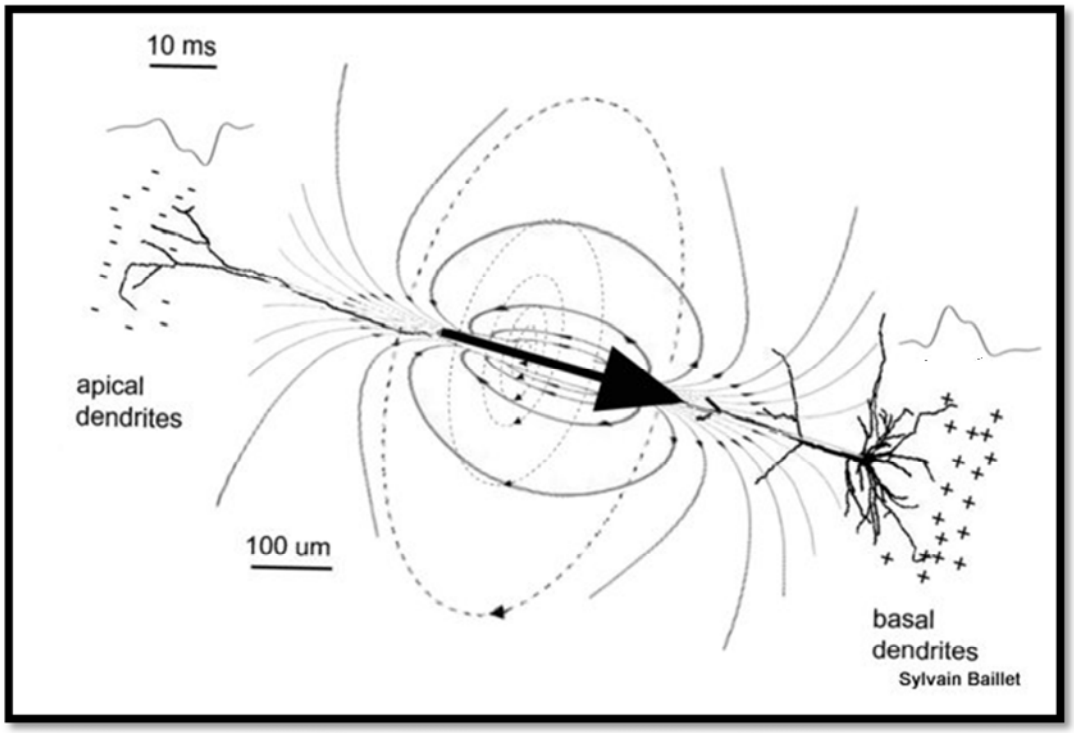

Figure 2.3: Primary and secondary currents of a neuron [11]

Reprinted by permission of Medical College of Wisconsin, (8 Jan 2012)

Both primary and secondary currents contribute to magnetic fields outside the head and to electric scalp potentials, but in order for the neural currents to add up in a way that can produce measurable fields outside the head, their spatial arrangement is of importance [1]. To better understand this concept, we should have a look at the structure of the cerebral cortex of the brain.

2.2 Cerebral Cortex

EEG and MEG studies are mainly concerned with the uppermost layer of the brain, which is the cerebral cortex. It is a 2–4 mm thick sheet of gray tissue where most of the measured neural activity takes place. At least 10 billion neurons reside in the whole cortex tissue. The total surface area of the cortex is about 2500 cm^2, but it is folded such that it fits into the cranial cavity formed by the skull [6].

Most regions of the cortex have been mapped functionally. For example, we know that the primary somatosensory cortex receives tactile stimuli from the skin, and the area in primary motor cortex is involved in the movement of specific parts of the body, and so on [6]. Figure 2.4 shows how the cortex is virtually divided in to lobes for being studies and how different parts of cortex are functionally mapped.

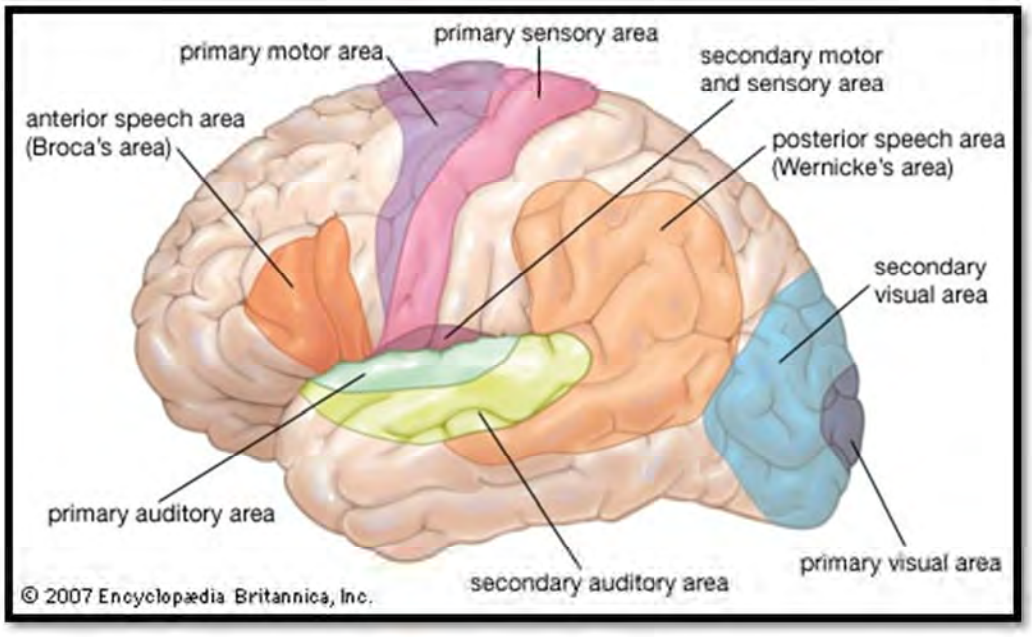

Figure 2.4: Cerebral Cortex lobes and functional mapping [12]

The cortex is organized in six parallel layers. Layer 1 is the uppermost one. Layers 2, 4 and 6 are mostly populated with nonpyramidal such as stellate cells, which have a star shaped structure. Layer 5 contains the large pyramidal cells, which have a linear structure with dendrites arranged parallel to each other and perpendicular to cortex surface [6]. Apical dendrites of pyramidal cells reach up to the first layer of cortex and axons from these cells typically project to more distant cortical regions, to other parts of the brain, or to lower centers (such as spinal motor neurons). Due to their structure and arrangement, synchronous activity of tens of thousands of pyramidal neurons of cortex are believed to be the main sources of MEG and EEG signals [1]. Figure 2.5 shows a schematic of cortical layers. Pyramidal and stellate neurons are depicted in their corresponding layers.

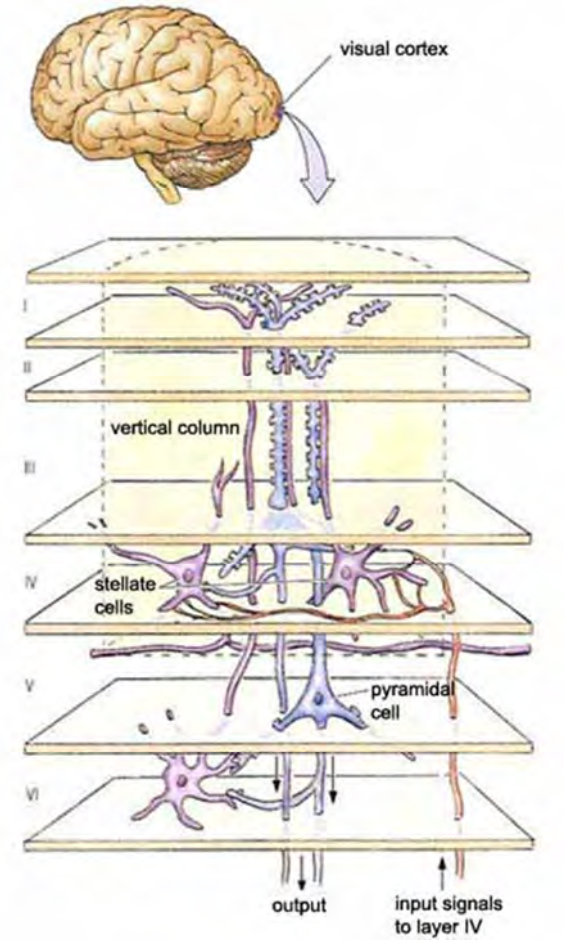

Figure 2.5: Location and Types of main cortical neurons [13]

The currents generated along apical dendrites of pyramidal neurons are believed to be the source of most signals detected in MEG and EEG, because they typically last longer than the rapidly firing action potentials traveling along the axons of excited neurons [1]. Calculations suggest that each synapse along a dendrite may contribute as little as a 20 fA-m current source. But through measurements we see sources on the order of 10 nA-m, which is the cumulative summation of millions of synaptic junctions in a relatively small region [1]. The measured magnetic field outside the scalp rising from such brain activity is on the order of 10^{-12} Tesla, which is extremely small [14].

Due to the pattern and orientation of the magnetic field (obtained from right-hand rule), MEG signals reflect the current flow in the apical dendrites of those pyramidal cells which are oriented *tangentially* with respect to the skull surface. However, EEG reflects potentials that rise from both tangentially and radially oriented volume currents [14]. Figure 2.6 shows some tangentially oriented current sources and their resulting magnetic field from the right hand rule.

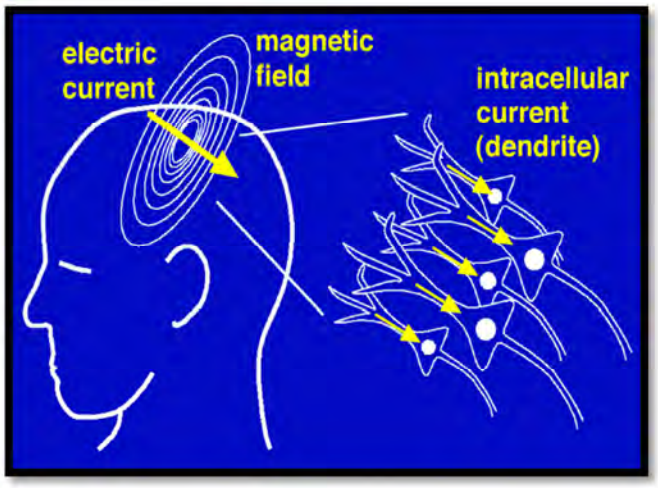

Figure 2.6: Magnetic field of tangential current sources (measured in MEG) from right hand rule [15]

In the end it's worth mentioning that, even though cortical pyramidal neurons are assumed to be the main contributors to MEG and EEG signals, some authors have reported scalp recordings of deeper cortical structures including the hippocampus, cerebellum, and thalamus [1]. However, the contribution from the cortex is overwhelmingly large compared to all other structures, due to two factors: (1) the number

of cortical neurons is much larger than that of subcortical neurons; (2) the distance from subcortical structures to the scalp electrodes is larger than from cortical structures to the electrodes [16].

2.3 Functional Brain Imaging Techniques

As we mentioned before, we can use functional brain imaging techniques to understand the human brain better. These techniques are non-invasive and produce images of the electrophysiological, hemodynamic, metabolic, and neurochemical processes that underlie normal and pathological brain function [1].

For example, in positron emission tomography technique (PET), we can use radioactively labeled organic molecules or probes that are involved in the processes of interest (such as glucose metabolism or dopamine synthesis) to study brain metabolism and neurochemistry [1]. Hence, we can view images of dynamic changes in the spatial distribution of these probes, as they are transported and chemically modified within the brain. These images have high spatial resolution (2 millimeter), but the temporal resolution is around several minutes, due to the dynamics of the processes being studied, and by photon- counting noise [1]. Another similar technique is single-photon emission computed tomography (SPECT) that uses radioactive tracers to tract metabolic activity of the brain.

We can also study the neural activity more closely by investigating hemodynamic changes. The principle behind this idea is that: when neurons become active, they induce localized changes in the blood flow and oxygenation levels. These changes can be tracked using PET, functional magnetic resonance imaging (fMRI), Near-infrared spectroscopy (NIRS), and various transcranial optical imaging methods [1][17]. Among these methods, fMRI is currently the most widely used. It has high spatial resolution of 1-2 millimeter, but temporal resolution of around 1 second, which is still relatively low. The limitation in temporal resolution is due to the relatively slow hemodynamic response compared to the speed of electrical neural activity. Another complication of using fMRI rises from the fact that regions of blood oxygenation level dependent (BOLD) changes detected by fMRI do not necessarily correspond one-to-one with regions of electrical neural activity. This hampers interpretation of fMRI data [1].

Two well-known bioelectromagnetic methods to map the brain functionally are EEG and MEG.EEG measures scalp potentials produced by electrical activity in neural cell assemblies, and MEG measures the magnetic fields outside the head, produced by the same sources. These two techniques offer higher temporal resolution (on order of millisecond) compared to PET or fMRI.

However, the spatial resolving power of MEG and EEG does not, in general, match that of PET and fMRI. This limitation in spatial resolution is due to two reasons [1]: (1) the relatively small number (few hundred) of spatial measurements in EEG/MEG, compared to PET/fMRI (tens of thousands); (2) ill posed nature of static electromagnetic inverse problem for brain signal sources. Yet, by placing restrictive models on the sources of MEG and EEG signals we can achieve resolutions similar to those of fMRI and PET [1].

2.3.1 Electroencephalography (EEG)

Electroencephalography (EEG) is a functional brain imaging technique in which the potential differences between pairs of electrodes placed on the scalp are measured. As mentioned before, these readings are the summation of potentials generated from the volume conductor currents induced in the conductive media of the head; which appear as a result of large clusters of synchronized cortical pyramidal neurons undergoing postsynaptic potentials (PSPs) [6][16].

Pyramidal neurons constitute approximately 80% of the cortex and are oriented perpendicular to the surface. A typical cluster size of these neurons must cover at least 40 to 200 mm2 of cortical surface in order to produce a measurable scalp signal [16].

Good news is that, by using the fact that EEG sources are confined to the cortical surface of the brain and activity of cortical pyramidal neurons, we can narrow significantly the nonuniqueness of the inverse solution [16].

The internationally standardized *10-20 electrode system* is usually employed to record the spontaneous EEG. In this system 21 electrodes (19 + ground+ reference electrode) are located on the surface of the scalp, as shown in Figure 2.7A and B. Also, intermediate 10% electrode positions can be used (shown by black circles in Figure 2.8) [18]. Additional electrodes can be added to the standard set-up when a clinical or

research application demands increased spatial resolution for a particular area of the brain. High-density arrays (typically via cap or net) can contain up to 256 electrodes more-or-less evenly spaced around the scalp.

As for the resolution of EEG, spatial resolution is in millimeter range, and temporal resolution on the order of milliseconds. As for the amplitude, a typical adult human EEG signal is about 10μV to 100 μV in amplitude when measured from the scalp and is about 10–20 mV when measured from subdural electrodes [19]. Advantages of EEG over methods like PET and fMRI are

EEG's can detect changes within a millisecond timeframe, which is excellent considering an action potential takes approximately 0.5-130 milliseconds to propagate across a single neuron, depending on the type of neuron. Remember that other methods of looking at brain activity, such as PET and fMRI have time resolution between seconds and minutes.

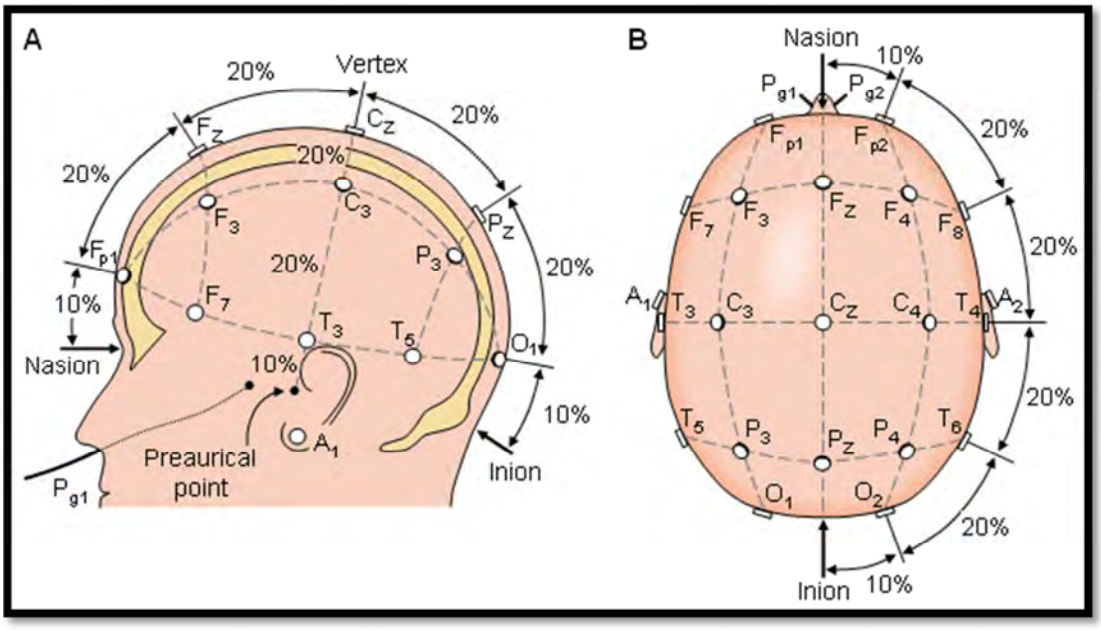

Figure 2.7: The international 10-20 system seen from (A) left and (B) above the head. A = Ear lobe, C = central, Pg = nasopharyngeal, P = parietal, F = frontal, Fp = frontal polar, O = occipital [17]

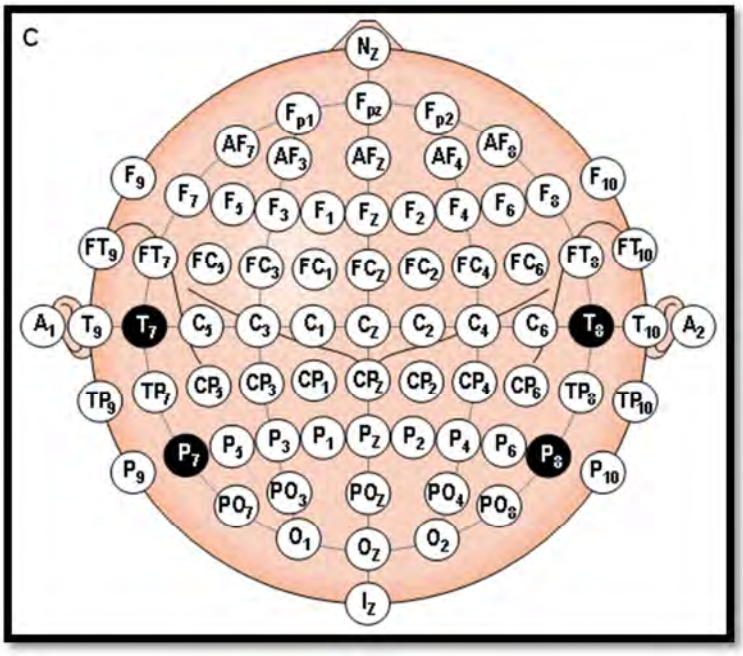

Figure 2.8: Location and nomenclature of the intermediate 10% electrodes, as standardized by the American Electroencephalographic Society [17].

EEG measures the brain's electrical activity directly, while other methods record changes in blood flow (e.g., SPECT, fMRI) or metabolic activity (e.g., PET), which are indirect markers of brain electrical activity [19].

The major drawback in estimating cerebral sources from EEG recordings is the effect of parameters such as thickness of the skull and scalp, conductivity anisotropy, and inhomogeneity of the head, on the forward and inverse problems. For example, potentials in the skull decrease depending on its thickness. Moreover, low conductivity of the skull spreads out the potentials in transverse directions. As a result, focal sources in the brain could be averaged out in the scalp [6]. These variables do not pose as much problem in MEG method though, which we study next.

2.3.2 Magnetoencephalography (MEG)

Magnetoencephalography (MEG) is a non-invasive neurophysiological technique that measures the magnetic fields generated by neuronal activity of the brain. MEG is a direct measure of brain function, unlike functional measures such as fMRI, PET and SPECT that are secondary measures of brain function reflecting brain metabolism [20].

The magnetic field passes unaffected through brain tissue and the skull, so it can be recorded outside the head. The magnetic field is extremely small, but can be detected by sophisticated sensors that are based on superconductivity [20]

MEG has a very high temporal resolution. Events with time scales on the order of milliseconds can be resolved, again differentiating MEG from fMRI, PET and SPECT, which have much longer time scales. Also MEG has excellent spatial resolution; sources can be localized with millimeter precision [20].The activity recorded in MEG is mostly confined to a frequency window less than 100 Hz but components up to 600 Hz have been studied .The strength of the biomagnetic field is 50–500 fT which is about 10^8 times smaller than the magnetic field of the earth. The measurement of neuromagnetic fields are quite weak and require extremely sensitive sensors with a good control of the external noise [6].

The sensor used in biomagnetic instruments is called superconducting quantum interference device (SQUID).When cooled to very low temperatures, superconductors conduct electricity without resistance. This lack of resistance allows a SQUID to measure the interference of quantum-mechanical electron waves circulating in the superconducting loop as the magnetic flux enclosed by the loop changes and the SQUID circuitry produces a voltage proportional to this change. The associated computer software converts the SQUID data into current flow maps throughout the brain as a function of time.

In

Figure 2.9 you can see two different coil configuration SQIUDs.

Figure 2.9(d) shows a first order axial gradiometer which detects the z-derivative of the magnetic field and consists of two coils connected in series but wound in opposite senses, separated by a distance.

Figure 2.9(e) shows a planar gradiometer which detects the x and y derivatives of the magnetic field.

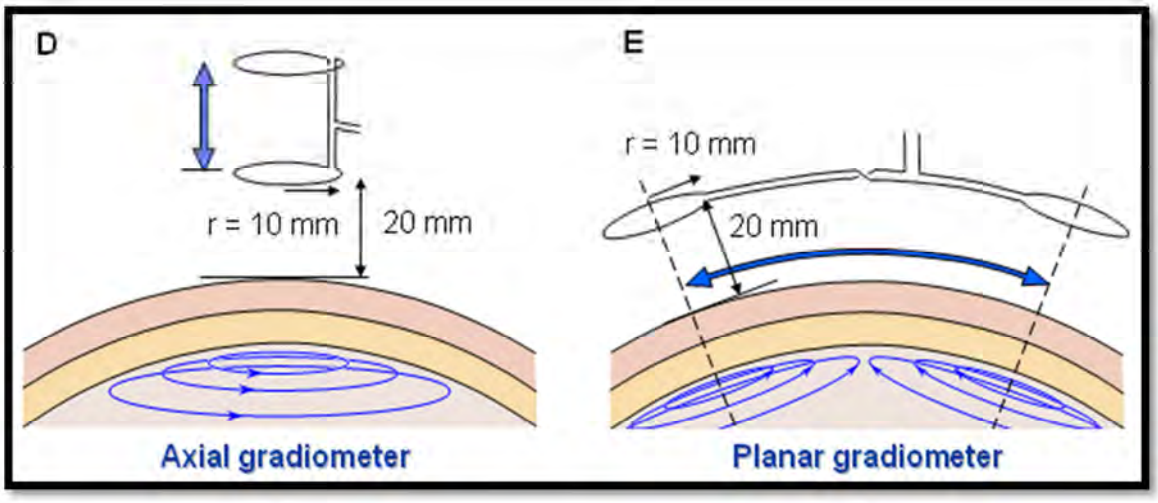

Figure 2.9: (d) axial gradiometer (e) planar gradiometer [17]

More recently, EEG and MEG have come to be viewed as complementary rather than competing modalities and most MEG facilities are equipped for simultaneous acquisition of both EEG and MEG data [1].

CHAPTER 3

MODELING BIOELECTROMAGNETIC FIELDS OF BRAIN

3.1 Forward and Inverse Problems

As we defined before, the *inverse problem* comprises of estimating current sources in the brain (mainly cortex) which result in specific electric/magnetic signals measured on/outside the scalp. Figure 3.1 shows a schematic of a current dipole as the source inside the brain. The electrodes are placed on/outside the scalp depending on whether we want to measure potentials or magnetic fields. We have to note that in case of measuring potentials (EEG), the shape of the head, conductivity of the brain, skull, and scalp are all important parameters; however, magnetic field is not affected by the conductivities of these intermediate media.

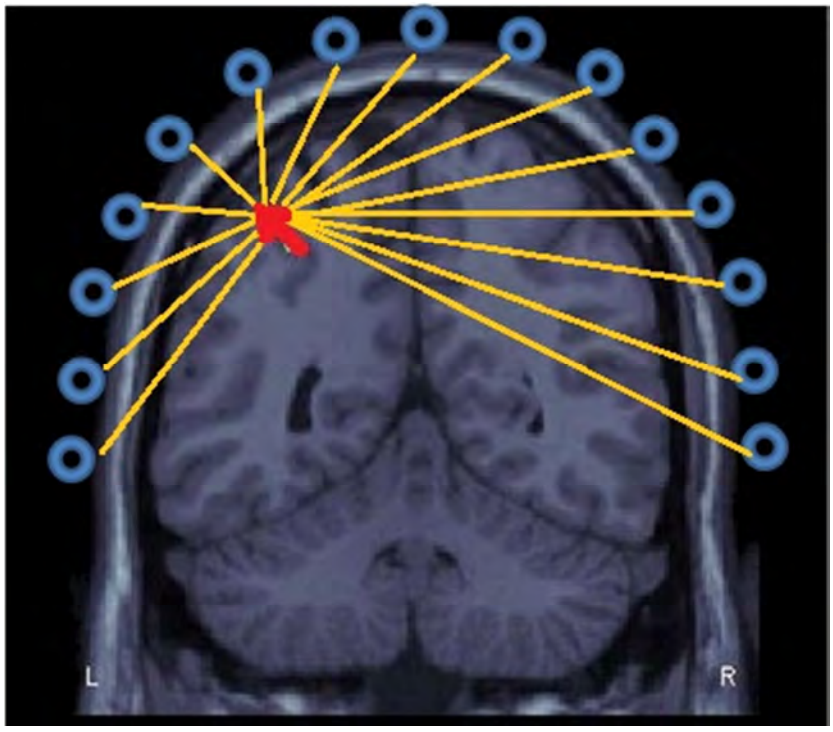

Figure 3.1: Current dipole representing a current source in the brain, and electrodes on/outside scalp which measure the corresponding electric/magnetic fields

Forward problem can be modeled mathematically as [21]:

$$B_k = \int L_k^M(r) * J^P(r)\, dV \tag{3.1}$$

$$V_{ij} = \int L_{ij}^M(r) * J^P(r)\, dV \tag{3.2}$$

B_k and V_{ij} respectively denote signal at magnetometer (*k)* and between electrodes (*ij).* $L_k^M(r)$ and $L_{ij}^M(r)$ are *lead fields* for magnetometer (*k)* and electrode pairs (*ij).* They represent sensitivity patterns of sensors to sources. Lead fields also depend on sensor locations and configurations (as well as on head conductivities in electric potential case). $J^P(r)$ denotes primary source current at locations (r) [21].

In the *forward problem*, by knowing $J^P(r)$, and having an approximation of the lead fields (L), we can find unique solutions for magnetic field and electric potential (**B** and V). Hence we say the forward problem is *well-posed*.

In the *inverse problem*, we have measured B and V, and using approximations of the lead fields (L), we try to find the location of primary current densities $J^P(r)$. This kind of problem does not have a unique solution and is called ill-posed.

We notice that in order to solve the *inverse problem*, we need approximations of the lead fields. Here we need to have a closer look at the electromagnetic theory behind EEG and MEG methods.

3.2 Maxwell's Equations

The following four equations constitute the famous Maxwell's equations [22]:

$$\nabla \times \boldsymbol{H} = \frac{\partial \boldsymbol{D}}{\partial t} + \boldsymbol{J} \tag{3.3}$$

$$\nabla \times \boldsymbol{E} = -\frac{\partial \boldsymbol{B}}{\partial t} \tag{3.4}$$

$$\nabla . \boldsymbol{B} = 0 \tag{3.5}$$

$$\nabla . \boldsymbol{D} = \rho_v \tag{3.6}$$

where **H** is the magnetic field intensity (A/m), **E** is electric field intensity (V/m), **D** is electric flux density (C/m$^{2)}$, **B** is magnetic flux density (W/m^2 or Tesla), **J** is electric current density (A/m^2) and ρ_v is electric volume charge density (C/m^3). Also, **E** and **D** are related through $\boldsymbol{D} = \varepsilon \boldsymbol{E}$, while **H** and **B** have a similar relation$\boldsymbol{B} = \mu \boldsymbol{H}$**.**

Here **ε** denotes permittivity of the medium (F/m) and μ stands for permeability of the medium (H/m). Another useful relation is $\boldsymbol{J} = \sigma \boldsymbol{E}$ (Ohm's law) which relates J and E via the conductivity of the medium (σ). We should note that ε,μ and σ are scalar for isotropic media and tensors for anisotropic media.

3.2.1 Quasi-static Approximation to Maxwell's Equations

If the effects of the time dependent terms in Maxwell's equations can be neglected, we can simplify the equations. Validity of this approximation depends on the frequency of the signals and the properties of the medium, i.e. σ, ε, μ. Since measurements show that the frequency of the signals obtained from MEG and EEG are typically below 1 kHz, we can apply a *quasi-static* approximation of Maxwell's equations [6]. Hence, the terms with time dependency can be omitted and we can rewrite equations (3.3) and (3.4) as:

$$\nabla \times \boldsymbol{H} = \boldsymbol{J} \tag{3.7}$$

$$\nabla \times \boldsymbol{E} = 0 \tag{3.8}$$

Taking divergence of both sides of equation (3.7) will result in:

$$\nabla . (\nabla \times \boldsymbol{H}) = \nabla . \boldsymbol{J} \tag{3.9}$$

Since the left-hand side of equation (3.9) is zero, we get:

$$\nabla . \boldsymbol{J} = 0 \tag{3.10}$$

The total current density **J** can be divided into *primary current density* (J_P) and *volume current density* (J_Ω) as follows:

$$\boldsymbol{J} = \boldsymbol{J}_P + \boldsymbol{J}_\Omega \tag{3.11}$$

As we discussed before, primary current is generated by neural activity within the neuronal cells, whereas the volume currents which flow passively in the conductive medium. The total current is the sum of these two current components. **The primary current density ($\boldsymbol{J}_P$) represents the source of the brain activity which we are trying to locate**. However, modeling the volume currents enhances the localization accuracy [6]. The volume current can be represented as:

$$\boldsymbol{J}_\Omega = \sigma \boldsymbol{E} \tag{3.12}$$

Also we note that equation (3.8) can be satisfied by representing electric field **E** with a gradient of a scalar function, the potential V as:

$$\boldsymbol{E} = -\nabla V \tag{3.13}$$

From equations (3.12) and (3.13) we see that the volume current density can be written as:

$$\boldsymbol{J}_\Omega = -\boldsymbol{\sigma}\nabla \mathrm{V} \tag{3.14}$$

Hence, total current density can be rewritten as:

$$\boldsymbol{J} = \boldsymbol{J}_P - \boldsymbol{\sigma}\nabla \mathrm{V} \tag{3.15}$$

3.3 The Biot-Savart Law

From the well-known Biot-Savart law we can find the magnetic field B at location r due to current density J at location r'as follows [22].

$$\boldsymbol{B}(r) = \frac{\mu_0}{4\pi} \int J(r') \times \frac{r - r'}{\left|\left|r - r'\right|\right|^3} dv' \tag{3.16}$$

where $\mu_0$is permeability of free space and dv' is the differential element of volume.

If we assume that the head consists of a set of contiguous regions each of constant isotropic conductivity σ_i ,i =1,...,3, representing the brain, skull and scalp for instance (Figure 3.4) , we can rewrite the Biot-Savart law above as a sum of contributions from the primary and volume currents [1]:

$$\boldsymbol{B}(r) = B_0(r) + \frac{\mu_0}{4\pi}\sum_{ij}(\sigma_i - \sigma_j)\int_{S_{ij}} V(r')n(r')\frac{r-r'}{\left||r-r'|\right|^3}\times dS'_{ij} \qquad (3.17)$$

where $B_0(r)$ is the magnetic field in an infinite homogeneous medium, due to the primary current distribution $J^P(r')$.

$$\boldsymbol{B_0}(r) = \frac{\mu_0}{4\pi}\int J^P(r')\times\frac{r-r'}{\left||r-r'|\right|^3}dr' \qquad (3.18)$$

The second term in equation (3.17) is the magnetic field due to volume currents, expressed as a sum of surface integrals over the brain-skull, skull-scalp, and scalp-air boundaries. $n(r')dS'_{ij}$ is a vector element of surface S_{ij} oriented along the outward unit norm of S_{ij}. Hence, the magnetic field can be calculated if we know the primary current distribution and the potential $V(\boldsymbol{r}')$ on all surfaces [1]. A similar equation can be derived for the potential itself [1]:

$$\begin{aligned}(\sigma_i + \sigma_j)V(r) &= 2\sigma_0 V_0(r) \\ &\quad - \frac{1}{2\pi}\sum_{ij}(\sigma_i - \sigma_j)\int_{S_{ij}} V(r')\,n(r')\frac{r-r'}{\left||r-r'|\right|^3}.dS'_{ij}\end{aligned} \qquad (3.19)$$

The above equation holds for potentials on surface S_{ij} where $V_0(r)$ is the potential at r in a infinite homogeneous medium, due to the primary current distribution.

$$V_0(r) = \frac{1}{4\pi\sigma_0}\int J^P(r').\frac{r-r'}{\left||r-r'|\right|^3}dr' \qquad (3.20)$$

Equations (3.17) and (3.18) represent the integral solutions to the forward problem. If we specify a primary current density distribution $J^P(r')$ we can calculate a primary potential and a primary magnetic field [1]. The primary potential $V_0(r)$ is then used to solve equation (3.19) for the potentials on all surfaces, and therefore solves the forward problem for EEG. These surface potentials $V(\boldsymbol{r})$ and the primary magnetic field $B_0(r)$ are then used to solve equation (3.17) for the external magnetic fields [1].

Equation (3.19) has analytic solutions only for special shapes and must otherwise be solved numerically. We return to specific solutions of the forward problem later, but first we discuss the models used to describe the primary current distributions.

3.4 The Equivalent Current Dipole Model

We can model a cortical pyramidal neuron, undergoing a PSP, as a current dipole. The current dipole consists of a current source and a current sink separated by a distance, in this case around 100 to 500 micrometer. The distance between the two sources is very small compared to the distance from the scalp electrodes [16].

The process that creates the dipolar behavior is the same that we discussed earlier in this report. For example, if an incoming axon from a presynaptic neuron terminates at a basal dendrite of a pyramidal neuron and induces excitatory postsynaptic potential (EPSP) there, it will cause sodium channels to open and inflow of sodium (Na+) will create a current sink. Consequently, a current source will be created at apical dendrites to conserve electrical neutrality. The two sources are always paired and extremely close to each other compared to the point of observation (outside scalp) [16]. Current dipole model is representation for coherent activation of not just one, but a large number of pyramidal neurons in cortex.

The validity of using a dipole model is restricted to cases where electric neuronal activity is dominated by a small brain area. For example, in epileptic spikes, and in the description of the early components of the average brain stem auditory evoked potential. However, localization of higher cognitive functions could not be reliably modeled by dipole fitting, because the whole cortex is never totally “quiet” except for a single small area, which is the basic assumption in single dipole model. [16].

In order to develop the mathematical model, we assume a small patch of activated cortex is centered at location $r_P$and that the observation point r is some distance away from this patch. In this case, we can approximate the primary current distribution as an equivalent current dipole represented as a point source,

$$J^P(r) = P\delta(r - r_P) \tag{3.21}$$

where $\delta(r)$ is the Dirac delta function and moment $P \equiv \int J^P(r')dr'$.

When too many small regions and their dipoles are required to represent a single large region of coherent activation, single dipole model does not work well. We can model such sources using a multipolar model, i.e. quadrupole, octupole, and so on [1]. For example, an action potential can be described by a quadrupole, whose magnetic and electric fields decay more rapidly than those of a dipole [6]. However, contributions to the magnetic field from octupolar and higher order terms drop off rapidly with distance, so dipolar and quadrupolar models are probably sufficient to represent most prominent cortical sources [1]. Figure 3.2 shows the electric and magnetic fields around a current dipole.

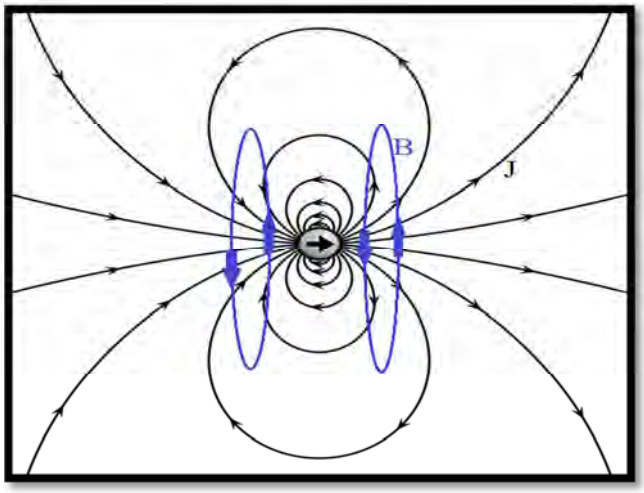

Figure 3.2: Electric and magnetic fields of a magnetic dipole (adapted from [23])

3.5 Head Models

In order to compute the electric potentials and magnetic fields on/outside scalp, we need to solve the forward problem equations (17) and (18). To do so, we need to have the conductive media's (head's) shape and conduction profile. For simple geometries like a homogeneous spherical shell, or a concentric nested set of them, we can find analytical

solutions for B and V in forward problem. However, when more realistic head models are used, we have to resort to numerical solutions to compute the surface integrals [1].

3.5.1 Single Sphere Head Model

Early studies in EEG source modeling used a single sphere with homogeneous conductivity to represent the head. For MEG, single sphere model to represent the inner surface of the skull is usually used. Single sphere model is the most basic kind of model to represent the human head used in source localization studies [6]. Figure 3.3 shows a schematic of a current dipole inside such single homogeneous sphere model.

However, studies using the single homogeneous sphere model produced large localization errors, because this model does not account for the *smearing* effect of the skull's low conductivity on scalp EEG's. MEG source localization accuracy, however, does not suffer as much as EEG with this model because the tissue conductivity does not affect the primary magnetic field as much [6]. Moreover, producing a single sphere head model is approximately three orders of magnitude faster to compute than a boundary element method (BEM) based realistic head model. And unlike BEM realistic models, no conductivity profile is explicitly required in the calculation using the spherical head model. However, although it has been widely used, the single sphere head model has been found to be inadequate for some regions of the brain, for example frontal and frontal-temporal areas [24][25].

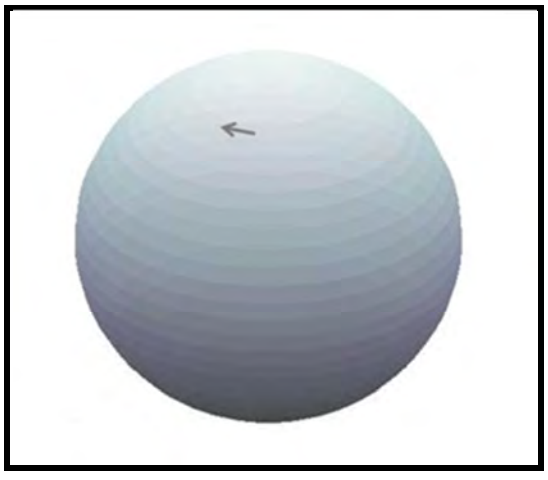

Figure 3.3: Current dipole inside single homogeneous sphere model

3.5.2 Multiple Spheres Head Model

This model is routinely used in most clinical and research applications to MEG/EEG source localization. The head is assumed to consist of a set of nested concentric homogeneous spherical shells representing brain, skull, and scalp [1] as shown in Figure 3.4. Closed form expressions for the electric potential and magnetic field of a current dipole inside the concentric spheres have been derived in the literature [26]. However, deviations from the realistic head model affect the volume currents more than the primary currents. Hence, since MEG signals are less sensitive to volume currents compared to EEG, spherical models are generally more suited for MEG applications than for EEG.

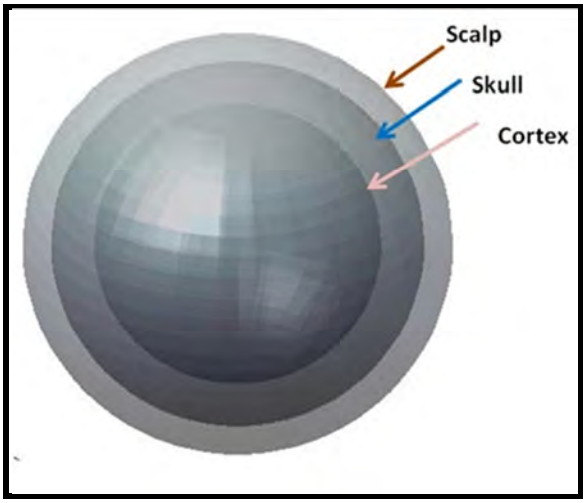

Figure 3.4: Three-shell model of the head

3.5.3 Overlapping Spheres Head Model

This model was developed by Huang in 1999. The overlapping spheres head model tries to maintain the computational efficiency of the spherical head model, yet achieve higher modeling accuracy (close to that of BEM models). In this method, instead of fitting a single sphere to the whole head, locally fitted spheres are used. That is, based on the head geometry, a set of grid points within the brain are used to fit spheres to different regions of the brain on a sensor-by-sensor basis. For each sensor, the center of the spheres is chosen such that the resulting field (forward model) is as close as possible to the field obtained from a three layer BEM model, over all the grid points. Later, when

dipole fields are calculated for each sensor (forward solution), this simpler sphere solution is used [25].

Figure 6.6 and Figure 6.7 in this thesis depict two examples of such best fitting spheres for the overlapping spheres head model, generated in Brainstorm software.

3.5.4 Realistic Head Models

In reality, our heads are anisotropic, inhomogeneous, and not spherical conductors. In order to find more accurate solutions to the forward problem, we can use anatomical information obtained from high-resolution volumetric brain images obtained with MR or X-ray computed tomography (CT) imaging [1].

Usually boundary element method (BEM) or finite element method (FEM) is used to construct more realistic head models when needed. In BEM, true surfaces are replaced with geometric elements, typically planar triangles as shown in Figure 3.5. Hence, the general solution is replaced by thousands of simpler equations [27].

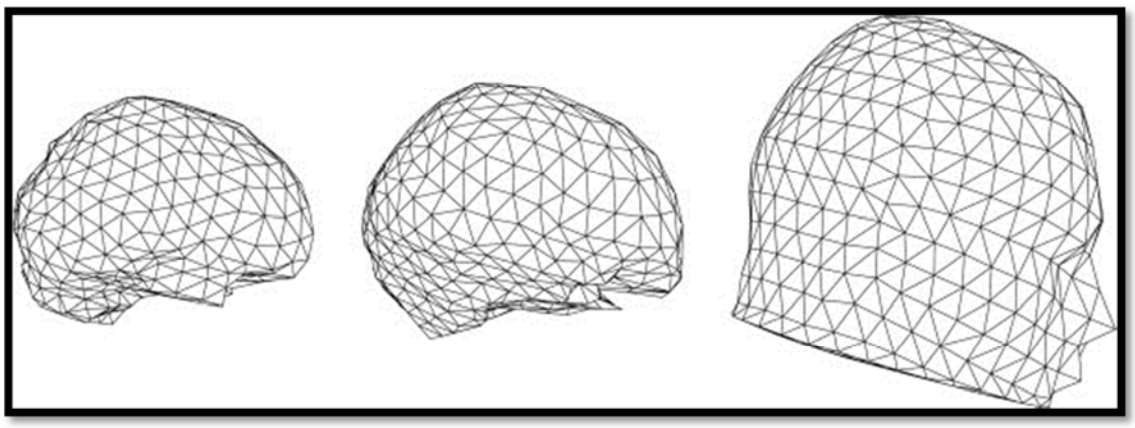

Figure 3.5: Realistic head model constructed using BEM [28]

While this is an improvement on the spherical model, the BEM methods still assume homogeneity and isotropy within each region of the head. This ignores, for example, anisotropy in white matter tracts of brain and inhomogeneousness in the skull due to sinuses and diploic spaces. However, finite element method (FEM) takes all these factors into consideration [1] (Figure 3.6).

Typically BEM and FEM calculations are very time consuming and use of these methods may appear impractical when incorporated as part of an iterative inverse solution. But through use of fast numerical methods, precalculation, look-up tables and interpolation of precalculated fields, both FEM and BEM can be made quite practical for applications in MEG and EEG [1].

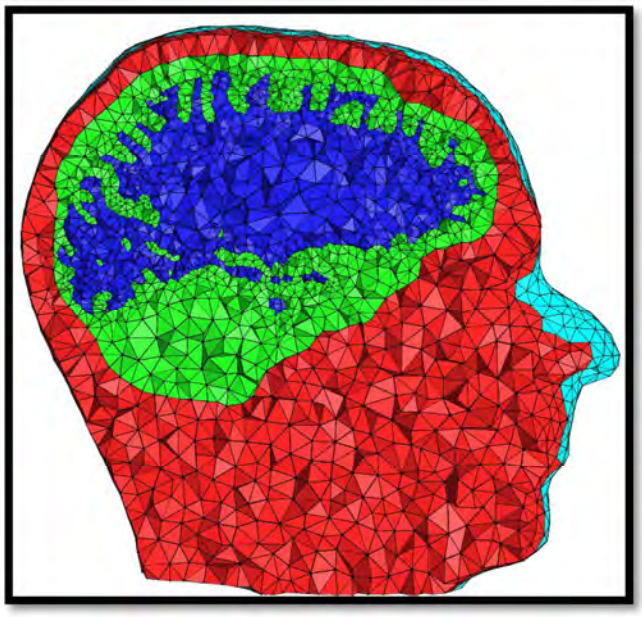

Figure 3.6: Realistic head model constructed by FEM [29]

3.6 Analytical Solutions for Simple cases:

In this section, analytical solutions to the bioelectromagnetic forward problem are presented for simple geometries with simplistic assumptions.

3.6.1 Potential from Current Dipole in Infinite Homogeneous Medium

Assume we have a dipole current consisting of a current sink $-I$ and current source I, separated by distance d, along the z-axis. Assume also that the dipole is placed in an infinite homogeneous volume conductor as shown in Figure 3.7. We intend to find the electric potential at a distance r from the center of the dipole. A simple derivation will result in [30]:

$$V_d = \frac{\boldsymbol{P}}{4\pi\sigma}.\frac{\boldsymbol{a_r}}{r^2} \qquad (3.22)$$

where $\boldsymbol{P} = I\boldsymbol{d}$ is the dipole moment, d is a distance vector pointing from current sink to current source, σ is conductivity of the infinite volume conductor, $\boldsymbol{r}$ is the position vector of the observation point with respect to the center of the dipole ($r \gg d$), and $\boldsymbol{a_r}$is the unit vector in the direction of $\boldsymbol{r}$, and the dot represents a dot (inner) product.

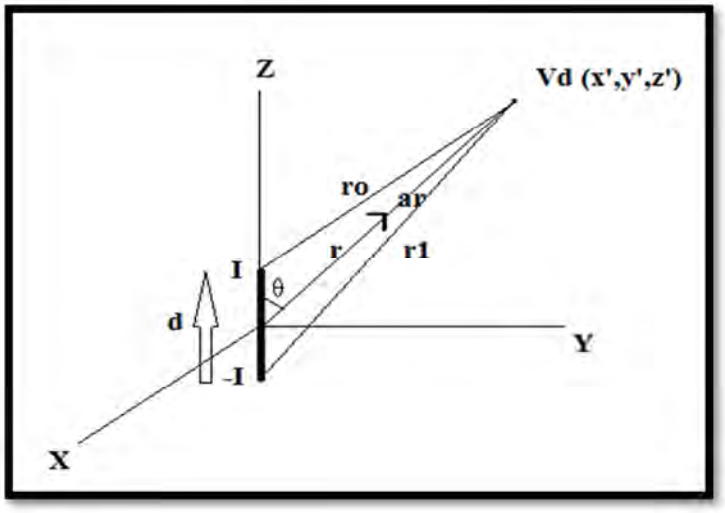

Figure 3.7: Current Dipole in Infinite Volume Conductor

3.6.2 Magnetic Field from Current Dipole in Infinite Homogeneous Medium

Assume a current dipole of moment P located at $r_P$in a spherical homogeneous conductor, and an MEG system in which we measure only the radial component of the magnetic field, i.e., the coil surface of the magnetometer is oriented orthogonally to a radial line from the center of the sphere through the center of the coil. The contributions of the volume currents vanish in this case, and we are left with only the primary term $B_0(r)$. Taking the radial component of this field for the current dipole reduces to [30]:

$$B_r(r) = \boldsymbol{a_r}.\boldsymbol{B_0}(\boldsymbol{r}) = \frac{\mu_0}{4\pi}\frac{\boldsymbol{P}\times\boldsymbol{r_P}}{||\boldsymbol{r}-\boldsymbol{r_P}||^3}.\boldsymbol{a_r} \qquad (3.23)$$

We notice that this magnetic field solution is linear in the dipole moment P but highly nonlinear with respect to its location r_P. We can also see that due to the triple scalar product, $B_r(r)$ is zero everywhere outside the head if P points towards the radial direction r_P. That's actually why radially oriented dipoles do not produce any external magnetic field outside a spherically symmetric volume conductor. However, EEG is sensitive to radial sources, which is one of the major differences between EEG and MEG [1].

CHAPTER 4

SOLUTIONS OF THE INVERSE PROBLEM USING SIGNAL PROCESSING APPROACHES

In this chapter, we categorize and study the existing proposed techniques for solving the inverse problem in bioelectromagnetism using signal processing appraoches. In order to localize sources of EEG or MEG signals, there exist two general approaches currently [EBM]. In this chapter, we discuss briefly the concept behind each of these two dominant approaches and provide examples for each; also assumptions and limitations of each method will be mentioned.

4.1 Parametric Methods

In parametric methods, the main assumption is that sources of brain activity can be represented by a few equivalent current dipoles. The unknowns in this case are the locations, amplitudes and orientations of the dipoles which are estimated using nonlinear numerical methods. Main solutions using such approaches are given below.

4.1.1 Least-Squares Source Estimation

In this method, the focal sources of brain activity are modeled using equivalent current dipoles (ECD) and six parameters are assigned to each dipole: three location parameters (x,y,z), two orientation parameters (azimuth and elevation angles) and one strength parameter (amplitude). The algorithm for this method works as follows [1][31]:

First, the number of dipoles is decided and initial parameters are selected for each dipole; second, forward solution is computed for the given dipole parameters (i.e. resulting potentials or magnetic fields are estimated); third, solutions of the forward problem are compared with the actual potential or magnetic field measurements by computing the squared error between the two (i.e. square of Frobenius norm).

The goal is to minimize this squared error which is our measure of fit. Usually a non-linear search algorithm is applied iteratively to minimize the measure of fit over all

dipole parameters simultaneously. The process is continued until some minimization criterion is met. In simple words, the goal is to identify dipole parameters that best explain the observed field measurements [31].

The three most widely used dipole models for this approach are *fixed dipole model*, *moving dipole model* and *rotating dipole model*. The *fixed dipole model* holds position and orientation constant within a given interval and it estimates the dipole strength for each time point. The *moving dipole model* assumes only one dipole at the time and allows all parameters to vary. The *rotating dipole model* constrains location to a single point but allows orientations and strength to vary [31]. These models have proven useful in both EEG and MEG and remain the most widely used approach to processing experimental and clinical data [1].

In summary, dipole source modeling has proven useful to localize spatially restricted and focal sources such as early sensory evoked potentials. The main limitation of this method is that the exact number of dipoles often cannot be determined a priori, which requires the user to decide the number of dipoles before applying the algorithm[31].

Another concern in using least squares method is being trapped in local minima. As the number of sources increases, nonconvexity of the cost function further increases chances of ending up in local minima. We'll see shortly that there exist other methods that do not require any prior estimate of the number of underlying sources, and also avoid the nonconvexity issue [1]. Beamforming and multiple signal classification (MUSIC) techniques that we discuss next in this section are examples of such techniques. We'll see that MUSIC algorithm, deals with the issue of "number of sources" by trying to decompose the signal to identify underlying components, hence determine the number of sources [31]. Both beamforming and MUSIC avoid the nonconvexity issue by scanning a region of interest (of any desirable size) for possible sources. An estimate of the contribution of each localized source to the data can be derived either via spatial filtering techniques or signal classification indices [1].

4.1.2 Beamforming (linearly constrained minimum variance)

Beamforming is originally a radar technique that has found applications in different fields. In this technique, data from a sensor array is spatially filtered in order to pass signals coming from selected locations of interest, and minimizing (ideally nullifying) contribution of signals from elsewhere [1][32]. By scanning the location of interest throughout the brain, we can monitor all possible source locations in the brain [25].

Due to insufficient degrees of freedom, it's not possible to place a strong stop-band constraint over the entire brain region in beamforming technique. Hence, we can't use a fixed spatial filter for this application. An adaptive spatial filter that has been proposed is *linearly constrained minimum variance (LCMV)* beamforming, in which the limited degrees of freedom are used to nullify interfering sources by placing nulls at their positions. The desired location, at the same time, is represented with a unity gain constraint [1].

The limitation of LCMV method is that sources which are correlated with signal from scanning location will result in partial cancellation of signal of interest [1][32]. We know that neural activity in different parts of the brain often turn out to be correlated, which is bad news for beamforming method. However, recent evaluations suggest that LCMV beamforming can tolerate moderate levels of source or interference correlation [1]. Generally, beamformers work best when there are a limited number of independent components in the data that are not strongly correlated with each other.

Another challenge in this method is that, any errors in the constraint model can result in attenuation or even cancellation of signals, hence the need for more elaborate constraints. But as the number of constraints increases, the degrees of freedom are reduced, and the result is that beamformer becomes less adaptive to other unknown sources. This is another tradeoff that needs to be taken into consideration in beamforming methods [1].

4.1.3 Multiple signal classification (MUSIC)

MUltiple SIgnal Classification (MUSIC) is a signal space scanning method. The procedure it performs is as follows: the data covariance matrix is decomposed into signal and noise subspaces using standard eigen decomposition methods. Sources are assumed to be located at places for which the dipole forward solution is orthogonal to noise subspace [33].

Similar to beamforming, MUSIC also assumes that the sources are discrete and that there are fewer sources than sensors, the sources are uncorrelated and the noise is white. Moreover, partitioning of the data into signal and noise subspaces are more easily performed on averaged data, hence this method might be more difficult to apply to online data [33].

A more recent modification of this method known as recursively applied and projected MUSIC (RAP-MUSIC), projects out each located source before repeating the scanning procedure [33]. MUSIC will be discussed and modeled in more detail as a subspace-based DOA technique in the next chapter.

4.2 Non-parametric (Imaging) Methods

Imaging methods make use of the fact that primary sources which generate EEG/MEG signals are the intracellular currents flowing in the dendrites of cortical pyramidal neurons. As we discussed before, these neurons are aligned normal to the cortical surface. Hence, the cortical surface is divided into tens of thousands of tessellations, and a dipole is assumed at each of the tessellations, with its orientation constrained to be equal to the local surface normal [1].

Such a constraint transforms the inverse problem to a linear one, since the only unknowns in this case are the amplitudes of the dipoles at each tessellation element. The challenge faced in this approach is that the number of sensors used is on the order of 100 while the number of unknowns is on the order of 10,000, which makes the problem severely under-determined. Hence, in order to restrict the range of allowable solutions,

priors or regularization methods are applied in imaging approaches [1], [31], [32]. Some primary methods that fall under this category are discussed in this section.

4.2.1 Bayesian Methods

Bayesian approach incorporates a priori information based on anatomy of head and brain, maximum current strength, smoothness and so on, to determine expectation and variance of the a posteriori source current probability. A priori information can be obtained from other imaging techniques such as functional magnetic resonance imaging (fMRI) or positron emission tomography (PET)[33].

Assume we have a spatio-temporal data matrix M and we intend to estimate a matrix S composed of dipole amplitudes at each tessellation element. In a noise-less data case, the two are related by $M = AS^T$, such that the ith row of S contains the amplitude image across the cortex at time i. Bayes theorem is used to obtain posterior probability for the amplitude matrix S conditioned on the data M, as follows [1]:

$$P(S|M) = \frac{p(M|S)p(S)}{p(M)} \tag{4.1}$$

where $p(M|S)$ is the conditional probability for the data given the image and $p(S)$ is a prior distribution reflecting our knowledge of the statistical properties of the unknown image. Images are typically estimated by maximization of the posterior or log-posterior probability [1]:

$$\begin{aligned} \widehat{\boldsymbol{S}} &= \underset{S}{argmax}\, p(\boldsymbol{M}|\boldsymbol{S})\, p(\boldsymbol{S}) \\ &\equiv \underset{S}{argmax} \ln p(\boldsymbol{M}|\boldsymbol{S}) + \ln p(\boldsymbol{S}) \end{aligned} \tag{4.2}$$

The term $p(M|S)$ depends on the forward model and the true source distribution. However, this noiseless scenario is not realistic. MEG and EEG signals contain additive Gaussian noise that we assume here is spatially and temporally white (generalizations for colored noise are possible). The log likelihood to be maximized is then given by [1]:

$$\ln p(\boldsymbol{M}|\boldsymbol{S}) = \frac{1}{2\sigma^2} \left|\left|\boldsymbol{M} - \boldsymbol{AS}^T\right|\right|_F^2 \tag{4.3}$$

We assume a general exponential density for the prior [1],

$$p(S) = \frac{1}{z}\exp\left(-\beta f(\boldsymbol{S})\right) \tag{4.4}$$

where β and z are scalar constants and $f(\boldsymbol{S})$is a function of the image $\boldsymbol{S}$.

By combining equation (4.4) with the log likelihood, we obtain the negative log posterior. Minimization of the latter is equivalent to maximization of the posteriori that we seek. Hence the problem is reduced to minimization of the following energy function [1]:

$$U(\boldsymbol{S}) = ||\boldsymbol{M} - \boldsymbol{A}\boldsymbol{S}^T||^2 + \lambda\, f(\boldsymbol{S}) \tag{4.5}$$

where $\lambda = 2\beta\sigma^2$.

The rest of the imaging methods mentioned in this section are special cases of minimization of the above energy function [1].

As mentioned before, Bayesian solutions incorporate physiological and anatomical constraints derived from other imaging techniques. Several anatomical/physiological assumptions are used to reduce the solution space a priori, such as: (1) sources are located in gray matter; (2) sources are oriented perpendicularly to the cortical mantle; and (3) sources are locally coherent (i.e., their activity changes smoothly along the cortical mantle). Anatomical information gathered from MRI can be used to enforce the first two constraints. The third assumption be met by imposing spatial smoothness which is mathematically implemented by minimizing differences among neighboring voxels [31].

An important feature of the Bayesian approach is that, by determining a priori the orientation of dipoles, the inverse problem is reduced from a vectorial problem of determining amplitudes and orientations, to a scalar problem of finding the amplitudes of the dipoles [31]

4.2.2 Linear Imaging Methods

As explained at the beginning of this section, imaging techniques make use of some form of regularization or prior on the solution to solve the severely underdetermined (ill-posed) inverse bioelectromagnetic problem [32].

For example, we can view equation (4.5) as a Tikhonov regularization problem, where the first term measures the fit to the data and the last is a regularizing function that measures smoothness of the image. The scalar λ is the regularization parameter that can be chosen using cross-validation methods or the L-curve [1]. For more information about Tikhonov regularization method and L-curve method you can refer to [34] and [35].

One of the first linear imaging solution is called *minimum norm (MN)* solution proposed for MEG by Hämäläinen and Ilmoniemi [36]. In this method, the head model is mapped to a 3-D grid and at each grid point three mutually perpendicular dipole currents are assumed. The goal is to estimate the distribution and amplitudes of these tens of thousands of dipoles, such that they contain the least energy, or equivalently minimum overall current density within the brain. That is, the 3-D source distributions are found such that they fit the actual data with the smallest L-2 norm [31].

A major difference between MN and dipole fitting is that, the dipole model assumes that the brain activity is localized in one or several small areas of the brain; however, MN does not make any a priori assumption about the source distribution, which is an advantage in some cases [33]. However, there is no strong evidence that the solution with smallest L2-norm is the most physiologically plausible one as well. Another issue in MN technique is its tendency to favor weak and localized activation patterns, especially those closer to the cortex surface. Hence, sources that are actually located deep within the brain may get misplaced onto the outermost cortex [31]. Another major shortcoming of the MN approach is that it produces low spatial resolution (blurring) due to the underdetermined nature of the inverse problem in MEG/EEG.

To compensate for these shortcomings of MN, various weighting factors have been suggested. The first, known as the *weighted MN solution*, uses a lead field normalization for compensating for the lower representation of deeper sources .The second, called FOCUSS (Focal Underdetermined System Solution) modifies the weights iteratively according to the solution estimated in a previous step. Specifically, at each step, the weights of grid points with the lowest current density are reduced, and this process is repeated until the current density at most of the grid points is zero [31]. Another method called the Minimum Current Estimate (MCE) utilizes the L1-norm approach. A related method, Magnetic Field Tomography (MFT) utilizes weights and a

regularization parameter which are optimized according to the given experimental geometry and noise.

Another famous minimum norm based method is the algorithm LORETA (LOw Resolution Electromagnetic TomograPhy). This algorithm introduces a spatial second derivative operator (Laplacian) into the weighting function and selects the solution with the smoothest spatial distribution by minimizing the Laplacian of the current sources [31]. The smoothness requirement comes from the neighboring points in the brain are likely to be synchronized. Another assumption behind this method is that the scalp-recorded signal originates mostly from cortical gray matter, which constrains the solution space to cortical gray matter (and hippocampi). The method produces low spatial resolution that is a consequence of the smoothness constraint [33][31].

4.2.3 Signal Space Projection (SSP)

Signal space projection (SSP) is a spatial filter method that can separate signal from noise on the basis of their relationship in signal space. It relies on the assumption that component vectors corresponding to different neuronal sources have distinct and fixed directions in signal space, and only their amplitudes change with time. If we can get these signal vectors from the patterns in the data, we do not even need a source model for SSP. However, if we assume current dipole source models, SSP will be reduced to estimating dipole parameters only [33].

If known dipole sources are each assigned such a vector, SSP can be used as a spatial filter that passes only signals corresponding to these known sources. Parallel projection operators are constructed from the forward solutions of the dipole sources of interest and multiplied by the signal measurements to obtain the spatial filter output. Moreover, if the vectors corresponding to artifact patterns are known, SSP can use orthogonal projection to eliminate them [33].

The shortcoming of SSP method is that it does not perform well when the source signals subspace is not completely orthogonal to noise subspace [33].

CHAPTER 5

PRINCIPLES OF ARRAY PROCESSING

In this chapter we review fundamentals of narrowband array models. We use the simplest array geometry, which is uniform linear array, to explain the basic concepts such as propagation delay and spatial covariance matrix. In these formulations, the array is assumed to be in the far field of the source.

It should be noted that he array geometry required for EEG/MEG inverse problem is definitely not linear. However, the same concepts and models of 1-D array can be easily extended to 2-D and 3-D arrays when necessary. Moreover, the electric/magnetic fields in the bioelectromagnetic inverse problem, are not in the far-field. In fact, we deal with near-field scenarios. So the appropriate near-field formulae should be used when phased array technique is applied to this specific application.

However, uniform linear array in the far-field is a simple scenario that is usually used to explain the basics of array processing. In the following sections a narrowband signal received by a uniform linear array is approximated; next, the spatial covariance matrix is formed; later, this matrix is decomposed into signal and noise subspaces which are later used in subspace based DOA techniques.

5.1 Uniform Linear Arrays

Consider a uniform linear array consisting of N elements (antennas/sensors) numbered from 0 to $N-1$, displaced by a distance D from each other as shown in figure (26). Imagine a wave propagating towards these array elements. The wave will be received by each antenna element at a slightly different time (hence phase), due to the difference in the lengths of paths to be traveled towards each element. If we assume the phase of the signal s(t) received at element 0 is zero, we can find the phase of the signals received at each of the other elements, considering the extra length the signal has to travel to reach each element. From the geometry of the problem we can see that the signal path difference between two elements is $Dsin(\theta)$. Hence, the additional time spent for the

wave to travel this distance equals the distance over the speed of propagation, i.e. speed of light. Therefore, for the kth element, distance kD from the first element, the time delay of signal arrival compared to first element would be [37]:

$$\Delta t_k = \frac{kDsin\,\theta}{c} \tag{5.1}$$

Where c is the speed of light.

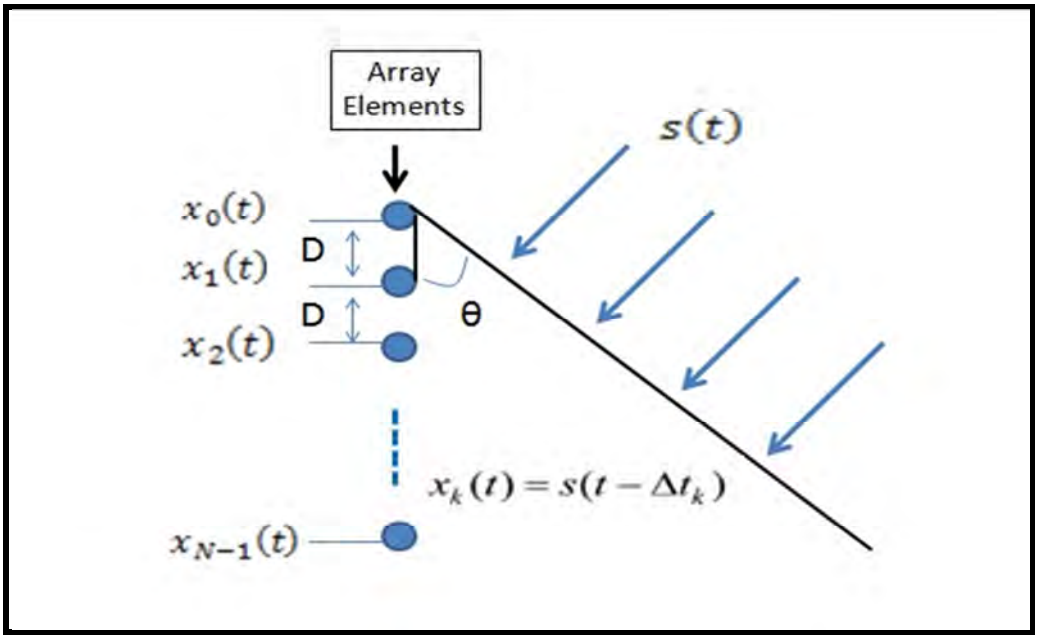

Figure 5.1:Uniform linear array geometry

For a ***narrowband*** signal $s(t)$, Let the nth sample of the signal at the kth element be denoted as $x_k[n]$ [37].

$$x_k[n] \approx s[n]e^{-j2\pi f_c \Delta t_k} \tag{5.2}$$

where f_c is the center frequency of the narrowband signal and the exponential term takes care of the phase difference compared to the first element. We also know that $c = \lambda f_c$, where λ is the wavelength of the signal. We can also express the element spacing in wavelength as $d = D/\lambda$. Hence, by substituting the value of Δt_k from equation 3, we can rewrite equation (5.2) as [37]:

$$x_k[n] \approx s[n]e^{-j2\pi kd\,sin\theta} \tag{5.3}$$

Note that, to avoid aliasing in space the distance D between the elements should be $\lambda/2$ or less. For example, for $D = \lambda/2$ we get $d = 1/2$ which simplifies equation (5.3) to [37]:

$$x_k[n] \approx s[n]e^{-j\pi n\, sin\theta} = s[n]a_k(\theta) \tag{5.4}$$

Now, if there are r signals present, the nth sample of the ith signal is denoted as $s_i[n]$ where $i = 0, 1, \dots, r-1$. Hence, the baseband sampled signal at the kth element can be expressed as [37]:

$$x_k[n] \approx \sum_{i=0}^{r-1} s_i\,[n]a(\theta_i) \tag{5.5}$$

By accounting for all array elements $(k = 0, 1, \dots, N-1)$ and considering additive noise $v_k[n]$ at each element, we can rewrite equation (5.5) in a matrix form as follows [37]:

$$\begin{bmatrix} x_0[n] \\ x_1[n] \\ . \\ . \\ x_{N-1}[n] \end{bmatrix} = \begin{bmatrix} a_0(\theta_0) & a_0(\theta_1) & \cdots & a_0(\theta_{r-1}) \\ a_1(\theta_0) & . & \dots & . \\ . & . & \dots & . \\ . & . & \dots & . \\ a_{N-1}(\theta_0) & . & \cdots & a_{N-1}(\theta_{r-1}) \end{bmatrix} \begin{bmatrix} s_0[n] \\ s_1[n] \\ . \\ . \\ s_{r-1}[n] \end{bmatrix} + \begin{bmatrix} v_0[n] \\ v_1[n] \\ . \\ . \\ v_{N-1}[n] \end{bmatrix}, \tag{5.6}$$

For simplification in notation, we intrdouce the $N \times 1$ vectors $\boldsymbol{x}_n, \boldsymbol{v}_n$, and $r \times 1$ vector $\boldsymbol{s}_n$, to denote the received signals vector, uncorrelated noise vector at each antenna element and transmitted signals vector, respectively. Also the $N \times r$ matrix $\boldsymbol{A}$ is defined to help write matrix in equation (5.6) in a more compact form as follows [37]

$$\begin{aligned} \boldsymbol{x}_n &= [\, \boldsymbol{a}(\theta_0)\ \boldsymbol{a}(\theta_1)\ \dots\ \boldsymbol{a}(\theta_{r-1})]\, \boldsymbol{s}_n + \boldsymbol{v}_n \\ &= \boldsymbol{A}\boldsymbol{s}_n + \boldsymbol{v}_n \end{aligned} \tag{5.7}$$

Of course if we assume there is no noise, the above equation simplifies to [37]:

$$\boldsymbol{x}_n = \boldsymbol{A}\boldsymbol{s}_n \tag{5.8}$$

The columns of matrix $\boldsymbol{A}$, denoted by $\boldsymbol{a}(\theta_i)$, are called the *steering vectors* of the signals $s_i(t)$. If the angles of arrival of the r signals are different, the steering vectors form a

linearly independent set, which can be used to find the corresponding angles. All possible steering vectors put together form an *array manifold*. From equation (36) we can see that the data vector $\boldsymbol{x}_n$ is a linear combination of the columns of $\boldsymbol{A}$. Hence, the steering vectors span the *signal subspace*. We will see later on how the subspace concept finds applications in direction of arrival (DOA) techniques [37].

5.1.1 Spatial Covariance Matrix

In order to compute the spatial covariance matrix of an array we have to make a couple of assumptions. First, we assume that the signal and noise vectors $\boldsymbol{s}_n$ and $\boldsymbol{v}_n$ are uncorrelated, hence they have orthogonal subspaces. Second, we assume the noise vector to be Guassian with zero mean and correlation matrix $\sigma^2\boldsymbol{I}$, which means the noise at different elements are uncorrelated [37].

$$\begin{aligned}\boldsymbol{R}_{xx} = E[\boldsymbol{x}_n\,\boldsymbol{x}_n^H] = E[(\boldsymbol{A}\boldsymbol{s}_n + \boldsymbol{v}_n)(\boldsymbol{A}\boldsymbol{s}_n + \boldsymbol{v}_n)^H] \\ = \boldsymbol{A}E[\boldsymbol{s}_n\,\boldsymbol{s}_n^H]\boldsymbol{A}^H + E[\boldsymbol{v}_n\,\boldsymbol{v}_n^H]\end{aligned} \tag{5.9}$$

The signal correlation matrix is: $\boldsymbol{R}_{ss} = E[\boldsymbol{s}_n\,\boldsymbol{s}_n^H]$. So we can write equation (5.9) as [37]:

$$\boldsymbol{R}_{xx} = \boldsymbol{A}\boldsymbol{R}_{ss}\boldsymbol{A}^H + \sigma^2\boldsymbol{I}_{N\times N} \tag{5.10}$$

Since the matrix $\boldsymbol{R}_{xx}$ is Hermitian (complex conjugate transpose) it has real eigen values and can be unitarily decomposed. We will show in the next few lines that any vector, $\boldsymbol{q}_n$, which is orthogonal to the columns of $\boldsymbol{A}$, is also an eigenvector of $\boldsymbol{R}_{xx}$ [37]:

$$\boldsymbol{R}_{xx}\boldsymbol{q}_n = (\boldsymbol{A}\boldsymbol{R}_{ss}\boldsymbol{A}^H + \sigma^2\boldsymbol{I})\boldsymbol{q}_n = 0 + \sigma^2\boldsymbol{I}\boldsymbol{q}_n = \sigma^2\boldsymbol{q}_n \tag{5.11}$$

From equation (5.11) it's clear that $\boldsymbol{q}_n$ is an eigenvector of $\boldsymbol{R}_{xx}$, and its corresponding eigen value is σ^2, which is the noise power. If we make sure that $N > r$, since $\boldsymbol{A}$ is an $N \times r$ matrix, there are $N - r$ linearly independent vectors such as $\boldsymbol{q}_n$, with eigenvalues equal to σ^2. These vectors span the *noise subspace* [37].

Now assume $\boldsymbol{q}_s$ is an eigenvector of $\boldsymbol{A}\boldsymbol{R}_{ss}\boldsymbol{A}^H$, we can show that $\boldsymbol{q}_s$ is also an eigenvector of $\boldsymbol{R}_{xx}$ as follows:

$$\begin{aligned}\boldsymbol{R}_{xx}\boldsymbol{q}_s = (\boldsymbol{A}\boldsymbol{R}_{ss}\boldsymbol{A}^H + \sigma^2\boldsymbol{I})\boldsymbol{q}_s = \sigma_s^2\boldsymbol{q}_s + \sigma^2\boldsymbol{I}\boldsymbol{q}_s \\ = (\sigma_s^2 + \sigma^2)\boldsymbol{q}_s\end{aligned} \tag{5.12}$$

The corresponding eigenvalue is $(\sigma_s^2 + \sigma^2)$, where σ_s^2 is the eigenvalue of $\boldsymbol{A}\boldsymbol{R}_{ss}\boldsymbol{A}^H$. Also note that the vector $\boldsymbol{A}\boldsymbol{R}_{ss}\boldsymbol{A}^H\,\boldsymbol{q}_s$ is nothing more than a linear combination of the columns of $\boldsymbol{A}$. Therefore, eigenvector $\boldsymbol{q}_s$ lies in columnspace of $\boldsymbol{A}$. As a result, r linearly independent eigenvectors of $\boldsymbol{R}_{xx}$ span the *signal subspace* [37].

To summarize, there are two important points to be mentioned here:

- Signal and noise subspaces are orthogonal to each other,
- If the eigenvalues of $\boldsymbol{R}_{xx}$ are listed in descending order, the first largest r eigenvalues correspond to eigenvectors that span the *signal subspace*, and the remaining $N - r$ eigenvalues have eigenvectors that span the *noise subspace*.

Hence, we can decompose $\boldsymbol{R}_{xx}$ as:

$$\boldsymbol{R}_{xx} = \boldsymbol{Q}\boldsymbol{D}\boldsymbol{Q}^H = [\,\boldsymbol{Q}_s\;\;\boldsymbol{Q}_n\,]\begin{bmatrix}\boldsymbol{D}_s & 0\\ 0 & \sigma^2\boldsymbol{I}\end{bmatrix}[\,\boldsymbol{Q}_s\;\;\boldsymbol{Q}_n\,]^H \qquad (5.13)$$

where $\boldsymbol{Q}_s$ is an $N \times r$ matrix whose columns are the r eigenvectors that span the *signal subspace;* $\boldsymbol{Q}_n$ is an $N \times (N - r)$ matrix whose columns are the eigenvectors that span the *noise subspace*. Matrix $\boldsymbol{D}$ is a diagonal matrix that has the eigenvalues of $\boldsymbol{R}_{xx}$ along its main diagon. $\boldsymbol{D}$ is subsequently partitioned into $\boldsymbol{D}_s$ and $\sigma^2\boldsymbol{I}_{N\times N}$ .Matrix $\boldsymbol{D}_s$ is an $r \times r$ diagonal matrix containing "signal" eigenvalues, and $\sigma^2\boldsymbol{I}_{N\times N}$ is an $(N - r) \times (N - r)$ scaled identity matrix containing the $(N - r)$ noise eigenvalues [37].

We can also find the eigenvectors of autocorrelation matrix by using the data matrix $\boldsymbol{X}$ and singular value decomposition (SVD) method [37]. Note that, in real cases usually $\boldsymbol{R}_{xx}$ is not known and we have to estimate it from finite data snapshots that we have. In such cases, we estimate the spatial covariance matrix using the sample spatial covariance matrix as follows:

$$\boldsymbol{R}_{xx} = \frac{1}{K}\sum_{i=0}^{K-1} x_n x_n^H \qquad (5.14)$$

where K is the number of snapshots of data available from array elements.

5.2 Classical Methods for Direction of Arrival Estimation (DOA)

Two classical techniques in this category are *delay-and-sum* and *minimum variance distortionless response (MVDR).* These methods are based on beamforming. The idea is to scan a beam through space and measure the power received from each direction. Maximum power received corresponds to the location of interest [37].

5.2.1 Delay-and-Sum Method (Classical Beamformer)

In this method, powers from all possible directions of arrival (DOA) are measured and the angle that yields the maximum power is chosen as DOA. To test each angle, a beam is formed in that direction and the beamformer weights are set to be the steering vector of that direction. Hence, we get the output power of the beamformer as [37]:

$$P(\theta) = E[\boldsymbol{y}^H \boldsymbol{y}] = E|\boldsymbol{w}^H \boldsymbol{X}_n|^2 = E|\boldsymbol{a}(\theta)^H \boldsymbol{X}_n|^2 = \boldsymbol{a}(\theta)^H \boldsymbol{R}_{xx} \boldsymbol{a}(\theta) \qquad (5.15)$$

$P(\theta)$ will have peaks when $\mathbf{w}$ is equal to the steering vectors of DOA angles.

The disadvantage of this method is that the only way to improve the DOA resolution is to increase the number of antenna elements in the array. As we will see shortly, subspace methods that make use of the subspace decomposition described earlier in this chapter, will yield much higher resolution than classical methods [37].

5.2.2 Capon's Minimum Variance Distortionless Response Method (MVDR)

MVDR also measures the power of the received signal in all possible directions. The power from the DOA, θ, is measured by constraining the beamformer gain to be 1 in that direction and using the remaining degrees of freedom to minimize the contributions to the output power from signals coming from all other directions. The problem can be stated mathematically as [37]:

$$\min_{\boldsymbol{w}} E[|y(k)|^2] = \min_{\boldsymbol{w}} \boldsymbol{w}^H \boldsymbol{R} \boldsymbol{w} \qquad (5.16)$$

$$\text{with constraint: } \boldsymbol{w}^H \boldsymbol{a}(\theta) = 1$$

Hence, the weights of the beamformer are found to be [37]:

$$\boldsymbol{w} = \frac{\boldsymbol{R}^{-1}\,\boldsymbol{a}(\theta)}{\boldsymbol{a}^{\boldsymbol{H}}(\theta)\,\boldsymbol{R}^{-1}\,\boldsymbol{a}(\theta)} \tag{5.17}$$

The disadvantage of this method is that an inverse matrix computation is required which may become ill-conditioned if highly correlated signals are present. This method, however, provides higher resolution than the delay-and-sum beamformer [37].

5.3 Subspace Methods for DOA Estimation

In subspace-based methods we estimate the autocorrelation of the signal and the noise model to form a matrix (spatial covariance matrix) whose eigenstructure yields signal and noise subspaces, as discussed in section 4.1.1 of this report. We'll see shortly how these subspaces help find high resolution DOA estimates [37].

5.3.1 Multiple Signal Classification Algorithm (MUSIC)

We showed in section 5.1.1, that the steering vectors span the signal subspace and are therefore orthogonal to the noise subspace. In MUSIC method, we perform a search through the set of all possible steering vectors and find those that are orthogonal to the noise subspace. If **a**(θ) is the steering vector corresponding to one of the incoming signals, then it is orthogonal to the noise subspace, that is [37]:

$$\boldsymbol{a}(\theta)^{H}\boldsymbol{Q}_n = 0 \tag{5.18}$$

Where $\boldsymbol{Q}_n$ denotes the noise subspace, spanned by the $N - r$ eigenvectors of the spatial covariance matrix ($\boldsymbol{R}_{xx}$) that correspond to its $N - r$ smallest eigenvalues derived from eigenvalue decomposition, as displayed in section 5.1.1.

In practice, $\boldsymbol{a}(\theta)$ will not be precisely orthogonal to the noise subspace due to errors in estimating $\boldsymbol{Q}_n$. However, we can form a function which will have large peaks at $\theta's$ that correspond to DOA of each of the signals [37]:

$$P_{\boldsymbol{MUSIC}}(\theta) = \frac{1}{\boldsymbol{a}^{H}(\theta)\boldsymbol{Q}_n\boldsymbol{Q}_n^{H}\boldsymbol{a}(\theta)} \tag{5.19}$$

The above function is known as the multiple signal classification (MUSIC) *spectrum*. Hence, the MUSIC algorithm first estimates a basis for the noise subspace, $\boldsymbol{Q}_n$,

and then determines the r peaks in (5.19); the associated angles provide the DOA estimates [37]. The MUSIC algorithm has high resolution and can be used with a variety of array geometries.

The disadvantage of the MUSIC algorithm is that it is not able to identify DOAs of correlated signals and is computationally expensive because it involves a search over the function P_{MUSIC} for the peaks [37]. A widely used method for overcoming the latter challenge for MUSIC is s*patial smoothing*, which is actually essential in multipath propagation environments. To perform spatial smoothing, the array is divided up into smaller, possibly overlapping subarrays and the spatial covariance matrix of each subarray is averaged to form a single, spatially smoothed covariance matrix. The MUSIC algorithm is then applied on the spatially smoothed matrix. This approach helps improve resolvability of closely placed sources using MUSIC [37].

CHAPTER 6

METHODOLOGY

6.1 Software Choice

In order to solve the bioelectromagnetic *inverse problem*, one has to solve the *forward problem* first. To solve the forward problem, one has to choose an appropriate *model for the sources* of activity in the brain and a suitable *head model*, and then calculate the expected electric potentials/magnetic fields produced on/outside the scalp. Later on, the inverse problem uses these produced fields to try and recover the underlying neural activity in the brain.

Hence, the first step in developing a signal processing algorithm to solve the inverse problem of bioelectromagnetism would be choosing appropriate source and head models. Neural activity of the brain has been widely modeled as *current dipoles.* The head model, however, is more complicated. Different head models have been proposed and developed over the years: single sphere, multiple spheres, and realistic head models.

In a recent paper [38], Sylvain Baillet et al. presented a summarized comparison of the available features of the existing free academic softwares for electromagnetic brain mapping using EEG and MEG. In order to choose an all-in-one software package, the following features of each software package have been compared:

- time-series analysis,
- time-frequency analysis and decomposition,
- MEG/EEG forward modeling and/or source modeling
- statistical analysis,
- graphical user interface versus scripting libraries,
- interoperability with other software packages/the possibility for users to develop plugins,
- the computing environment and the operating system(s) (OS) required,

The comparison results for the existing free all-in-one packages have been summarized in Table 1. Purple filled squares denote availability of the feature.

Table 1: Academic Software for Brain Signal Analysis [38]

Featured software packages	Time-series analysis	Time-frequency analysis	Forward modeling	Source modeling	Statistical analysis	Graphical user interface	Interoperability (other software packages/user plugins)	Environment/OS
BrainStorm							User plugins	Matlab/ multiple
CARTOOL								Windows
eConnectome								Matlab/ multiple
EEGLAB,SIFT, NFT, BCILAB & ERICA							EEGLAB, FieldTrip; user plugins	Matlab/multiple
ELAN							Matlab, SPM, FieldTrip, NUTMEG	Compiled C/multiple (virtual machine)
EMEGS							SPM8; User plugins	Matlab/ multiple
FieldTrip							BESA, EEGLAB, LORETA,SPM8; userplugins	Matlab/ multiple
MNE							Matlab	C/C++ (Linux/MacOS)
NUTMEG							FieldTrip, SPM, OpenMEEG,ELAN,	Matlab/ multiple; Python
sLORETA								Windows
SPM8							FieldTrip,BioSig; user plugins	Matlab/ multiple

Based on the needs of this thesis, the criteria for a suitable software were set as follows:

1. Accurate forward modeling
2. Time series and time-frequency analysis capability
3. Matlab based environment (to ease handling the data and applying signal processing techniques)
4. Graphical User Interface

Forward Modeling is the first important criterion on the list. Hence, each software was investigated for the method used in its forward modeling, and how accurate the results are in each case. All the software packages can produce spherical head models, but spherical representation of the head is a crude approximation that causes localization errors in real cases, especially for EEG application. Hence, the softwares that can produce more realistic head models are more useful for the purpose of this research. Realistic head models are usually generated by applying Finite Element Method (FEM) or Boundary Element Method (BEM) on multiple images from the anatomy of a head. As mentioned in section 3.5.3 of this report, BEM technique assumes isotropy and homogeneity for each layer of the head, while FEM can account for anisotropy and inhomogeneousness of different head surfaces. Hence, FEM is a more realistic and a superior technique compared to BEM. However, applying FEM to a complicated volume such as the human head is very challenging. At this time (December 2011), none of the free all-in-one packages for brain signal analysis offer an FEM computation for human head anatomy. Only a dedicated software named Simbio can implement such FEM calculation for the human head [39]. The author contacted the developers of this software through email for getting access to the code. Dr. Carsten Wolters, from Institute for Biomagnetism and Biosignalanalysis in University of Münster, Germany replied and explained that this software is not easy to use without proper support from the developers; and that this kind of support can only be provided if there is a common research project between the two universities. However, they are trying to integrate the FEM calculations into FieldTrip software in the near future [40].

Hence, the next best option was to look into softwares that provide realistic head models using BEM techniques. Literature review was performed in order to compare the accuracy of BEM solvers used in each of the candidate softwares. An almost thorough comparison has been made in [41] among publicly available M/EEG forward solvers, which are: MNE, Brainstorm (without OpenMEEG), EEGLAB (via the NFT Toolbox), Fieldtrip, Simbio, OpenMEEG and SPM [41]. The accuracy of forward solvers can be assessed for simple geometries such as nested spheres, by comparison with analytical results. Paper [41] provides such accuracy comparison for the above BEM solvers (except NFT toolbox). The conclusions are as follows:

- When comparing accuracy of electrical potential simulations in EEG forward modeling, it was found that OpenMEEG provides the most precise solutions [41]
- By comparing accuracy of magnetic fields simulated in MEG forward modeling, the authors found that the OpenMEEG and Simbio solvers take the lead for radially oriented sensors with similar results for both [41]

Hence, OpenMEEG was chosen as the most plausible candidate for forward modeling. However, OpenMEEG is not an all-in-one package; rather, it specializes in EEG/MEG realistic head modeling for forward problem .OpenMEEG has recently been made available in few all-in-one packages, which are SPM, FieldTrip, and Brainstorm. All three of the above have MATLAB environment, which is great news. Fieldtrip is a strong tool, but it does not have a graphical interface. SPM and Brainstorm have graphical interfaces, with Brainstorm having the lead in user-friendly graphical interfaces and comprehensive online tutorials.

Finally, after thorough investigation, Brainstorm was chosen as the software used in this thesis [42].

6.2 The Forward Problem Solution

As it was explained earlier in this thesis, in order to solve the inverse problem of bioelectromagnetics, one needs an appropriate solution to the forward problem first; i.e. one needs to produce mathematical models for the sources of brain activity assuming the head as a conductive medium. Using these models and some constraining assumptions, one can estimate the electric/magnetic signals that would appear outside the head as the result of brain neural activity. These signals can be recorded with suitable sensors.

In this chapter, the procedure of obtaining an appropriate solution to the forward problem using the dedicated softwares Brainstom and OpenMEEG, is described. Next, it is demonstrated how synthetic brain signals are generated from the acquired forward solution. In the next chapter, these artificial EEG/MEG signals are used to tackle the inverse problem of bioelectromagnetics.

6.2.1 Source modeling in Brainstorm

Brainstorm works with a distributed source modeling assumption. In this approach, the brain (usually only cortex surface) is divided into thousands of grid points, each of which is assumed to hold a current dipole. The software assumes a unit amplitude (1A.m) dipole at each vertex of the grid and computes the resulting electric/magnetic fields that a set of sensors outside the head would record. Once this procedure is carried out for each dipole on the grid, a lead-field matrix is created. This matrix has dimensions of $N \times M$, where N is the number of sensors (array size) and M is the number of sources (dipoles).

For the simulations of this research, a grid with 15000 vertices is used. As a result, adjacent dipoles are spaced a few millimeters (3-5mm) apart. Standard EEG or MEG caps are assumed as the sensor array to collect desired electric/magnetic signals.

6.2.2 Head Anatomy in Brainstorm

The first step in creating a head model in brainstorm is creating a new protocol and defining a new subject. Next, one has to import the anatomy of the subject's head into the software. This comprises of a series of MRI images of the head. Next, the head surfaces (scalp, skull, and cortex) are imported to the protocol. These surfaces are

obtained using other softwares (such as BrainVisa, BrainSuite, and FreeSurfer) that perform segmentation of MRI images.

Brainstorm offers one default head anatomy called the *Colin27* anatomy. It is based on the *Colin27* MRI volume provided by the Montreal Neurological Institute (MNI), which is an average of 27 T1-weighted scans of Colin Holmes brain [43]. For part of the simulations in this paper, Colin27 anatomy is used. Later, a second head anatomy is introduced for comparison purposes. Figure 6.1 shows the three anatomical surfaces extracted from Colin's head anatomy. Figure 6.2 shows the MRI scan of the same head, comprising of three views: sagittal, coronal and axial. Sagittal plane is an imaginary vertical plane that passes from front to rear, dividing the head into right and left sections. Coronal plane, on the other hand, is an imaginary vertical plane that divides the head into front and back sections. Axial, or transverse plane, is another imaginary plane which is horizontal and divides the head to superior and inferior sections. The three planes are perpendicular to each other, and are used to give a better view of the brain.

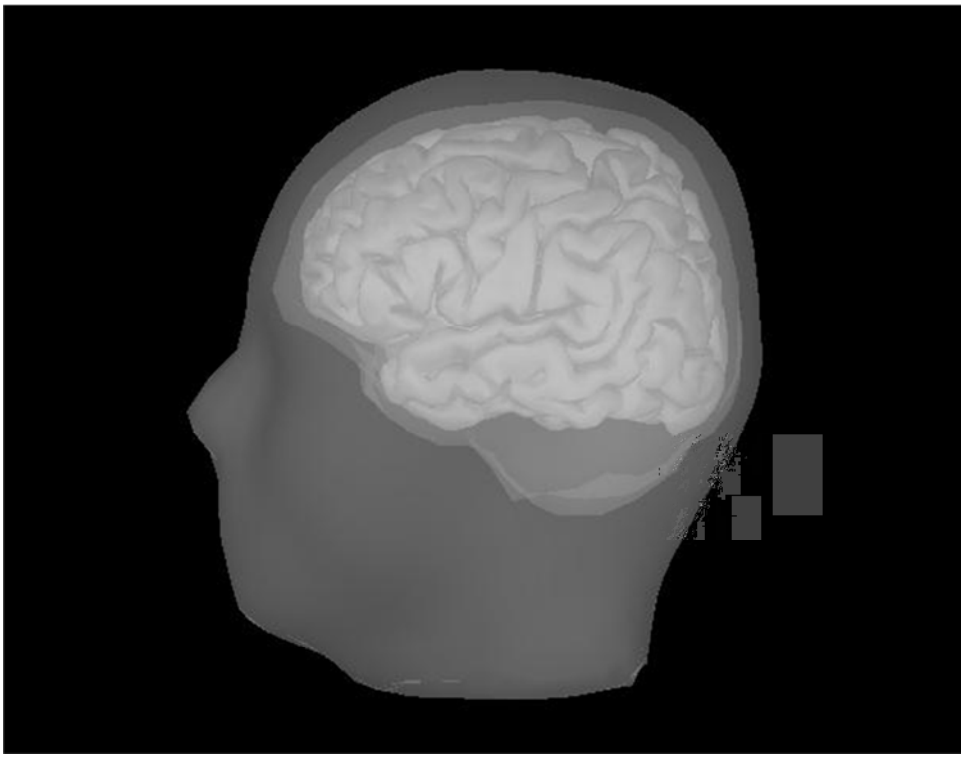

Figure 6.1: Colin Head showing the three anatomical surfaces (developed in Brainstorm)

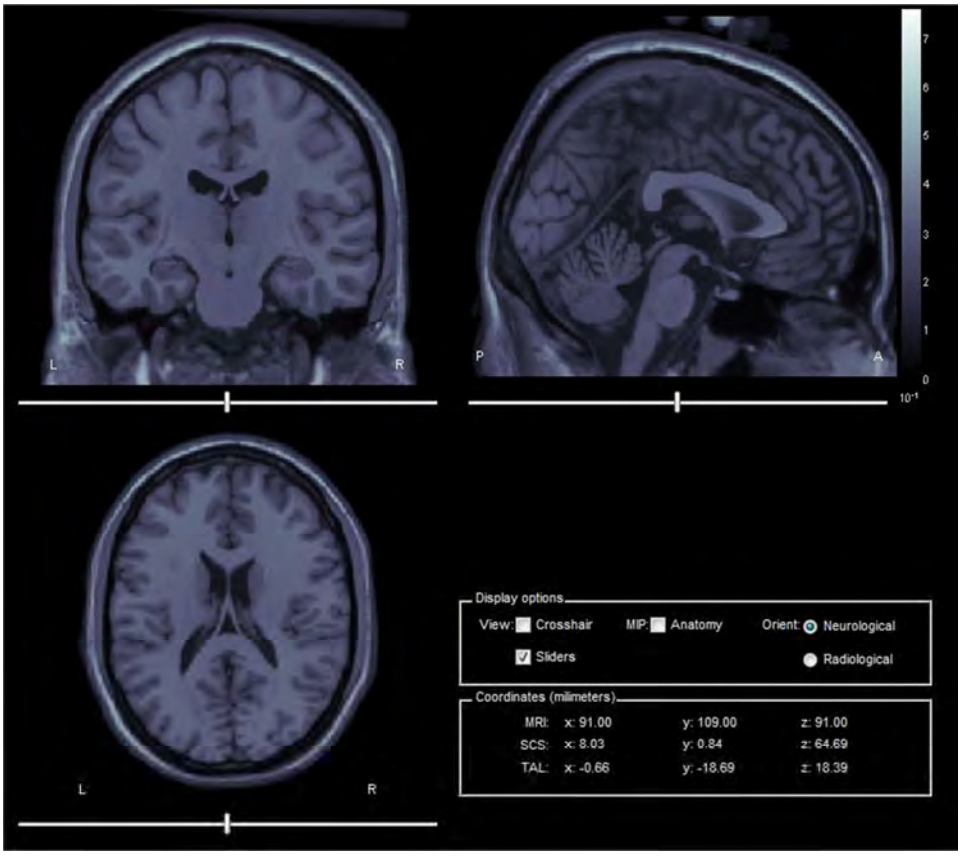

Figure 6.2: Colin MRI: Top left: coronal view, top right: sagittal view, bottom: axial view (developed in Brainstorm)

Figure 6.3-Figure 6.5 show the three layers of Colin's head anatomy, tessellated into small triangular areas; they depict cortex surface; inner-skull layer; and the head (scalp) respectively. It should be mentioned that Brainstorm has these segmented layers available only for Colin's anatomy; hence, any other head anatomy needs to go under the segmentation process, using other software, before being imported to Brainstorm.

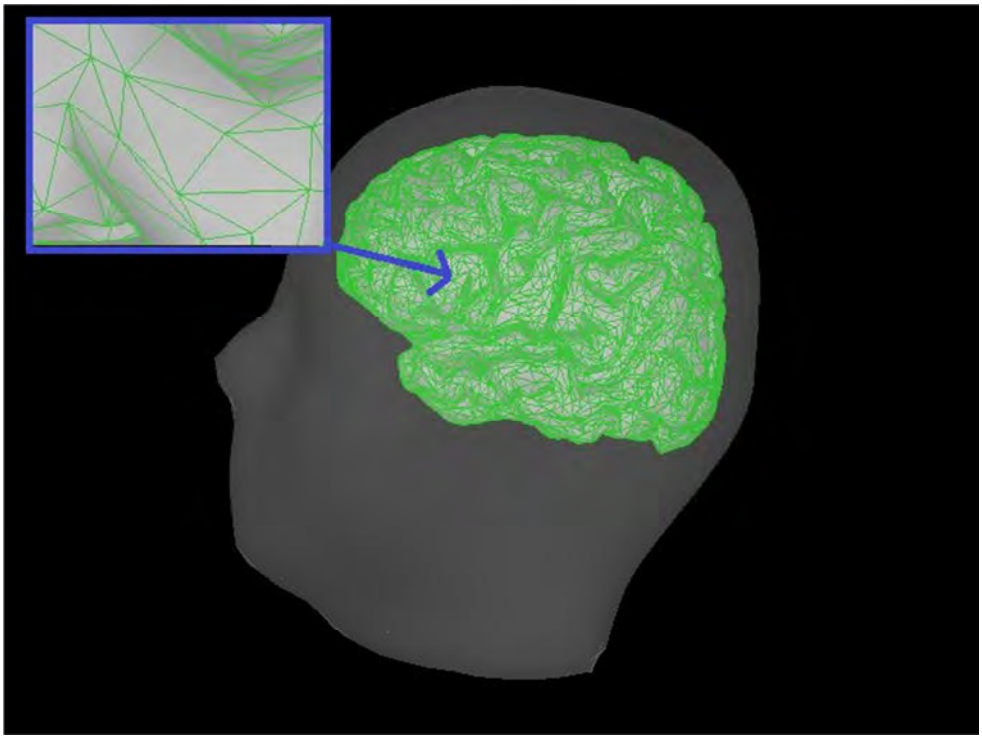

Figure 6.3: Colin anatomy: tessellated cortex (developed in Brainstorm)

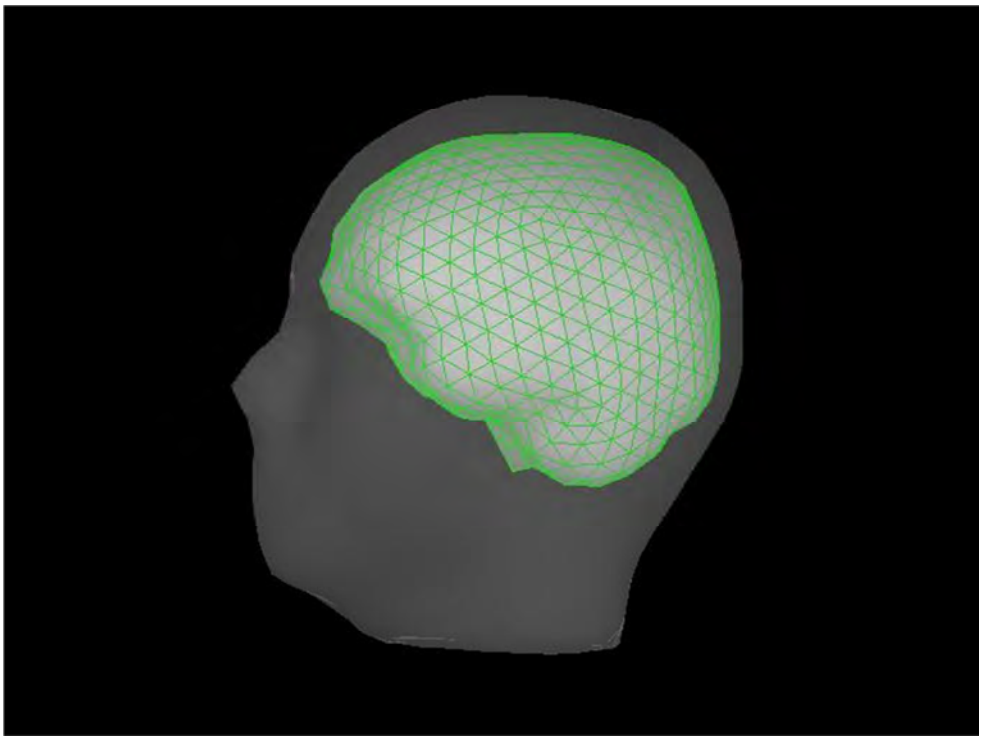

Figure 6.4: Colin anatomy: tessellated Inner skull (developed in Brainstorm)

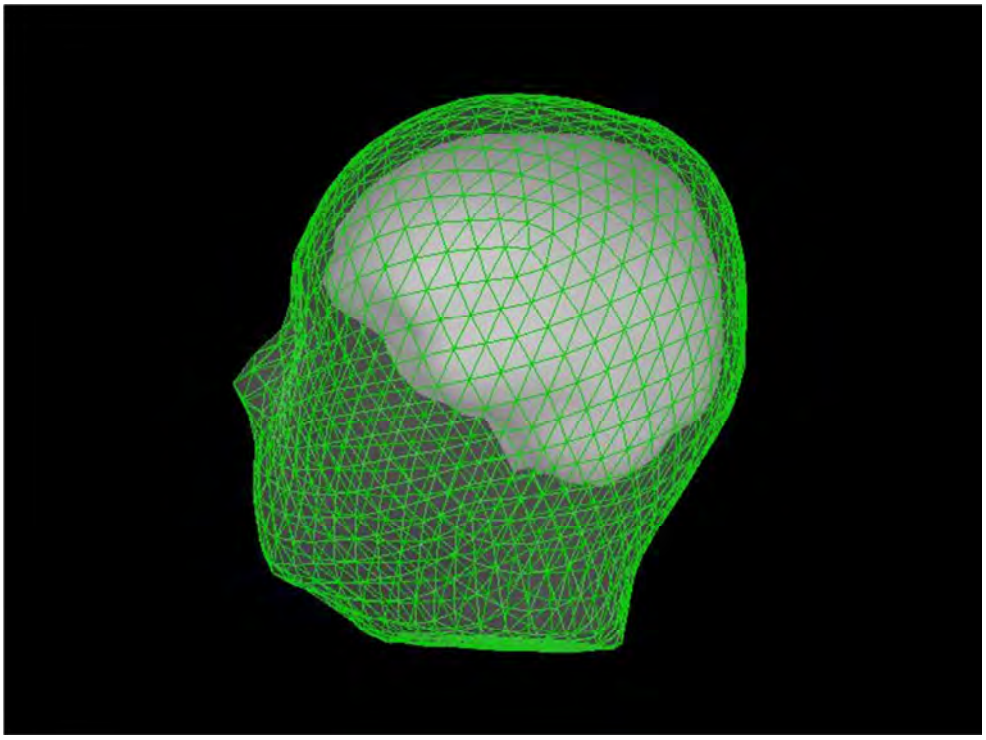

Figure 6.5: Colin anatomy: tessellated scalp (developed in Brainstorm)

6.2.3 Head Model in Brainstorm

This software is capable of producing spherical shells to represent different head anatomies. For EEG, the famous three-shell model uses three concentric spheres with different diameters to represent cortex, skull and scalp. Figure 6.6 shows one of the spheres of a 3-shell spherical head model developed in brainstorm for EEG. The computations for a spherical head model are done using Berg's three-layer sphere model for EEG in Brainstorm [44].

For MEG, a single sphere model is the simplest that can be used. A more complex spherical model developed for MEG is the overlapping spheres model [25], which was explained in section 3.5.3 of this thesis. Overlapping spheres model is a supposed to provide an easy-to-compute approximation to a realistic head model.

Figure 6.7 and Figure 6.8 depict two out of 151 spheres from an overlapping spheres head model generated in Brainstorm.

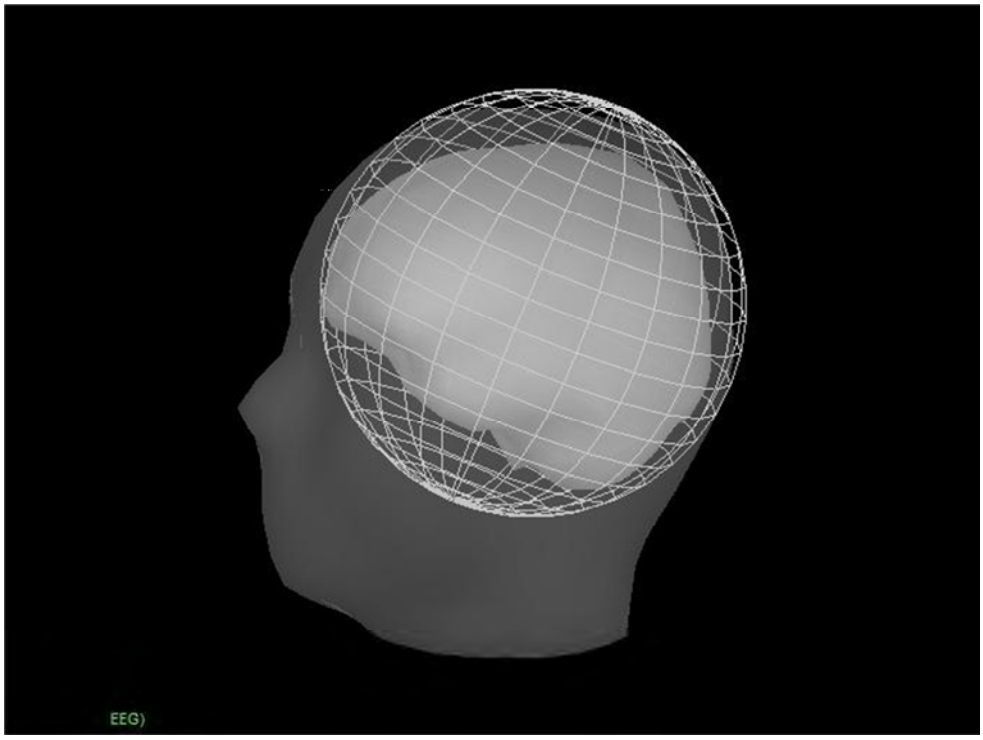

Figure 6.6: Spherical Head Model (developed in Brainstorm)

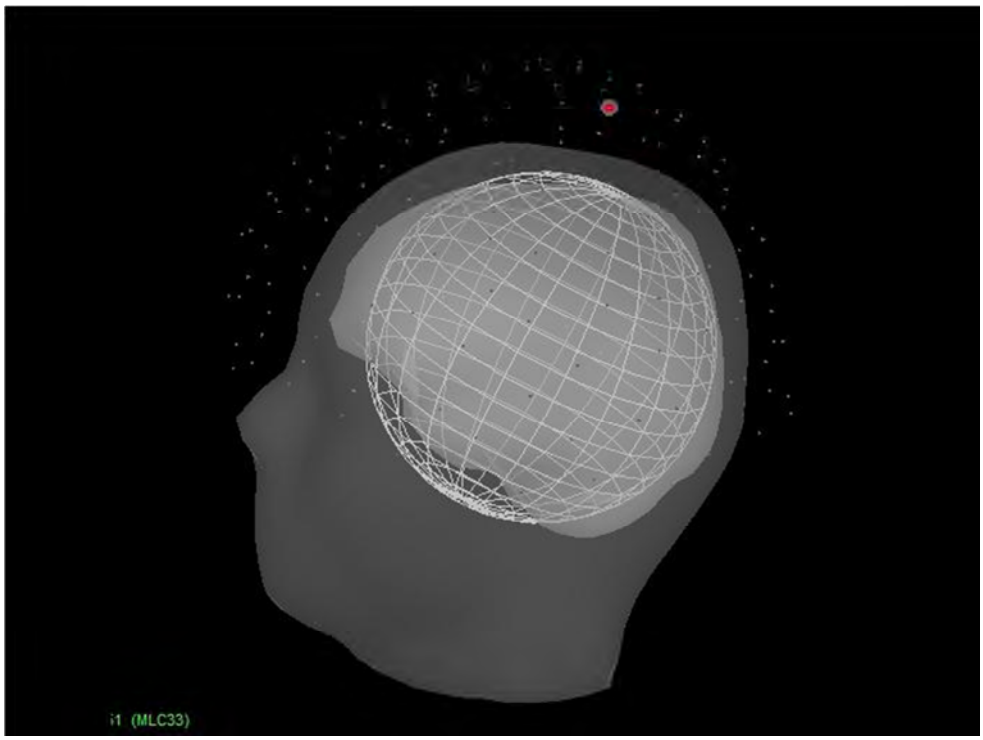

Figure 6.7: Overlapping Spheres model example (developed in Brainstorm)

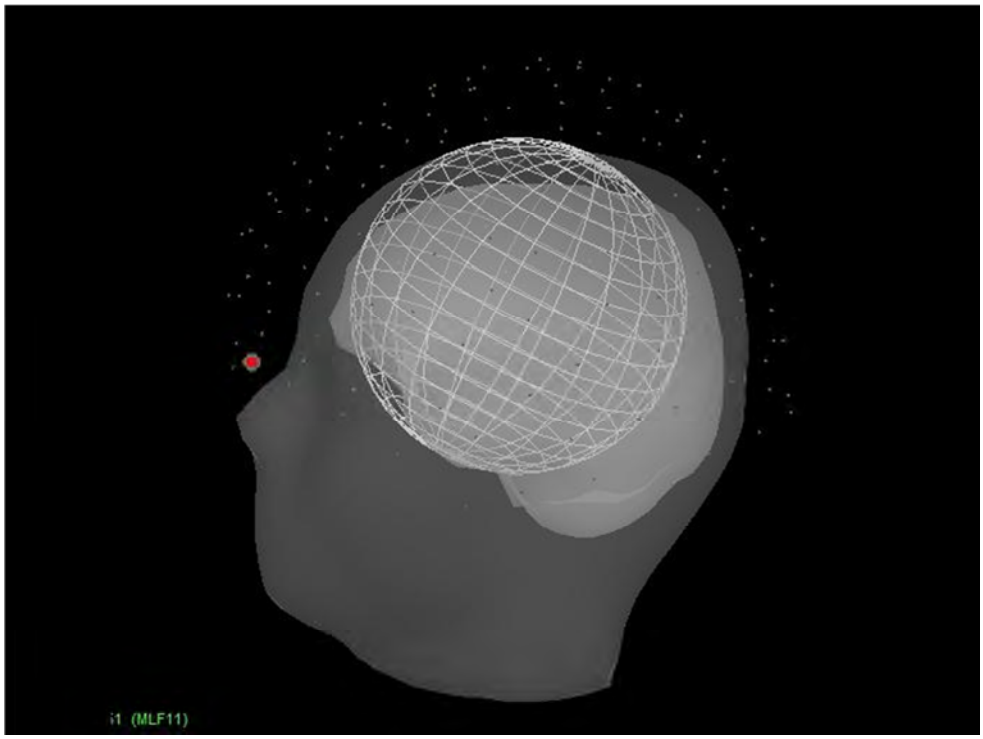

Figure 6.8: Overlapping Spheres model example (developed in Brainstorm)

Realistic head models can be computed in Brainstorm using OpenMEEG software which has recently been integrated with Brainstorm. This software uses symmetric BEM methods for calculation of realistic head models.

6.2.4 Sensors in Brainstorm

In order to obtain a forward model in Brainstorm, in addition to the source and head models and the head anatomy, a channel file needs to be imported to the software. This channel file should include the names and positions of the array of sensors (electrodes) that would be collecting the electrical/magnetic signals generated outside the head. These sensors usually come in standard cap forms which are used in clinics to record brain signals from patients.

Throughout this thesis a 151-channel CTF MEG cap is assumed to collect MEG signals. This MEG helmet comprises of 151 axial gradiometers and 29 reference channels used for noise cancellation. MEG helmets with 64 and 275 coils also exist in the market.

Figure 6.9 shows a schematic of the position of the 151 CTF helmet sensors around a head anatomy.

For EEG signals, a GSN 128 EEG cap is assumed to record electric potentials on the scalp. Other standard EEG electrode systems include the famous 10-10 and 10-20 configurations, and other EEG caps that include 32, 64, or 256 electrodes. Figure 6.10 shows a schematic of GSN 128 electrodes encompassing Colin's head anatomy.

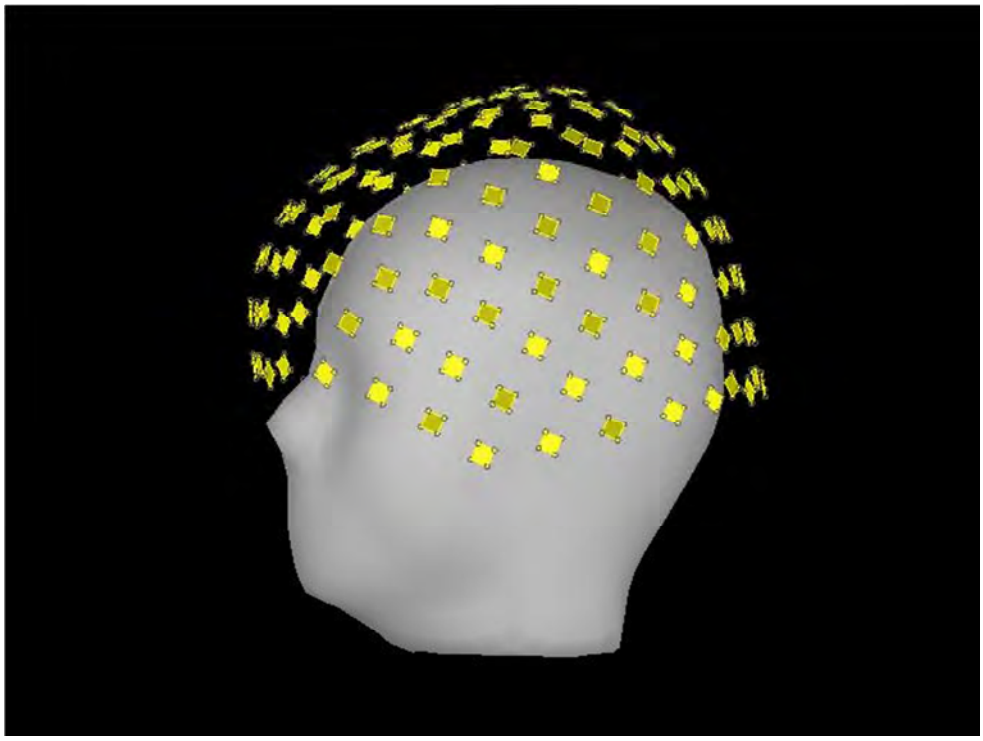

Figure 6.9: Schematic of the position of the 151 CTF MEG helmet sensors around Colin head anatomy (developed in Brainstorm)

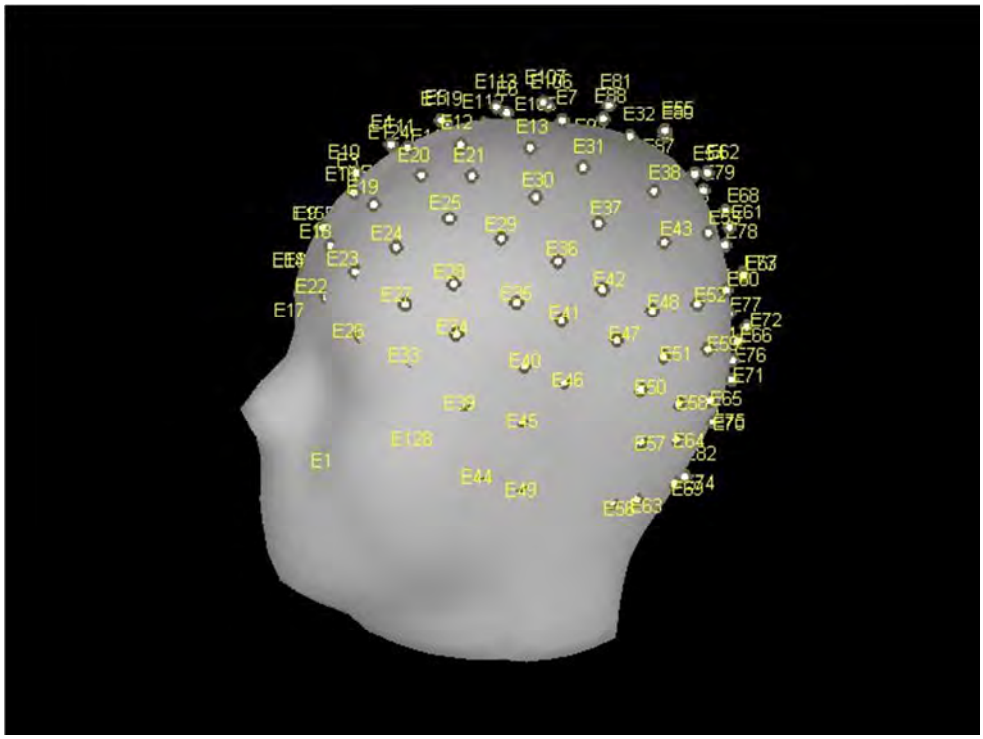

Figure 6.10: Schematic of the position of EEG GSN 128 electrodes around Colin anatomy (developed in Brainstorm)

6.3 Assumptions

The head models developed in this research are either spherical or realistic. The realistic heads are derived from boundary element method (BEM), using OpenMEEG software [41]. The common assumption in all these head models is that each of the layers of the head (cortex, skull, and scalp) is isotropic and homogeneous. This is a simplifying assumption used in many researches of this field. In reality, however, none of the abovementioned layers is neither isotropic, nor homogeneous. In order to get a more realistic head model, one has to use softwares that produce BEM realistic head models.

But in order to generate a forward solution, even simpler head models such as spherical and BEM realistic require that the conductivities of the head layers be provided to the software. What is more important than the absolute conductivity values of brain surfaces is the ratio of their corresponding conductivities due to the role it plays at the boundaries.

Among conductivities of brain, skull and scalp, the skull conductivity is the most crucial parameter in development of the head model. However, different studies suggest different values for this parameter, relative to conductivities of brain and scalp. The oldest, most often used conductivity ratio for brain, skull and scalp is 1:1/80:1 [45]-[48]. However, other studies suggest that the correct ratio is in the vicinity of 1:1/15:1 [49]-[52]. Other studies have found different values or ranges for conductivity ratio between the two abovementioned extremes [53]-[55]. In this research, the baseline for conductivity ratio of brain: skull: scalp is the default values in Brainstorm software, which is 1:1/80:1 ratio; this ratio corresponds to absolute conductivity values of 0.33 S/m: 0.0042 S/m: 0.33 S/m. The baseline for skull thickness is set to 4 millimeters.

Another crucial assumption in the course of this research is the orientation of the current dipoles. In both forward and inverse solutions obtained in this work the orientation of the current dipoles is assumed to be normal to the local cortex surface. This is a widely used assumption in the literature, which is physiologically justified, since pyramidal neurons that constitute 80% of the neocortical neurons are organized normal to the local cortex surface [56] [57].

6.4 Generation of Synthetic Brain Signals

Once a solution to the forward problem is generated using the dedicated software (BrainStorm/OpenMEEG), one obtains a *leadfield matrix S* that shows the signal collected at each MEG/EEG sensor as a result of brain activity at each one of the source locations. Matrix S is also called the *array manifold*. This is an $N \times M$ matrix, where N is the number of sensors (array elements), and M is the number of sources (dipoles). Each column of the manifold is called a *steering vector,* which basically corresponds to signals collected at the N sensors, as a result of one single source activity.

In order to generate synthetic brain signals, a superposition assumption is adopted. In other words, it is assumed that brain signals recorded via an array of sensors around the head can be modeled as the superposition of independent contributions from a number of sources. When put into matrix form, this formulation summarizes to

$$\boldsymbol{y}(l) = \boldsymbol{S}\boldsymbol{x}(l) + \boldsymbol{v}(l) \qquad (6.1)$$

where $\boldsymbol{y}(l)$ is an $N \times 1$ vector of measurements from N sensors at time l; $\boldsymbol{S}$ is the $N \times M$ lead-field matrix obtained from forward problem solution; $\boldsymbol{x}(l)$ is an $M \times 1$ vector representing amplitudes of M sources at time l; and $\boldsymbol{v}(l)$ is an $N \times 1$ vector of zero-mean additive Gaussian noise values at time l. As mentioned before, usually $M \gg N$; i.e. the number of possible source locations far exceeds the number of array elements.

The signal shape $\boldsymbol{x}$ used in this research, which is assigned to selected active source locations, is either sinusoid or Gaussian; this is due to the similarity of these waveforms to the action potential actually produced by brain neurons. The signal amplitude (dipole moment) is set to tens of nanoAmp.meters, which is a physiologically plausible assumption. Noise is assumed to be white Guassian, and the variance of noise is adjusted to obtain various signal to noise ratios (SNR). The number of array elements is the number of sensors used in MEG/EEG cap, which is in the range of a few hundred elements. The number of data samples (snapshots) generated and used in inverse solution is only a few (less than ten).

Once these synthetic signals are generated, they are used to localize active sources using the method described in the following section.

6.5 The SAFFIRE Algorithm

The principles of phased array signal processing and a few direction of arrival (DOA) techniques were presented in Chapter 5 of this report. The problem of DOA estimation can be summarized as follows: the superposition of a set of signals arrives at a collection of antenna elements; the goal is to determine the individual spatial arrival angles (relative to some reference). But sometimes the signals coming from different locations arrive at a set of antenna (array) elements with very small spatial separation, which makes it impossible to resolve them by the nominal array resolution. Hence, higher resolution DOA techniques have been developed to make the above possible [4].

In the previous chapter, MUSIC was introduced as one of these high resolution techniques. In this chapter, another high resolution DOA estimation method is introduced, which forms the basis for the simulations of this research. This technique has many advantages many other methods in its category. For example, MUSIC requires the

formation of a sample covariance matrix (SCM) from a collection of spatial snapshots. This SCM has to be decomposed to its eigen-values and eigen-vectors. Next, assuming that the signal and noise subspace are orthogonal, and the number of sources is known apriori, MUSIC offers high resolution DOA estimation. Some of the challenges faced in SCM-based techniques are as follows [4]:

(1) When DOAs of the sources change very fast with time, the number of available data samples (sample support) decreases. . Hence, the estimated SCM in this case is less accurate, which in turn degrades the performance of the corresponding SCM-based method;
(2) Most SCM-based techniques require eigen-decomposition of the SCM;
(3) SCM-based techniques don't perform well when there is temporal correlation between sources; because temporal correlation results in fewer available independent snapshots (smaller sample support);
(4) The number of underlying sources (model order) has to be known or estimated apriori for most of the methods in SCM-based category;
(5) These techniques are very sensitive to array modeling errors;
(6) They usually don't provide any information about the amplitude of the localized source.

In this chapter, a very high resolution DOA technique is introduced that can deal with all the abovementioned challenges. The re-iterative super-resolution (RISR) algorithm is based on a recursive implementation of minimum mean-square error (MMSE) estimation. The advantages of this technique are as follows [4]:

(1) It requires very small sample support,
(2) It does not require an SCM, nor its eigen-decomposition.; instead, it deploys non-coherent integration of multiple snapshots,
(3) It offers good robustness against temporal correlation,
(4) It determines the model order (number of sources) automatically,
(5) With an approximate knowledge of the array calibration tolerance, it can account for array modeling errors.

(6) Noise information is included in the estimator, given that the noise power is provided.

The adaptation of RISR to the application of neuro-imaging is called the Source Affine Image Reconstruction (SAFFIRE) algorithm. The main structure of SAFFIRE is explained in section 6.5.1. Additional modifications are discussed in the following sections of this chapter.

6.5.1 Source Affine Image Reconstruction (SAFFIRE) algorithm

SAFFIRE, like many functional brain imaging methods, is based on the assumption that brain signals recorded via an array of sensors around the head, can be modeled as the superposition of independent contributions from a number of sources, assumed to be distributed over a grid throughout the brain. Hence,

$$\boldsymbol{y}(l) = \boldsymbol{S}\boldsymbol{x}(l) + \boldsymbol{v}(l) \qquad (6.2)$$

where $\boldsymbol{y}(l)$ is an $N \times 1$ vector of measurements from N sensors at time l; $\boldsymbol{S}$ is the normalized $N \times M$ lead-field matrix obtained from forward problem solution; $\boldsymbol{x}(l)$ is an $M \times 1$ vector representing amplitudes of M sources at time l; and $\boldsymbol{v}(l)$ is an $N \times 1$ vector of zero-mean additive Gaussian noise values at time l. Usually $M \gg N$.

The sources are usually modeled as current dipoles, which can have strength components (amplitudes) in x, y, z directions (or ρ, ϕ, θ in spherical coordinates). Hence, originally $\boldsymbol{x}(l)$ is a $3M \times 1$ vector, and similarly $\boldsymbol{S}$ can generally be an $N \times 3M$ lead-field matrix. SAFFIRE is capable of finding all 3 strength components for each dipole. However, the assumption in this research work is that current sources are aligned normal to the local cortex surface. This assumption is physiologically justifiable, since pyramidal neurons that constitute 80% of cortex neurons are organized normal to the local cortex surface. Hence, the source matrix $\boldsymbol{x}(l)$ is modeled as an $M \times 1$ vector, and the corresponding lead-field matrix,$\boldsymbol{S}$, is of size $N \times M$.

Next, SAFFIRE searches for the $N \times M$ adaptive filter bank that minimizes the mean square error (MSE) cost function

$$\boldsymbol{J} = E\left\{\left|\left|\boldsymbol{x}(l) - \hat{\boldsymbol{x}}(l)\right|\right|^2\right\} = E\left\{\left|\left|\boldsymbol{x}(l) - \boldsymbol{W}^T(l)\boldsymbol{y}(l)\right|\right|^2\right\} \qquad (6.3)$$

where $E\{.\}$ denotes expectation and $(.)^T$ is transposition and $\hat{\boldsymbol{x}}(l)$ is the minimum mean square error (MMSE) estimate of $\boldsymbol{x}(l)$.

To find the filter $\boldsymbol{W}(l)$ that satisfies the MMSE criterion, the derivative of $\boldsymbol{J}$ with respect to $\boldsymbol{W}(l)$ is set to zero, which yields:

$$E\{2\,\boldsymbol{y}^T(l)[\boldsymbol{x}(l) - \boldsymbol{W}^T(l)\boldsymbol{y}(l)]\} = 0 \tag{6.4}$$

hence,

$$\boldsymbol{W}(l)E\{\boldsymbol{y}(l)\boldsymbol{y}^T(l)\} = E\{\boldsymbol{y}(l)\,\boldsymbol{x}^T(l)\} \tag{6.5}$$

which results in:

$$\boldsymbol{W}(l) = (E\{\boldsymbol{y}(l)\,\boldsymbol{y}^T(l)\})^{-1}\,E\{\boldsymbol{y}(l)\,\boldsymbol{x}^T(l)\} \tag{6.6}$$

Substituting (6.2) into (6.6) and assuming no correlation between source signal and noise, MMSE filter bank is derived to be [4]:

$$\begin{aligned}\boldsymbol{W}(l) = (&\boldsymbol{S}E\{\boldsymbol{x}(l)\boldsymbol{x}^T(l)\}\boldsymbol{S}^T \\ &+\ E\{\boldsymbol{v}(l)\boldsymbol{v}^T(l)\})^{-1}\,\boldsymbol{S}E\{\boldsymbol{x}(l)\boldsymbol{x}^T(l)\}\end{aligned} \tag{6.7}$$

The spatial power distribution of the source is denoted as $\boldsymbol{P}(l) = E\{\boldsymbol{x}(l)\boldsymbol{x}^T(l)\} \odot \mathbf{I}_{\mathrm{M\times M}}$, and the noise correlation matrix as $\boldsymbol{R}_v = E\{\boldsymbol{v}(l)\boldsymbol{v}^T(l)\}$. In practice, the noise covariance matrix information can be obtained from periods of time with no evoked response. Hence, equation (6.7) can be presented as:

$$\boldsymbol{W}(l) = (\boldsymbol{S}\boldsymbol{P}(l)\boldsymbol{S}^{\boldsymbol{T}} + \boldsymbol{R}_v)^{-1}\,\boldsymbol{S}\boldsymbol{P}(l) \tag{6.8}$$

Since prior knowledge of $\boldsymbol{P}(l)$ is generally not available, one needs to reiterate upon a previous estimate of the spatial power distribution. For initialization of the algorithm, SAFFIRE uses a matched filter (MF) to get the initial spatial power distribution. There is an extensive discussion in [5] about the choice of the initialization method and how initialization effects propagate through the iterations of SAFFIRE. Matched filter is a low resolution technique that turns out to result in the lowest localization error, hence adopted in this case [5]:

$$\hat{\boldsymbol{x}}_0(l) = \boldsymbol{S}^T \boldsymbol{y}(l) \tag{6.9}$$

Which results in the initial estimate of the spatial power distribution to be:

$$\hat{\boldsymbol{P}}_0(l) = [\hat{\boldsymbol{x}}_0(l)\, \hat{\boldsymbol{x}}_0^T(l)] \odot \mathbf{I}_{\mathrm{M}\times\mathrm{M}} \tag{6.10}$$

where $\odot$ is the Hadamard (element by element) product, and $\boldsymbol{I}$ is the identity matrix, to enforce the assumption that the sources are temporally uncorrelated. This assumption is justified by the fact that even if there is any temporal correlation between the sources, it is generally unknown beforehand. Moreover, this algorithm works on each snapshot independently or at best combines power estimates via noncoherent integration; hence, the temporal correlation of sources is not an issue as far as the algorithm is concerned. Note that, even though this algorithm is robust to source correlation, still having coherent sources is similar to a severe reduction in sample support scenario, which degrades the performance to some extent [4]:

Once the algorithm has been initialized, for subsequent steps the previous power estimate $\boldsymbol{P}_{i-1}(l)$ is used to obtain the new MMSE filter estimate as follows:

$$\widehat{\boldsymbol{W}}_{\boldsymbol{i}}(l) = \left(\boldsymbol{S}\widehat{\boldsymbol{P}}_{\boldsymbol{i-1}}(l)\boldsymbol{S}^{\boldsymbol{T}} + \boldsymbol{R}_v\right)^{-1} \boldsymbol{S}\widehat{\boldsymbol{P}}_{\boldsymbol{i-1}}(l) \tag{6.11}$$

This filter is then applied to the available data to obtain a new estimate of the source power distribution:

$$\hat{\boldsymbol{x}}_i(l) = \widehat{\boldsymbol{W}}_i^T(l)\, \boldsymbol{y}(l) \tag{6.12}$$

Hence, the ith power spatial distrubution estimate can be computed as:

$$\hat{\boldsymbol{P}}_i(l) = [\hat{\boldsymbol{x}}_i(l)\, \hat{\boldsymbol{x}}_i^T(l)] \odot \mathbf{I}_{\mathrm{M}\times\mathrm{M}} \tag{6.13}$$

Equations (6.11)-(6.13) form the ith recursive stage of the basic form of RISR/SAFFIRE. The recursions can be stopped when the norm of the difference between two consecutive source estimates falls below a predetermined small value, or as the number of iterations reaches a predetermined value. It has been reported in [4] and also

observed in the course of simulations of this research, that RISR/SAFFIRE appears to reach steady state within maximum of 15 iterations.

Once recursion stops, the "RISR/SAFFIRE spectrum" can be determined from diagonal elements of the diagonal matrix $\sqrt{\boldsymbol{P}_i(l)}$, and the corresponding spectrum amplitudes provide an estimate of the spatial magnitude distribution of the sources. Subsequent sections of this chapter demonstrate modifications to improve the performance of this algorithm.

6.5.2 Non-coherent Integration

RISR/SAFFIRE can operate on a single snapshot of data; however, for L time samples of recordings a *non-coherent integration* scheme can be adopted to improve performance. Assume that a collection of L spatial snapshots have been received

$$\boldsymbol{Y} = [\,\boldsymbol{y}(l) \;\; \boldsymbol{y}(L+1) \;\; \ldots \boldsymbol{y}(l+L-1)] \tag{6.14}$$

And it is desired to form an aggeragte filter bank $\overline{\boldsymbol{W}}$ in order to estimate L spatial amplitude estimate for the M sources, as follows:

$$\widehat{\boldsymbol{X}} = \overline{\boldsymbol{W}}^T \boldsymbol{Y} \tag{6.15}$$

Where $\widehat{\boldsymbol{X}} = [\widehat{\boldsymbol{x}}(l) \;\; \widehat{\boldsymbol{x}}(L+1) \;\; \widehat{\boldsymbol{x}}(l+L-1)]$ is an $M \times L$ martix. The spatial power distribution $\boldsymbol{P}$ is assumed to be stationary in the time period containing the L snapshots; hence $\boldsymbol{P}$ can be derived from the non-coherent integration of L time samples as follows

$$\overline{\boldsymbol{P}} = [\left(\frac{1}{L}\right) \sum_{\tau=0}^{L-1} \widehat{\boldsymbol{x}}(l+\tau)\, \widehat{\boldsymbol{x}}^T(l+\tau)] \odot \boldsymbol{I}_{M*M} \tag{6.16}$$

where $\odot$ is the Hadamard (element by element) product, and $\boldsymbol{I}$ is the identity matrix.
For each iteration, this average power estimate $\overline{\boldsymbol{P}}_{i-1}$ is used instead of the single snapshot power estimate $\widehat{\boldsymbol{P}}_{i-1}(l)$ to yield an estimate of the aggregate MMSE filter bank $\overline{\boldsymbol{W}}_{\boldsymbol{i}}$. Again for initialization of the algorithm a matched filter bank is applied to L snapshots of data, to give initial source distribution estimates for L time samples.

Once the algorithm converges to a stable solution or after a certain number of iterations, the final average amplitude distribution is obtained from the diagonal elements of the average spatial power distribution.

$$\bar{\boldsymbol{X}} = diag(\sqrt{\bar{\boldsymbol{P}}}) \tag{6.17}$$

The number of sources (model order), and their locations and amplitudes are estimated via the peaks in $\bar{\boldsymbol{X}}$. Hence, this algorithm is robust to correlation between sources, requires low sample support, determines the model order intrinsically and can be extended to account for array modeling error, as explained later on in this chapter.

The following flow-chart explains the basic structure of RISR/SAFFIRE explained so far in this chapter:

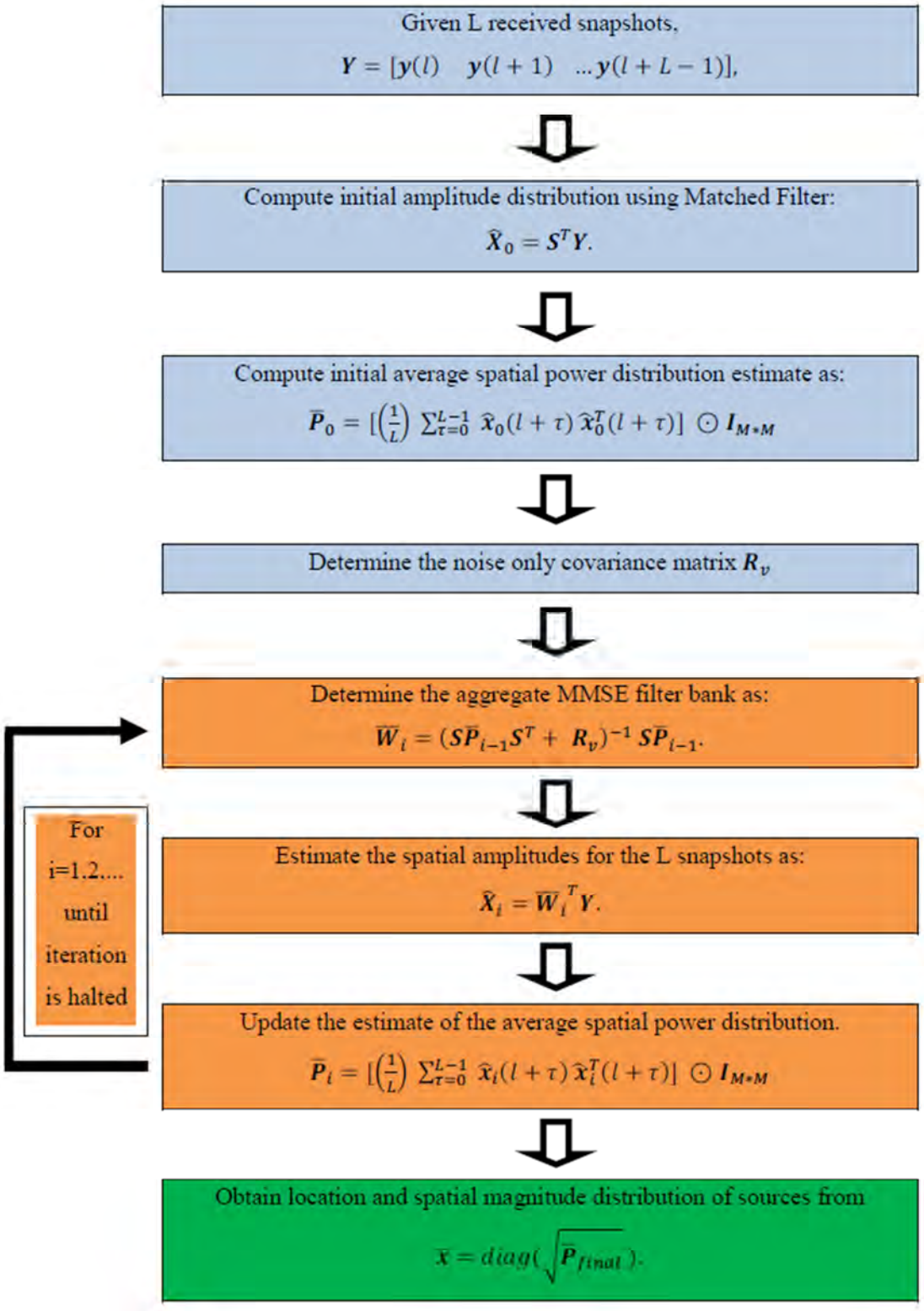

Figure 6.11: Flow-chart depicting the iterative stages of the SAFFIRE algorithm

6.5.3 Affine Transform of Solution Space

Superficial sources on the cortex are located closer to MEG/EEG array of sensors; hence, their corresponding *steering vectors* (defined as columns of the *lead-field* matrix $\boldsymbol{S}$) have larger norms relative to deeper sources. This causes a bias towards superficial sources in some localization methods, such as minimum norm estimate (MNE) technique. Various weighted MNE methods have been proposed to make up for this bias [58]. In a similar manner, SAFFIRE is adjusted to give all sources equal chance in the localization process; this adjustment is done through normalization of columns of the lead-field matrix $\boldsymbol{S}$ [5].

6.5.4 Energy Normalization

SAFFIRE starts by a matched filter initialization, which is a low resolution technique, and spreads the signal energy over most of the solution space. Later on, this initial distribution of sources is refined through the iterative steps of SAFFIRE. However, the recursions can introduce some scaling factor when the filter bank is being estimated, which can alter the ratio of signal to noise power. To compensate for this scaling effect, SAFFIRE uses energy normalization at each iteration to ensure that if dipole component estimate inserted into the forward model (exclusive of noise), it would produce a received signal estimate that has the same energy as the actual received signal [5].

6.5.5 Accounting for Modeling Errors

In all the above sections, exact knowledge of the lead-field matrix has been assumed. In reality, however, direction finding methods usually face forward problem uncertainties. Small errors arise from approximation of the volume conductor, discretization of the source space, co-registration with limited accuracy, small displacement of array elements (sensors), etc. These errors cause perturbations (in the lead field matrix) known as calibration errors.

To account for modeling errors, SAFFIRE represents the effect of modeling errors on the nth sensor as :

$$z_n = 1 + \Delta z_n \tag{6.18}$$

where Δz_n is a random amplitude deviation of arbitrary distribution. By putting all z_n elements together, an $N \times 1$ vector $\boldsymbol{z}$ is formed, and incorporated in equation (1) as follows [5]:

$$\boldsymbol{y}(l) = \big(\boldsymbol{S}\boldsymbol{x}(l)\big) \odot \boldsymbol{z} + \boldsymbol{v}(l) \approx \boldsymbol{S}\boldsymbol{x}(l) + \boldsymbol{v}(l) + \boldsymbol{v_z}(l) \tag{6.19}$$

where $\boldsymbol{v_z}(l) = (\boldsymbol{S}\boldsymbol{x}(l)) \odot (\boldsymbol{z} - \boldsymbol{1}_{N\times 1})$ is the noise caused by model errors. Assuming that all modeling errors are zero mean, symmetric, independent and identically distributed, and also assuming that source signals and additive noises are independent, the filter bank at iteration i can be rewritten as [5]:

$$\widehat{\boldsymbol{W}}_{\boldsymbol{i}}(l) = \big(\boldsymbol{S}\widehat{\boldsymbol{P}}_{\boldsymbol{i-1}}(l)\boldsymbol{S}^T + \boldsymbol{R}_v + \boldsymbol{R}_z\big)^{-1}\, \boldsymbol{S}\widehat{\boldsymbol{P}}_{\boldsymbol{i-1}}(l) \tag{6.20}$$

where $\boldsymbol{R}_z = E\{\boldsymbol{v}_z(l)\boldsymbol{v}_z^T(l)\}$ is the "model noise" covariance matrix, which is a signal-dependent term that adapts according to the update of the source estimate. On the other hand, the noise covariance term $\boldsymbol{R}_v$ is a fixed-regularization term [4]. Substituting the presumed model noise into $\boldsymbol{R}_z = E\{\boldsymbol{v}_z(l)\boldsymbol{v}_z^T(l)\}$ yields:

$$\begin{aligned} \boldsymbol{R}_z &= E\Big\{\ (\boldsymbol{z} - \boldsymbol{1}_{N\times 1}) \odot \big(\boldsymbol{S}\boldsymbol{x}(l)\big)\big(\boldsymbol{S}\boldsymbol{x}(l)\big)^T \odot\ (\boldsymbol{z} - \boldsymbol{1}_{N\times 1})^T\Big\} \\ &= E\{\widetilde{\boldsymbol{Z}}\,\big(\boldsymbol{S}\boldsymbol{x}(l)\big)\big(\boldsymbol{S}\boldsymbol{x}(l)\big)^T\widetilde{\boldsymbol{Z}}^{\,T}\} \end{aligned} \tag{6.21}$$

where $\widetilde{\boldsymbol{Z}} = diag\{z_0, z_1, \ldots., z_{M-1}\} - I_{M\times M}$. Assuming that the modeling errors are uncorrelated and also assuming signal and modeling errors are independent, $\boldsymbol{R}_z$ simplifies to:

$$\boldsymbol{R}_z = \sigma_z^2 \boldsymbol{I}_{M\times M}\ \odot (\boldsymbol{S}\boldsymbol{P}(l)\boldsymbol{S}^T) \tag{6.22}$$

where $\odot$ is Hadamard product, and σ_z is model error variance. With the addition of this model error term $\boldsymbol{R}_z$, the aggregate filter bank update for L snapshots will evolve into:

$$\overline{\boldsymbol{W}}_i = (\boldsymbol{S}\overline{\boldsymbol{P}}_{i-1}\boldsymbol{S}^T + \sigma_z^2 \boldsymbol{I}_{M\times M}\ \odot (\boldsymbol{S}\overline{\boldsymbol{P}}_{i-1}\boldsymbol{S}^T) + \boldsymbol{R}_v)^{-1}\, \boldsymbol{S}\overline{\boldsymbol{P}}_{i-1} \tag{6.23}$$

6.5.6 How SAFFIRE works

In this section, the iterative technique of SAFFIRE is demonstrated through a series of simulations. In this set of simulations, the head anatomy used in solving the forward problem is Colin's anatomy; the head model utilized is single sphere head;

cortex surface is divided into 15,000 tessellations, each assumed to hold a current dipole. MEG CTF Helmet with 151 coils is assumed as the sensor array to collect MEG signals. Once the forward problem is solved with the abovementioned settings, synthetic MEG data is generated with the following assumptions: a single source is activated in the brain, where the source index is 992 (out of 15,000 source indices); the active source waveform is Gaussian with maximum amplitude of 15 nA.m, centered at 0.4ms with standard deviation of 8ms. The waveform is sampled at 1 KHz rate. Only 3 data samples are used in the SAFFIRE algorithm for localization purpose. Noise variance is adjusted to get SNR of -12 dB. This is a low SNR considering the typical SNR range studied in literature for this application (-15 to +20 dB).

Since most of the cortex surface has been mapped functionally over the years, depending on the type of stimulation, the approximate location of the evoked source can usually be determined a-priori.; for example, specific parts of the cortex correspond to auditory, visual and somatosensory responses. Hence, it's usually not necessary to include the whole cortex surface when solving the inverse problem. However, the following simulations are intended to show the extent of accuracy of SAFFIRE. Hence, a large portion of the cortex (one hemisphere) is included in iterations of SAFFIRE. Since the whole cortex has been divided to 15,000 grid points, one hemisphere is composed of 7,500 current dipoles. Moreover, the MEG Helmet used to record brain signal includes 151 axial gradiometers plus 29 reference electrodes, hence a total of 180 sensors. This leads to a system of equations with 180 equations and 7,500 unknowns. As expected, the system is highly underdetermined (ill-posed) as the number of unknowns (source amplitudes) is 42 times the number of equations (electrodes).

Figure 6.12 shows the low resolution matched filter initialization used to start the algorithm. Figure 6.13- Figure 6.16 show how SAFFIRE converges to the correct solution in a few iterations. Figure 6.17 is a zoomed in version of Figure 6.16 to show the index of the correctly localized source. Figure 6.18 shows the localized source mapped to cortex surface.

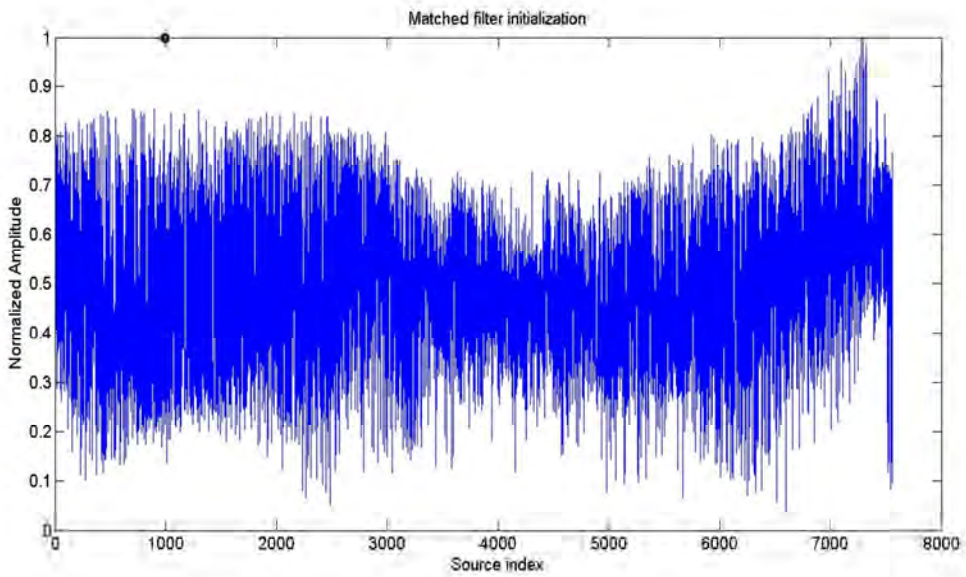

Figure 6.12: Matched-filter initialization of SAFFIRE applied to MEG data

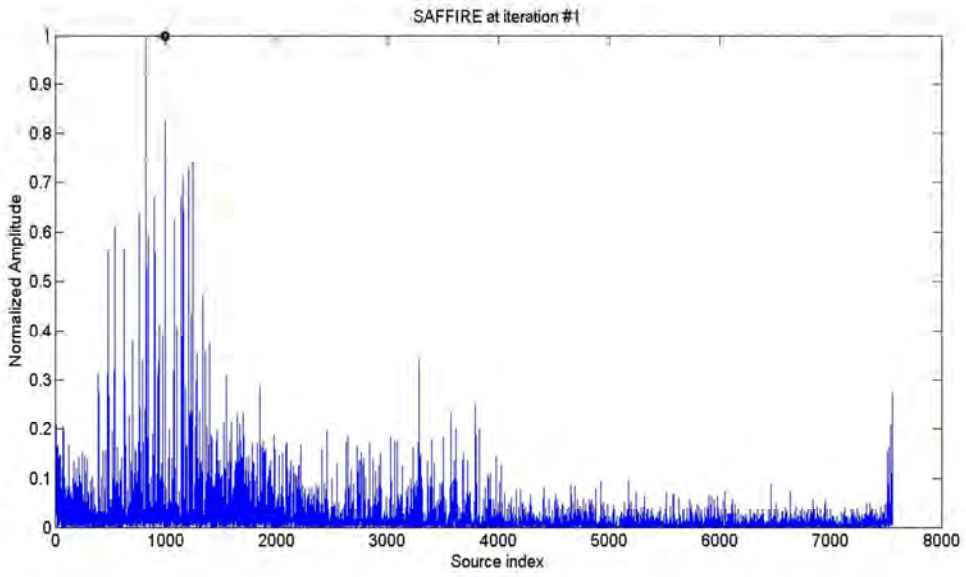

Figure 6.13: SAFFIRE applied to MEG data, iteration 1

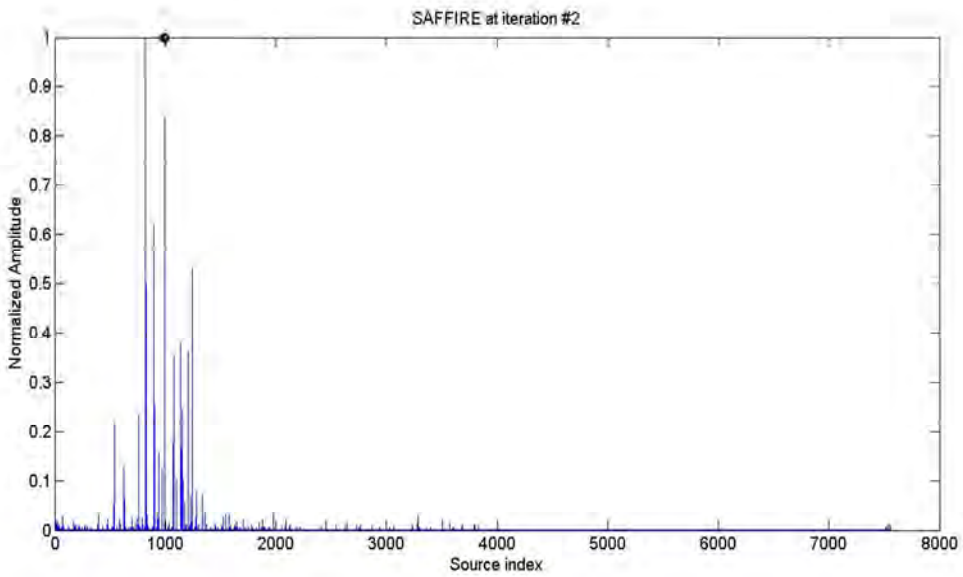

Figure 6.14: SAFFIRE applied to MEG data, iteration 2

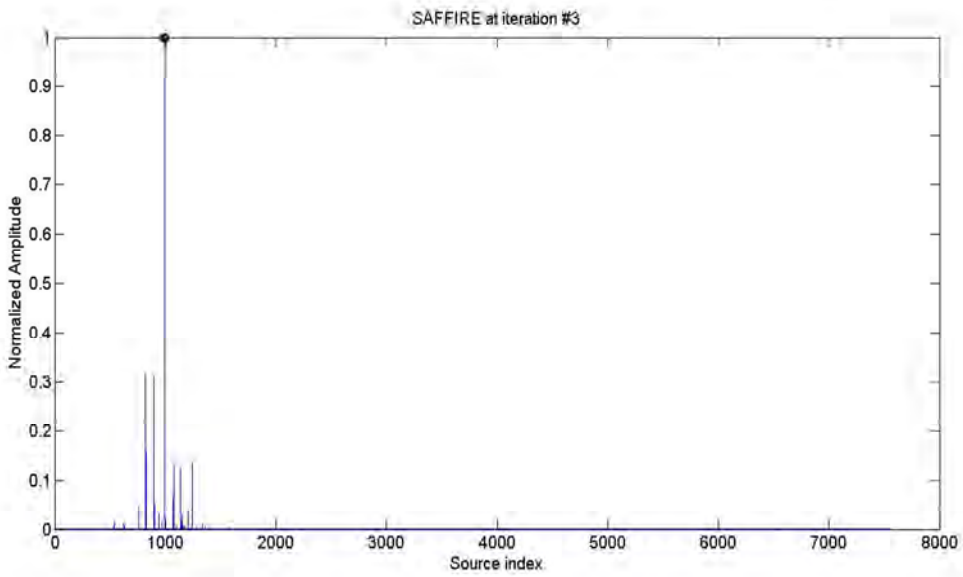

Figure 6.15: SAFFIRE applied to MEG data, iteration 3

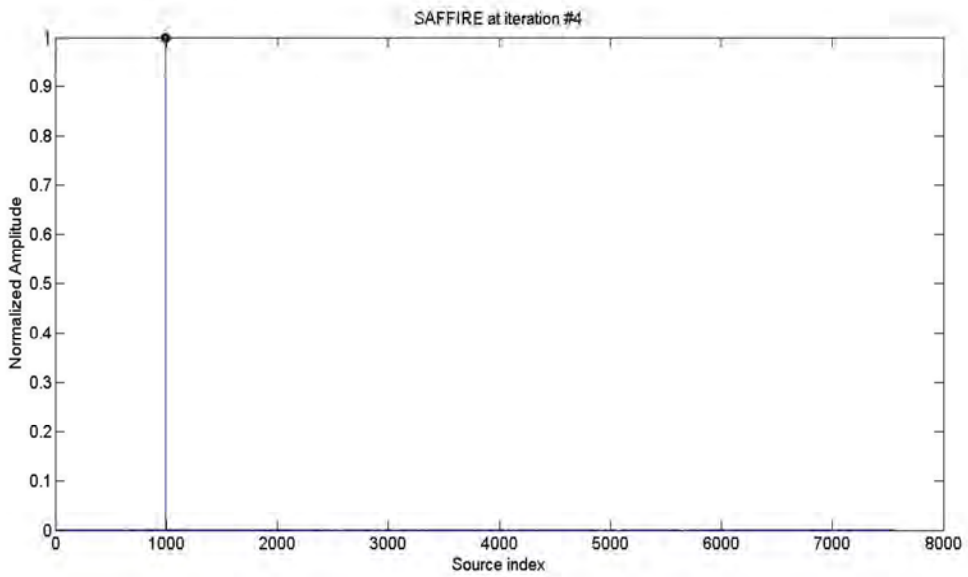

Figure 6.16: SAFFIRE applied to MEG data, iteration 4

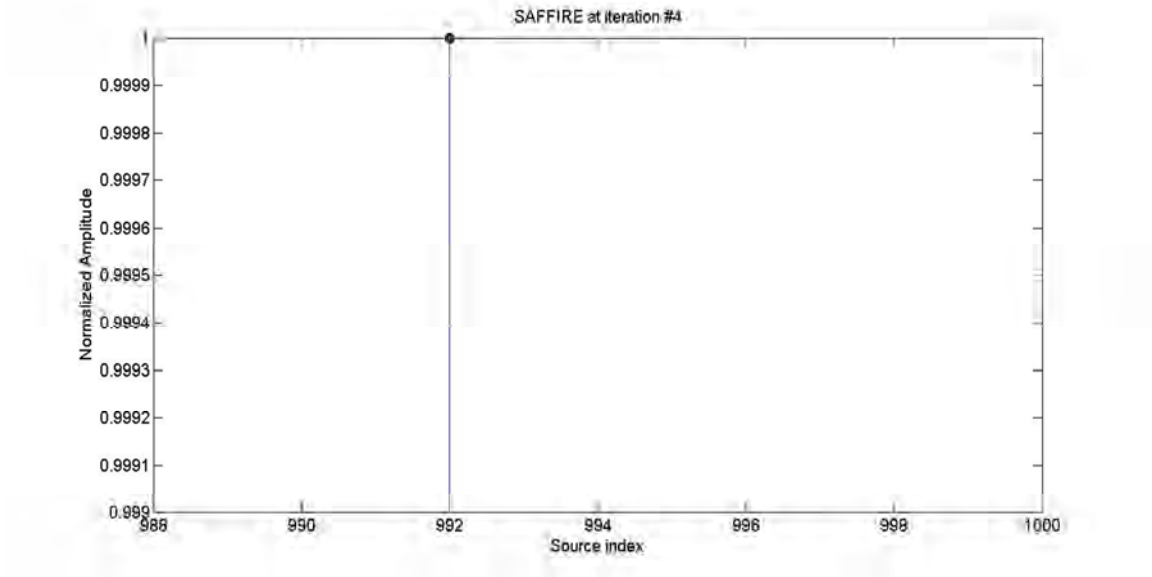

Figure 6.17: SAFFIRE applied to MEG data, iteration 4, zoomed in

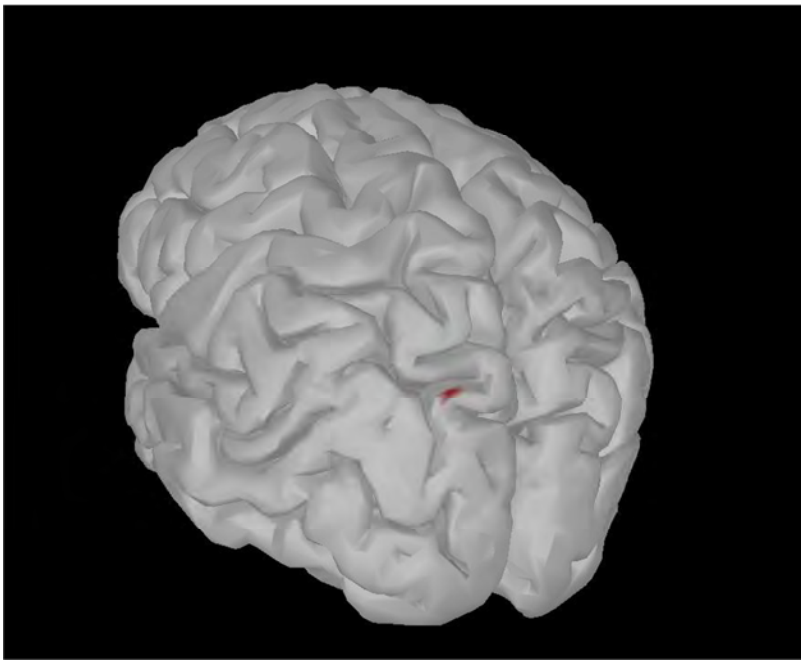

Figure 6.18: SAFFIRE localization result mapped to the cortex

6.6 Performance Metrics:

- Probability of detection: Once the iterations of SAFFIRE stop, a hard threshold is applied to the resulting spectrum. For example, with a threshold of 1%, only sources that contain more than 1% of the maximum recovered source power are considered. These sources are then compared against the 4 original activated sources and for each matching index a probability of detection of ¼ is credited to the localization. If there are more than 2 false peaks (recovered sources that had not been activated) in the spectrum, the localization is declared a failure, even if some of the actual sources were among the localized sources.
- Mean Square Error: MSE is computed as the average of the square error between the acquired spectrum and the correct spectrum, for hundreds of runs of SAFFIRE.

CHAPTER 7

BRAIN SOURCE LOCALIZATION FROM MEG SIGNALS

In this chapter, the performance of SAFFIRE is evaluated when applied to synthetically generated MEG data for different head models and anatomies. In order to show the high-resolution of this algorithm, 4 proximate sources are assumed to be active in the brain when generating the forward solution. The distance between any two of the active sources is a few millimeters (3-5mm).

The waveforms assigned to these sources are as follows: 2 sinusoids and 2 Gaussian waveforms. The sinusoids have maximum moment amplitude of 30 nA.m and frequency of 20 Hz; they are 90 degrees out of phase. The 2 Gaussians have respective maximum amplitudes of 15 and 7.5 nA.m; their means are located at a few milliseconds and their variances are 8 and 16ms. The 4 waveforms are shown in Figure 7.1 below in a time period of 100ms. Each waveform is sampled at a rate of 1 KHz. It is worth mentioning that the sources amplitudes, shapes and time delays have been inspired from real brain signals demonstrated in literature, obtained from signal decomposition methods such as independent component analysis (ICA).

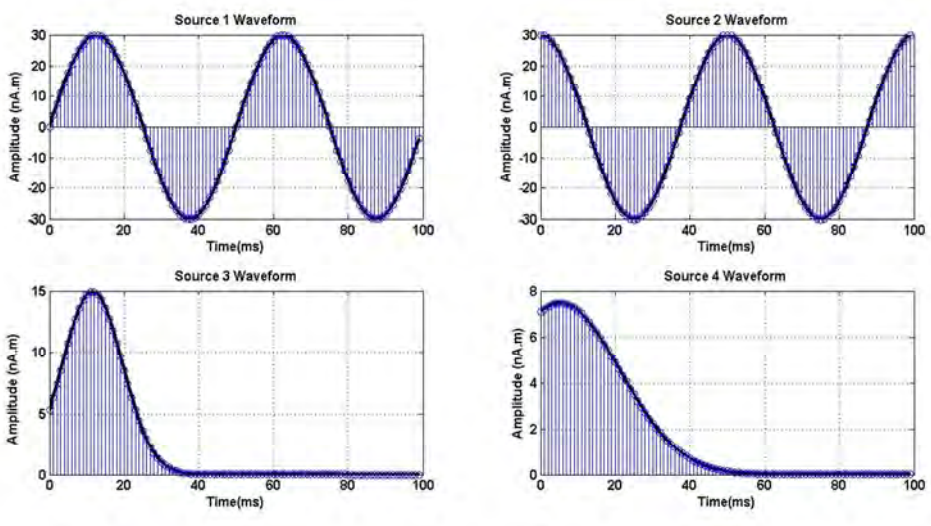

Figure 7.1: Waveforms assigned to the 4 proximate sources

Synthetic MEG signals are assumed to be recorded using a CTF 151 MEG helmet. At each of the MEG sensors, white Gaussian noise is added to the signal. The noise variance is changed in steps of a few dBs to obtain a range of SNR values from -30 to +30 dB. The reason for considering this SNR range is that SNR values considered for this application are typically between -15 and +20 dB as reported in the literature [59].

In practice, depending on the nature of the stimulation in an experiment (auditory, visual, somatosensory, etc), the approximate location of the evoked response can be determined apriori. Hence, throughout this report, a portion of the cortex (one fourth or one sixth) around the evoked brain source is included in the iterative search of SAFFIRE, instead of the whole cortex surface. This assumption greatly reduces the computational complexity, and can be accommodated in real cases.

SAFFIRE is applied iteratively to the scenario explained above, using the three possible head models developed for MEG application in turn; which are, in order of increasing accuracy: single sphere head model, overlapping spheres model, and realistic head model. All the above have been discussed in detail in Chapters 1 and 6 of this report. The same procedure is then applied to a second head anatomy, called hereafter "individual anatomy." The results for each part are presented in terms of the probability of detection of the 4 sources and the mean square error (MSE).

It should be noted that when applying SAFFIRE to each one of the mentioned head models, the inverse problem has been solved using the leadfield matrix produced in the forward solution using the same head model. In other words, it is implied that one has access to the exact array manifold in each case. This is an idealistic assumption and does not hold in many practical situations. When, in practice, the manifold used in the inverse problem is slightly different from the actual manifold of the data, it will result in errors in localization. These are called calibration errors, which will be discussed towards the end of this report.

7.1 Colin Anatomy

The first head anatomy investigated is the Colin anatomy [43]. The 4 selected sources have the following indices: 2000, 2030, 2148, and 2163, out of 3600 possible indices (locations). These selected sources are 3-5 mm apart from each other. Once

synthetic MEG data has been generated, 3 data samples are taken from each of the 180 channels. These 3 samples are then used in the SAFFIRE algorithm to recover the underlying sources. Figure 7.2 shows the result of iterations of SAFFIRE on 3 data samples, which has resulted in correct convergence to the desired source locations, within 7 iterations. The source amplitudes have been normalized, because at this stage the focus is on the location of the recovered sources. Later on in this report, recovery of sources amplitudes will be discussed.

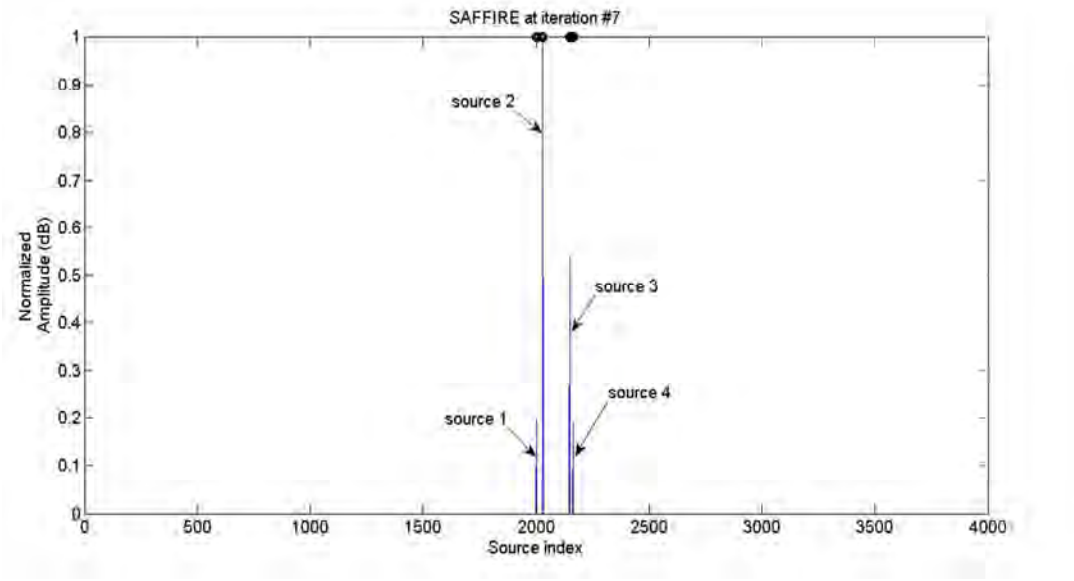

Figure 7.2: Result of applying SAFFIRE to 3 samples of MEG data, to find 4 sources

Figure 7.3 and Figure 7.4 summarize the performance of SAFFIRE on three types of head models developed for MEG application, on Colin anatomy. Figure 7.3 shows that the probability of detection of the sources is around 0.7 for all the head models, around SNR of -30 dB. As SNR increases, the detection probability remains rather constant until -10 dB. Between -10 and +10 dB this probability rises from 0.7 to 1.0, and it remains 1.0 for higher SNRs. The graph shows that when we have exact knowledge of the manifold for any of the investigated head models, SAFFIRE shows similar behavior on each head model in terms of the probability of detection of the 4 sources. In all three scenarios, SAFFIRE can accomplish exact recovery of the 4 sources for SNRs above +10dB.

Figure 7.4 demonstrates the MSE versus SNR, for the same experiment. As one can see, there is an inverse relationship between the probability of detection and the MSE

curve. MSE is initially around -3dB for SNR of -30 dB; between -3dB and +8 dB of SNR, MSE rolls off quickly from -4dB to –30 dB.

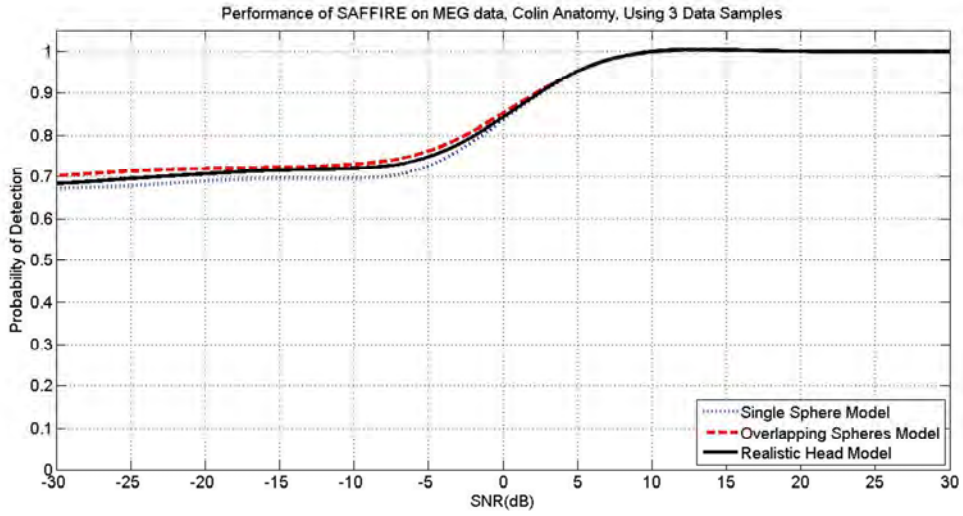

Figure 7.3: Probability of Detection of 4 proximate sources using SAFFIRE algorithm, from MEG data, on Colin anatomy, using 3 data samples

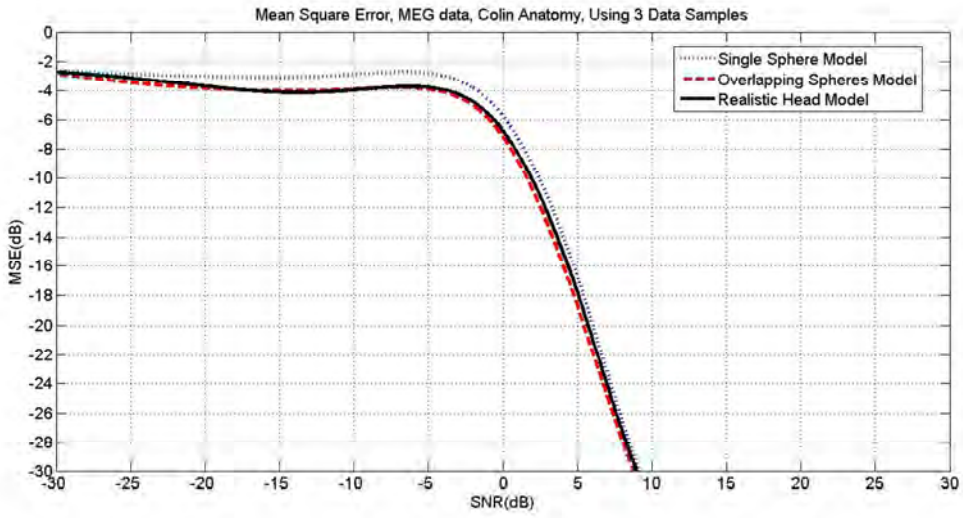

Figure 7.4: MSE for recovery of 4 proximate sources using SAFFIRE algorithm, from MEG data, on Colin anatomy, using 3 data samples

7.2 Individual Anatomy

An important factor in the investigations of brain signals is the effect of the physical shape of the head and the dielectric properties of the head surfaces on the acquired signals. Different people have very different head shapes; all layers of the head from the brain tissue to the inner and outer skull surfaces can vary significantly from one person to another. Among all layers, the most prominent difference is seen in the skull

shape, thickness, and conductivity in different individuals. Hence, any method or algorithm used to decompose or localize brain signals needs to consider these variations.

Of course, nowadays, most brain signal measurement techniques are used in conjunction with MRI, to get detailed information about the shape and thickness of the individual's head layers. This information can help one choose the right parameter values when forming a leadfield matrix to solve the inverse problem.

In this research, a second individual head is introduced in the simulations for comparison purposes with Colin head shape. The second anatomy is referred to as "individual anatomy" throughout this report, as opposed to Colin's anatomy. This individual anatomy has been obtained from the database of Brainstorm software website. It contains the scalp and cortex surfaces of an individual's head, which have been segmented using BrainVisa software. Since the information about the inner-skull and outer-skull surfaces are not available for this anatomy, once the two existing layers (scalp and cortex) are imported into BrainStorm software, a second procedure is performed. Using one of Braistorm's features, one can form pseudo layers for an anatomy, by interpolating the existing layers. This feature was utilized on the individual anatomy to obtain inner and outer skull surfaces, which are necessary for creating head models. The cortex of this individual anatomy is divided into 10,000 vertices.

Once the head models have been formed and forward solutions have been obtained for the individual anatomy, similar settings are applied for generation of synthetic brain signals. Again 4 proximate sources are picked and waveforms of known shape and amplitude are assigned to them. Approximately one sixth of the total cortex surface around the desired location is included in the iterative search of the SAFFIRE.

The goal is to see how SAFFIRE performs on this second anatomy when trying to localize the underlying neural activity. In order to be consistent, again 3 data samples are used for localization. Figure 7.5 and Figure 7.6 summarize the performance of SAFFIRE, in terms of probability of detection and MSE, on different head models produced for the same anatomy.

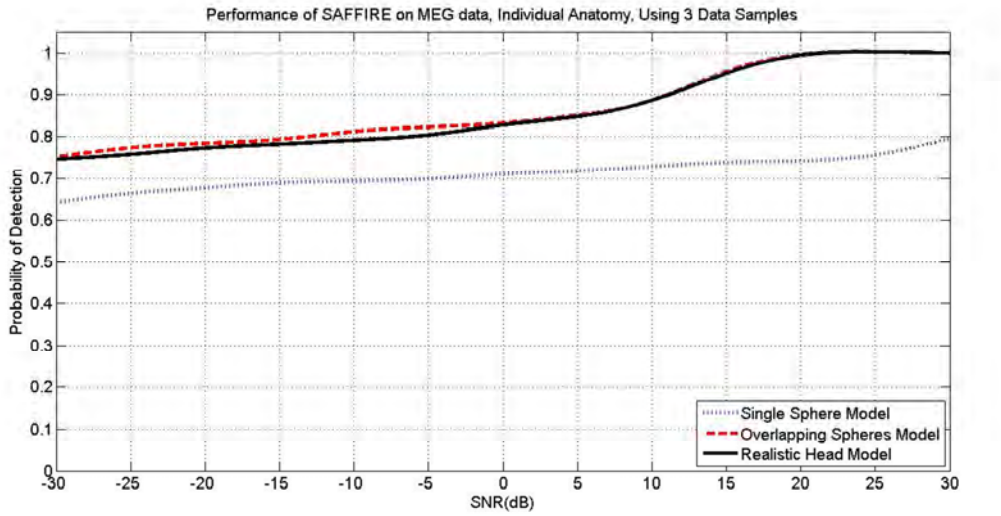

Figure 7.5: Probability of Detection of 4 proximate sources using SAFFIRE algorithm, from MEG data, on individual anatomy, using 3 data samples

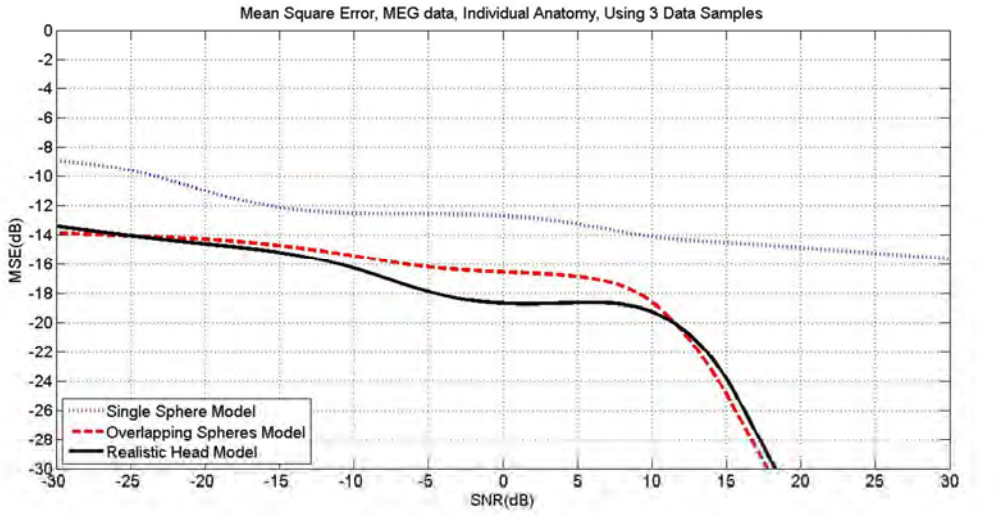

Figure 7.6: MSE for recovery of 4 proximate sources using SAFFIRE algorithm, from MEG data, on individual anatomy, using 3 data samples

Figure 7.5 suggests that the probability of detection of the 4 sources is about 0.75 for SNR as low as -30dB for overlapping spheres and realistic head models. This probability is lower for single sphere model by around 0.1. As SNR increases towards positive values, the detection rate increases gradually and reaches full detection for SNR around 20dB for overlapping and realistic head models. Single sphere model reaches maximum detection rate of about 80% for high SNR (+30 dB). Once this graph is compared with Figure 7.3 (for Colin anatomy), one realizes that even though the starting

detection is slightly higher for individual anatomy (at low SNRs), this second anatomy requires higher SNR for full recovery of the 4 sources. Colin offered exact localization of the sources for SNR around +10 dB, while individual anatomy requires at least +20 dB of SNR for similar performance.

Figure 7.6 shows the MSE for the same setup. For overlapping spheres and realistic head models MSE has a sharper fall for high SNRs. For these two head models, MSE reaches as low as -30 dB for SNR around +18 dB. However, the same MSE was accomplished on Colin's anatomy (Figure 7.4) for only +8 dB of SNR.

Figure 7.6 also suggests that the MSE corresponding to the single sphere head model is much higher compared to the other two head models. This is due to the fact that single sphere model of the individual anatomy did not result in full recovery of the 4 sources for any SNR in the designated range.

It should be noted that all the simulations so far have been carried out using only 3 data samples from the generated sequence of MEG recordings. But it was clear that the localization results on the single sphere head model of the individual anatomy were not satisfactory. Hence, in the next step, the number of data samples is increased to 5 for single sphere head model to see the effect on the performance of SAFFIRE. Figure 7.7 and Figure 7.8 demonstrate how the detection rate and MSE changes when the number of snapshots is increased from 3 to 5, for MEG data generated from a single sphere head model of the individual anatomy.

Figure 7.7 shows that the probability of detection of the 4 sources has improved by almost 0.15; hence, SAFFIRE can accomplish almost full recovery of the 4 sources using a single sphere head model for SNR of around +30 dB.

Figure 7.8 confirms the above finding; MSE starts at around -15 dB and reaches -30 dB for +26 dB of SNR. Even though these results from the single sphere model are still inferior to overlapping spheres and realistic models of the same anatomy (individual) and to all head models from Colin anatomy, one can see the improvement in the localization accuracy by adding only a few samples of recordings to the data used in the algorithm.

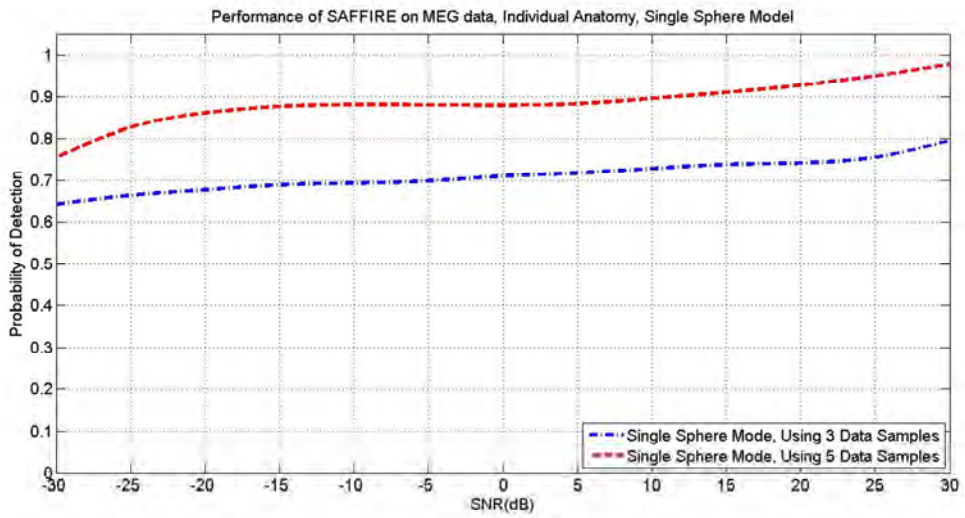

Figure 7.7: Probability of Detection of 4 proximate sources using SAFFIRE algorithm, from MEG data, on individual anatomy, for single sphere head model

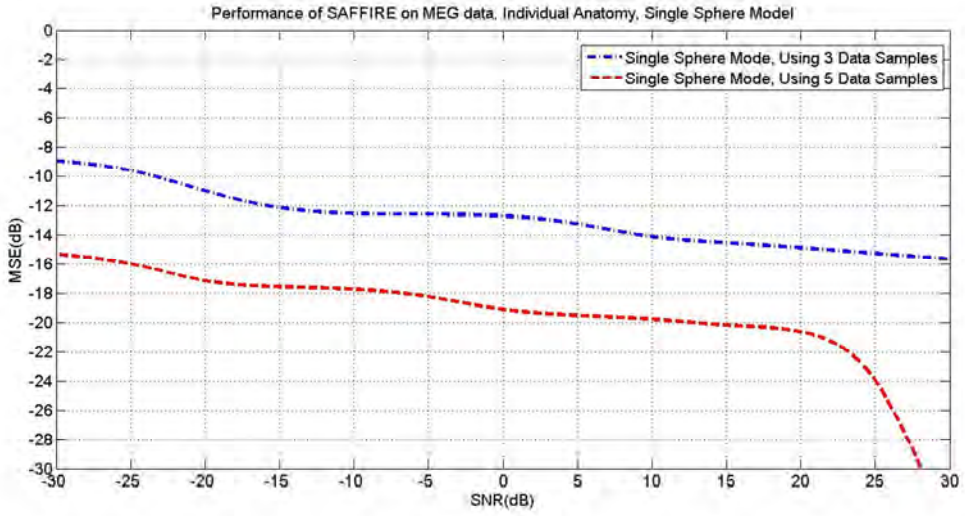

Figure 7.8: MSE for recovery of 4 proximate sources using SAFFIRE algorithm, from MEG data, on individual anatomy, for single sphere head model

By comparing the results for the two head anatomies and across all three head models, the following can be concluded:

(1) For Colin anatomy, all three head models show similar behavior in terms of detection rate and MSE, when used in SAFFIRE algorithm for localization, with only a few samples of data. For SNR about +8 dB, head models generated using Colin anatomy result in accurate localization of the 4 sources.

(2) Individual anatomy initially performs better in terms of probability of detection and MSE, for overlapping spheres and realistic head models, compared to the Colin's. However, as SNR increases, localization does not converge to the accurate scenario on individual anatomy as fast as it did in the case of Colin's. Overlapping and realistic head models require about +18 dB of SNR to reach their best performance.

(3) Single sphere head model seems to be the least reliable for the second anatomy. Only an increase in the number of samples could improve its performance. However, this increase was small (additional 2 samples) and it shows that with a few more snapshots of data, SAFFIRE can perform well on this kind of head model as well.

CHAPTER 8

BRAIN SOURCE LOCALIZATION FROM EEG SIGNALS

In this chapter, the performance of SAFFIRE is evaluated when applied to synthetically generated EEG data for different head models and anatomies. In order to show the high-resolution of SAFFIRE, 4 approximate sources are assumed to be active in the brain when generating the forward solution. The distance between the active sources is a few millimeters (3-5mm). The same points that were activated for MEG simulations have been considered for EEG experiment as well and the same waveforms have been assigned to them. That is, 2 sinusoids and 2 Gaussian waveforms. The sinusoids have maximum amplitude of 30 nA.m and frequency of 20 Hz; they are 90 degrees out of phase. The 2 Gaussians have respective maximum amplitudes of 15 and 7.5 nA.m; their means are located at a few milliseconds and their variances are 8 and 16ms. The 4 waveforms were formerly depicted in Figure 7.1 for a time period of 100ms. Each waveform is sampled at a rate of 1 KHz.

For each anatomy, two head models are developed: (1) three-shell head model, which consists of 3 concentric spheres representing scalp, skull and cortex, and (2) realistic head model, which is the model created based on symmetric boundary element methods (BEM) technique using OpenMEEG software. More details are available in the section 6.1 of this thesis.

Synthetic EEG signals are assumed to be recorded using a GSN 128 EEG cap, which as the name suggests, is composed of 128 EEG electrodes. A portion of the cortex (1/6-1/4) is included in the iterative search of SAFFIRE. Since the number of the EEG electrodes are fewer than the MEG scenario (which was 180), the resulting system of equations will be further underdetermined. As one will notice in the course of the simulations, this affects the localization results in some cases.

8.1 Colin Anatomy

In this section, the performance of SAFFIRE is evaluated on Colin's anatomy, for both possible head models, namely the three-shell and the BEM realistic head model.

Figure 8.1 reflects the probability of detection of the 4 close sources versus SNR, for both head models. Only 3 data samples have been utilized for localization. As the graph suggests, detection is around 0.6 for SNR in the range of -30 dB to -5 dB. Thereafter, detection probability rises gradually, and for SNR about +15dB the probability of detection reaches its maximum, i.e. full recovery of the 4 sources. The two head models demonstrate similar behavior, but three-shell model seems to perform slightly better in terms of probability of detection.

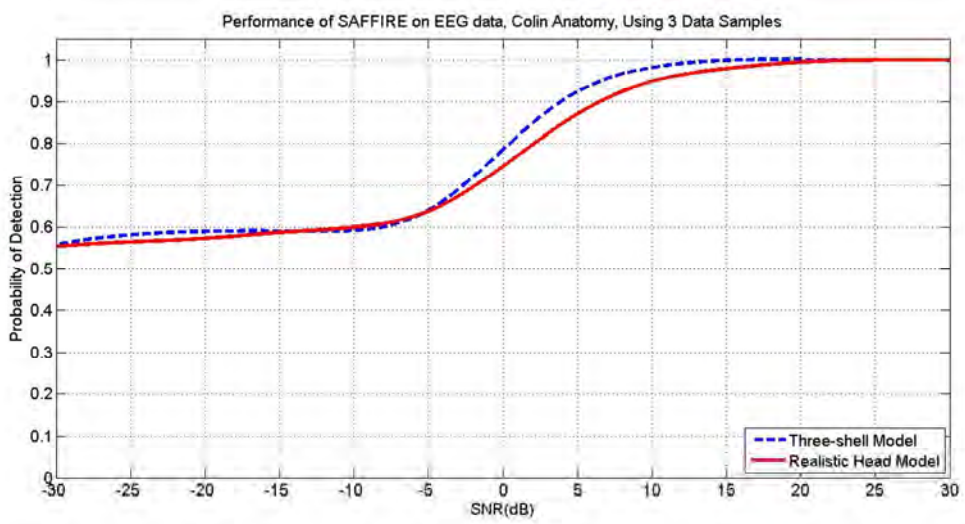

Figure 8.1: Probability of Detection of 4 proximate sources using SAFFIRE algorithm, from EEG data, on Colin anatomy, using 3 data samples

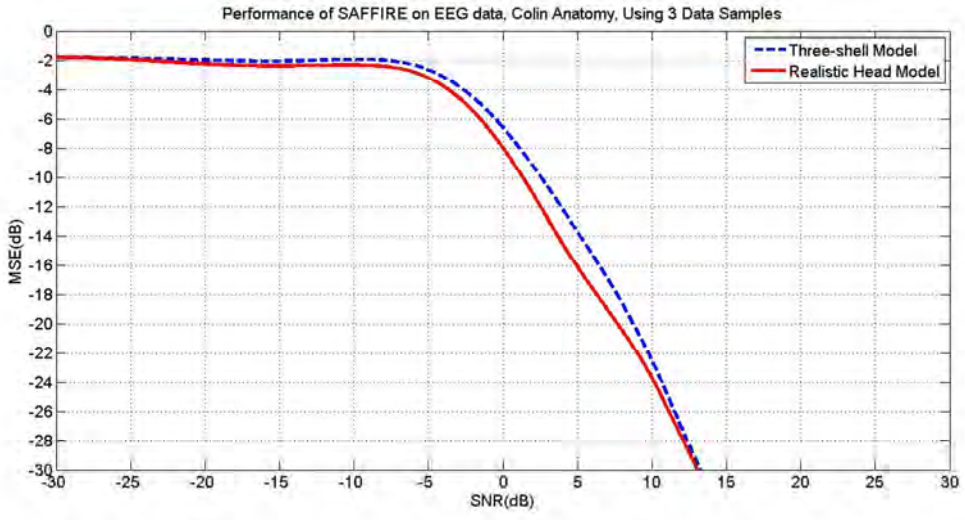

Figure 8.2: MSE for recovery of 4 proximate sources using SAFFIRE algorithm, from EEG data, on Colin anatomy, using 3 data samples

Figure 8.2 demonstrates the MSE for the same simulation setup. MSE is just above -2 dB for SNR of -30 dB and decreases very little as SNR increases to -5dB. Above -5 dB of SNR, MSE rolls off quickly and reaches -30 dB for +13 dB of SNR. Both head models present similar behavior, but realistic model performs slightly better for SNR between -3dB and +10 dB, in terms of mean square error.

8.2 Individual Anatomy

In order to see the effect of the head shape on the localization performance, a second anatomy is investigated using the same settings as the previous section: 4 proximate sources have been activated with sinusoidal and Gaussian waveforms; the forward models have been generated from two head models (three-shell and realistic); and 3 samples have been drawn from the data sequence for localization using SAFFIRE. Approximately one sixth of the total cortex surface around the desired location is included in the iterative search of the SAFFIRE.

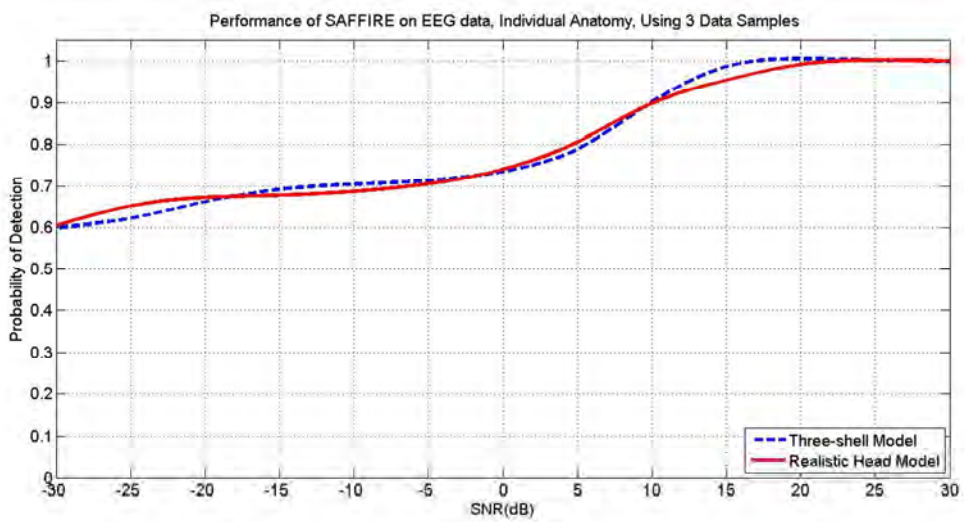

Figure 8.3: Probability of Detection of 4 proximate sources using SAFFIRE algorithm, from EEG data, on individual anatomy, using 3 data samples

Figure 8.3 and Figure 8.4 show the results in terms of the probability of detection and MSE. Figure 8.3 suggests that the detection rate rises as SNR increases, which is an expected behavior. Starting at 0.6 for SNR as low as -30 dB, localization on both head

models seems to rise gradually in terms of probability of detection, and for SNR around +18 dB both models seem to result in full recovery of the 4 sources, using only 3 data samples.

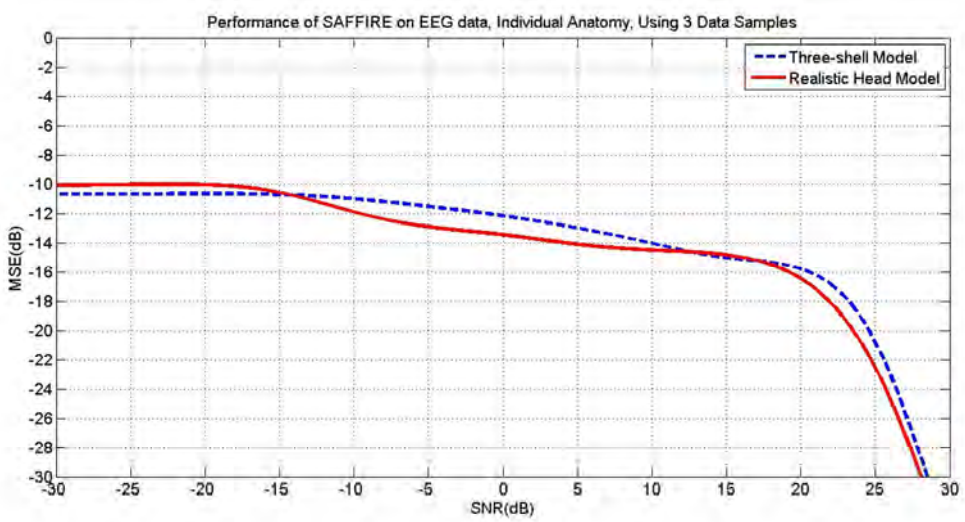

Figure 8.4: MSE for recovery of 4 proximate sources using SAFFIRE algorithm, from EEG data, on individual anatomy, using 3 data samples

Figure 8.4 also suggests that localization improves in terms of MSE as SNR increases, for both head models. Initially at -10 dB for SNR around -30 dB, MSE falls to -30 dB as SNR reaches about +28 dB.

Compared to the Colin anatomy, this second head anatomy shows better performance early on (for low SNR) in terms of detection rate and MSE, but as SNR increases, it does not converge to the accurate localization scenario (probability of 1 and MSE below -30 dB) as fast as Colin anatomy does. Still the fact that this kind of performance can be achieved with only 3 samples of data shows the effectiveness of the SAFFIRE algorithm, on different head models and different anatomies.

8.3 Forward Model Uncertainties

In this section, the effect of forward model uncertainties on the performance of SAFFIRE for EEG application is investigated. Among the head surfaces, skull is the most controversial one; the shape, thickness and conductivity associated with the skull can

vary significantly from one person to another. Moreover, EEG signals are greatly affected by the conductive properties of the skull. If these parameters are not estimated properly for the formulation of the forward problem, the inverse solution is affected adversely; i.e. huge localization errors can appear in the results.

As mentioned in section 6.3 of this report, various skull conductivity values have been reported in the literature. The baseline conductivity ratio in the simulations of this report, thus far, has been the default value in Brainstorm software, which is 1:1/80:1 for the cortex, skull and scalp respectively; however, since exact information about the skull conductivity and thickness has been used for solving the inverse problem in all cases, any other conductivity ratio would result in similar localization performance. Figure 8.5 shows the performance of SAFFIRE on EEG data for localization of 4 proximate sources using 3 data samples, for two different conductivity ratio scenarios. The two curves follow closely, with a slight advantage in 1/20 case.

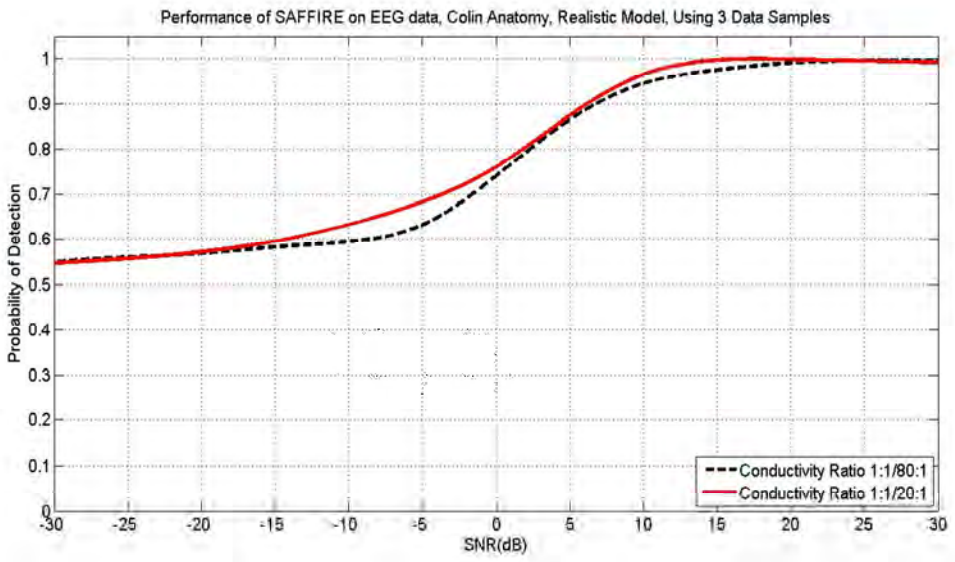

Figure 8.5: Probability of detection of 4 proximate sources using SAFFIRE algorithm, from EEG data, for two conductivity ratios, using 3 data samples

If one has more accurate information about the skull thickness and conductivity for a subject, a customized forward solution can be developed for an individual. Skull shape and thickness can be inferred from MRI images of the subject head. Conductivity value, however, is more difficult to estimate. Several papers report conductivity values for live and post-mortem skull tissues [60] [61]. The relationship between the skull

conductivity and age of the subject derived in these papers can be used as a guideline in conductivity estimation for different subjects [60] [61]. Figure 8.6 shows reported conductivity values of live skull samples temporarily removed during epileptic surgery plotted against patient age [62]. The thick blue trend with circles graphs raw data and the thin gray trend with dots graphs the least squares fit (reproduced from [60]). The graph suggests that skull conductivity drops as age increases.

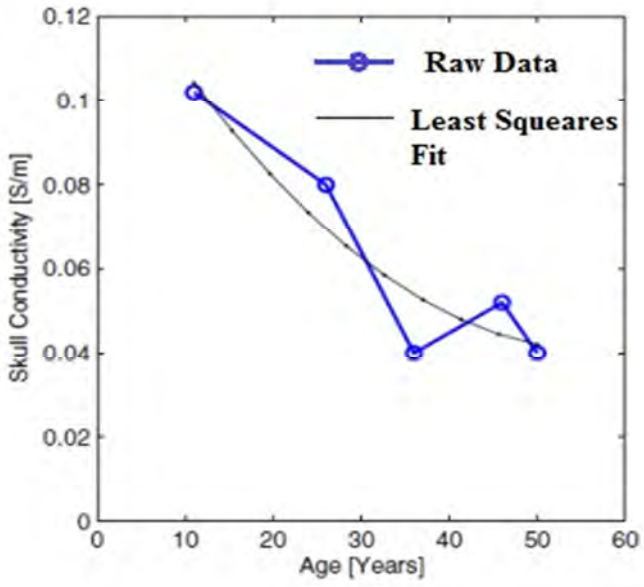

Figure 8.6: Estimated skull conductivity versus age [60][62]

In this section, the goal is to see how uncertainties in the forward model, arising from misestimation of the skull thickness and conductivity, affect the performance of SAFFIRE for EEG data.

8.3.1 Misestimation of skull thickness

Since the Brainstorm software cannot accommodate variation in skull thickness for realistic head models, the following simulations were run on three-shell head model for Colin anatomy. The settings for sources (number, location, and waveform) were adjusted identical to those of section 8.1. Two forward solutions (array manifolds) were generated for skull thicknesses of 5 and 6mm. Synthetic EEG signals were generated using one of the forward solutions (manifolds) and SAFFIRE was applied to these signals

with the other manifold, and vice versa. The physiological implication of this experiment is as follows: assume that EEG signals are collected from a head anatomy with a 5mm thick skull; if ones approximates the skull thickness as 6mm, how well can SAFFIRE perform the localization? And the other way around.

Figure 8.7 shows the results of the abovementioned experiment. The graph suggests that when the skull thickness is underestimated by only 1mm, probability of detection decreases by about 0.2. However, if the skull thickness is overestimated by the same amount, the performance of SAFFIRE is not much affected.

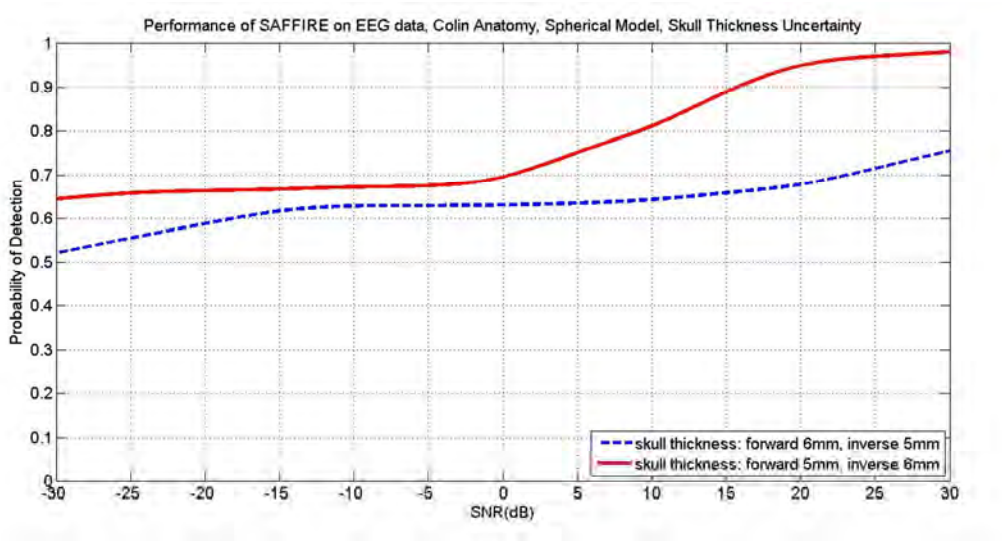

Figure 8.7: Performance of SAFFIRE in terms of probability of detection, for misestimated skull thickness

8.3.2 Misestimation of skull conductivity

The same procedure was repeated for creating forward solutions for Colin anatomy using spherical head models with different conductivity ratios for the brain, skull and scalp surfaces. One of the head models was based on 1:1/20:1 ratio, while the other was generated using 1:1/25:1 ratio for the brain, skull and scalp respectively.

Figure 8.8 shows that underestimating the relative conductivity of the skull with respect to the brain and scalp (dashed blue line) severely drops the probability of detection of the 4 sources using SAFFIRE. However, if the relative conductivity of the

skull is overestimated by the same amount, localization does not change for low SNRs (below -5dB) (compare to Figure 8.5), and for higher SNRs the adverse effect is about 0.2 drop in probability.

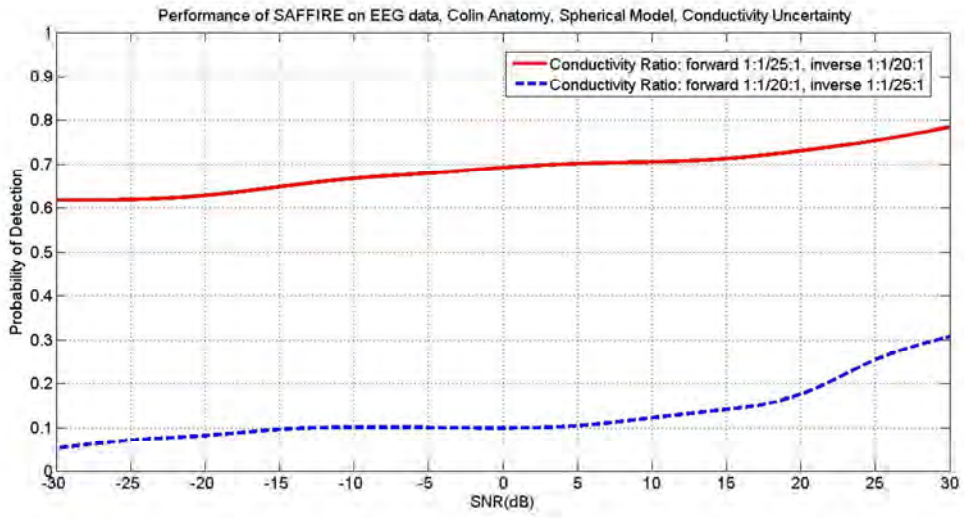

Figure 8.8: Performance of SAFFIRE in terms of probability of detection, for misestimated skull conductivity

Therefore, correct estimation of the conductivity ratio seems critical in brain source localization using EEG data. In addition to the conductivity versus age graph (Figure 8.6) other techniques have been proposed to estimate the skull conductivity for source localization. For example, in [63] the authors adopt an iterative optimization algorithm to simultaneously find optimum skull conductivity and localize the brain sources. In [64], a new method is proposed for combined MEG/EEG source localization. In this technique, the conductivities of a realistic FEM head model are optimized based on measured somatosensory evoked potentials and magnetic fields. This method uses the source parameters from the MEG dipole fit as a constraint for the conductivity estimation based on the EEG [64]. Another interesting approach was taken by authors of [65]. In this paper the authors select a number of the EEG electrodes that seem to be least affected by uncertainties of the conductivity, and use this subset of electrodes for solving the inverse problem [65].

In conclusion, conductivity profile is an ongoing issue in the localization of brain sources.

CHAPTER 9

CALIBRATION

So far in this research work, it was assumed that the theoretically derived array manifold (i.e. the solution of the forward problem) exactly matches the *actual* array manifold, which relates the activity of the sources in the brain to the sensor readings. However, in practice, small anomalies can cause significant discrepancy between the two. Any slight misplacement of the sensor electrodes, mutual coupling of sensors, or any other source of perturbations in the leadfield matrix causes the actual array manifold to differ from the nominal manifold which is available to the user. On the other hand, localization methods based on DOA estimation require that a precise characterization of the actual array manifold be available. Hence, *array calibration* techniques are applied to relate the actual and theoretical manifolds [66].

The SAFFIRE algorithm already contains an adaptive regularization term (R_z) that can account for the model error defined in its derivation (refer to section 6.5.5 for more details). This additional correction term tries to correct for certain modeled errors through the iterations of the algorithm.

In this chapter, the capability of the SAFFIRE to correct for modeling (calibration) errors is investigated for different head models using MEG and EEG synthetic data. These results are then compared with a more general transfer-function-based calibration technique from [66].

9.1 Iterative Calibration of SAFFIRE

The derivation of the model error term (R_z) for the SAFFIRE algorithm was demonstrated in section 6.5.5 of this report. In this section, the performance of SAFFIRE is investigated in the presence of calibration errors. To observe the effectiveness of the adaptive regularization term(R_z), localization is performed with and without this additional term using SAFFIRE. The results are compared in terms of the probability of detection of the two sources and the mean square error (MSE).

9.1.1 Calibration using MEG data

Synthetic MEG data was produced using the procedure explained in chapter 6 of this thesis and with the following settings: two head models (single sphere and realistic) have been developed on Colin anatomy. For each head model two sources have been activated in the brain, distanced 5cm apart from each other. The waveform assigned to each source is a sequence of random numbers picked from a normal distribution with mean of zero and standard deviation of 30nA.m; only 5 data samples have been used for localization purposes. Also, the sensor array used for the MEG data is the 151 CTF Helmet, and approximately one eighth of the cortex surface is included in the iterative search of SAFFIRE. As for the modeling errors, one percent error is induced on the diagonal elements of the array manifold. The error has normal distribution with zero mean and standard deviation 0.01.

Figures Figure 9.1 and Figure 9.2 demonstrate the effect of including the regularization (calibration) term of SAFFIRE (R_z), in the presence of modeling errors, in terms of probability of detection and MSE for localization.

Figure 9.1 suggests that modeling errors render SAFFIRE incapable of localizing the sources if the regularization term (R_z) is not included in the iterative estimation of the filter bank. The black solid line with circular markers shows the behavior of both head models in the absence of calibration term(R_z). Once this adaptive term is added to the iterative filter bank estimation, localization improves on both head models, but remains far from accurate. A maximum detection probability of 0.5 is achieved with SAFFIRE's iterative calibration term in this case, which means that for high SNR, on average one source out of two could be localized in the presence of modeling errors.

Figure 9.2 shows the mean square error in the localization of two sources, for the same experiment setup. The black solid line with circular markers corresponds to the MSE when the calibration term is not utilized in the algorithm. This high MSE corresponds to zero probability of detection in Figure 9.1. Once the adaptive regularization term is used in the updates of the aggregate filter bank, MSE decreases for both head models. For single sphere head model the improvement in MSE is 8-16 dB in SNR range of -30dB to +30dB. This improvement in MSE is between 10-22 dB for the realistic head model in the same SNR range.

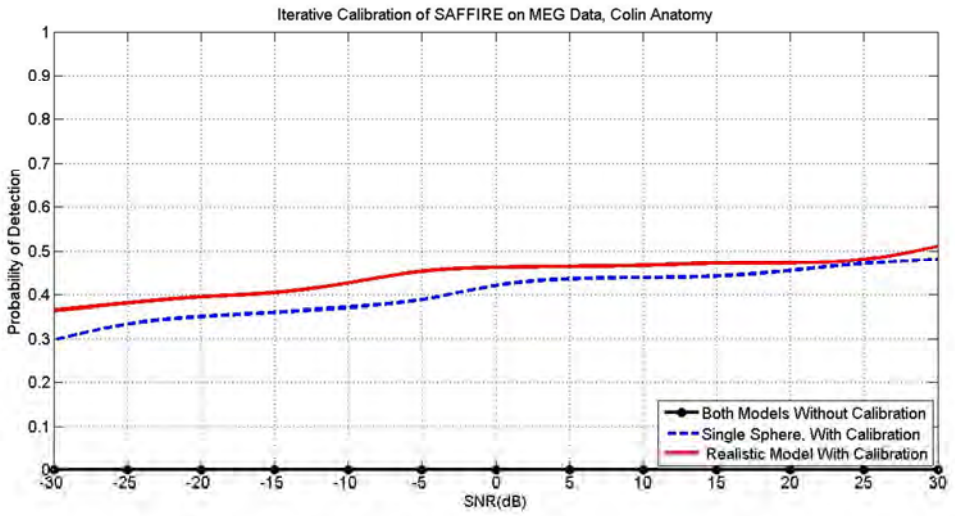

Figure 9.1: Effect of the Iterative Calibration of SAFFIRE on Probability of Detection of 2 Sources, from MEG data, 1% Diagonal Modeling Errors

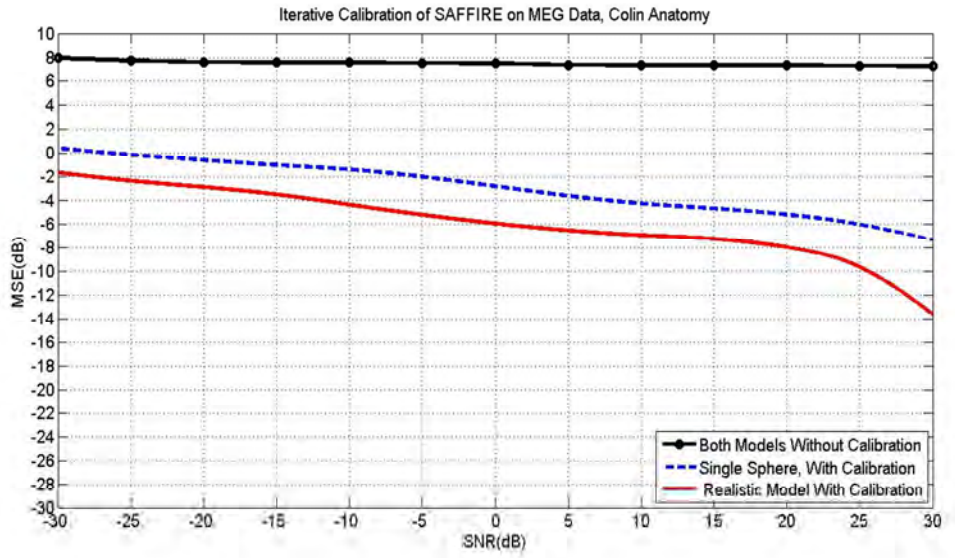

Figure 9.2: Effect of the Iterative Calibration of SAFFIRE on MSE in localization of 2 Sources, from MEG data, 1% Diagonal Modeling Errors

9.1.2 Calibration using EEG data (128 electrodes)

Synthetic EEG data was produced for two head models (three-shell and realistic) on Colin anatomy. For each head model two sources have been activated in the brain, distanced 5cm apart from each other. The waveform assigned to each source is a sequence of random numbers picked from a normal distribution with mean of zero and

standard deviation of 30nA.m; 5 data samples have been used for localization purposes. EEG data is assumed to be collected using a GSN 128 EEG cap. Approximately one tenth of the cortex surface is included in the iterative search of SAFFIRE. The model error has normal distribution with zero mean and standard deviation 0.01.

Figure 9.3 and Figure 9.4 demonstrate the effect of including the regularization (calibration) term of SAFFIRE(R_z), in the presence of modeling errors, in terms of probability of detection and MSE for localization of the two sources.

Figure 9.3 shows that the effect of calibration is more pronounced for EEG data collected from 128 EEG electrodes, compared to MEG data collected from 180 MEG coils (Figure 9.1). Considering that equal perturbation (1%) had been introduced to MEG and EEG manifolds, this graph suggests that EEG is less sensitive to slight modeling errors than MEG.

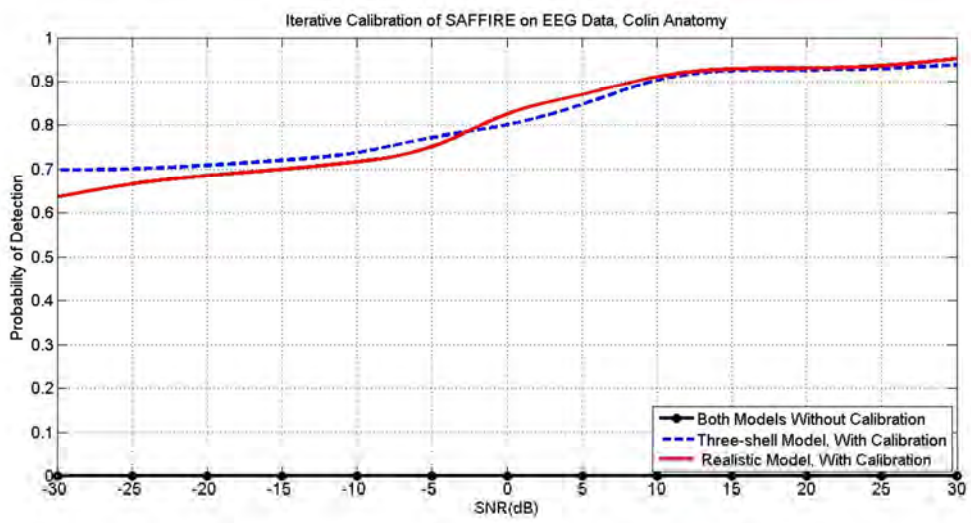

Figure 9.3: Effect of the Iterative Calibration of SAFFIRE on Probability of Detection of 2 Sources, from EEG data, 128 Electrodes, 1% Diagonal Modeling Errors

Figure 9.4 shows the improvement in MSE once the calibration term is included in SAFFIRE. Calibration offers 10-20 dB improvement in MSE for SNR in range of -30 to +30 dB on three-shell head model; and 10-26 dB improvement in MSE for similar SNR range on realistic head model. Once compared to Figure 9.2, one realizes that the improvement in MSE is more pronounced for EEG, compared to MEG, when equal modeling errors are imposed on their corresponding manifolds.

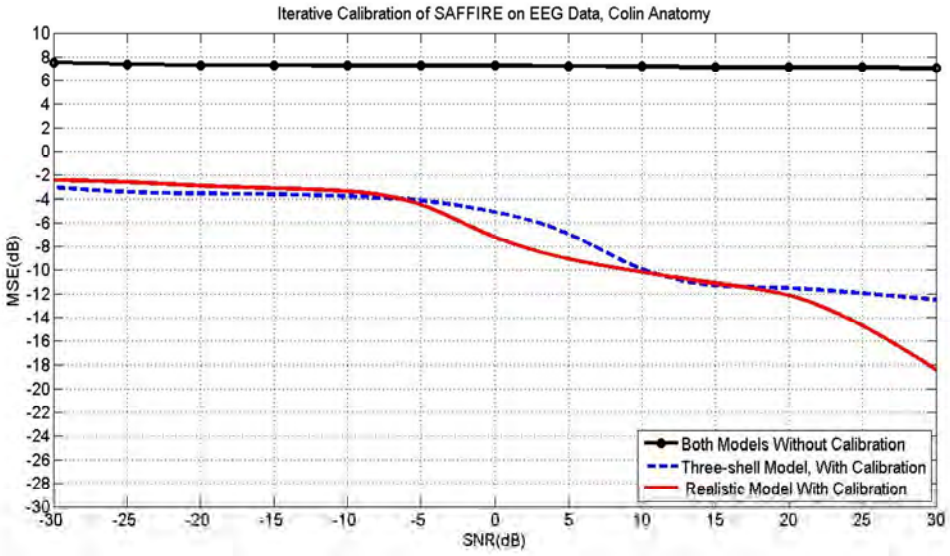

Figure 9.4: Effect of the Iterative Calibration of SAFFIRE on MSE in localization of 2 Sources, from EEG data, 128 Electrodes, 1% Diagonal Modeling Errors

So far in this research, EEG data was assumed to be collected from a GSN 128 EEG cap. However, different standard EEG caps exist in the market, and each one offers a different number of EEG electrodes. These caps include as few as 19 and as many as 256 EEG sensors. In the following section, the iterative calibration of SAFFIRE is applied to an EEG sensor array with 19 electrodes. The effect of calibration is observed for diagonal and non-diagonal model errors.

9.1.3 Calibration using EEG data (19 electrodes)

Synthetic EEG data is generated for Colin anatomy using realistic head model. Two sources with relative distance of 8cm are activated in the brain. Random samples are picked from a zero mean Gaussian distribution with standard deviation 30nA.m and assigned as the waveforms of the two sources. Only 3 data samples are used in the SAFFIRE for localization. Since the array size is very small (19), a smaller region of the cortex (one twentieth) containing the two sources is included in the iterations of SAFFIRE. One percent diagonal errors are induced on the array manifold.

Figure 9.5 and Figure 9.6 summarize the effect of calibration term on the performance of SAFFIRE in terms of probability of detection and mean square error (MSE).

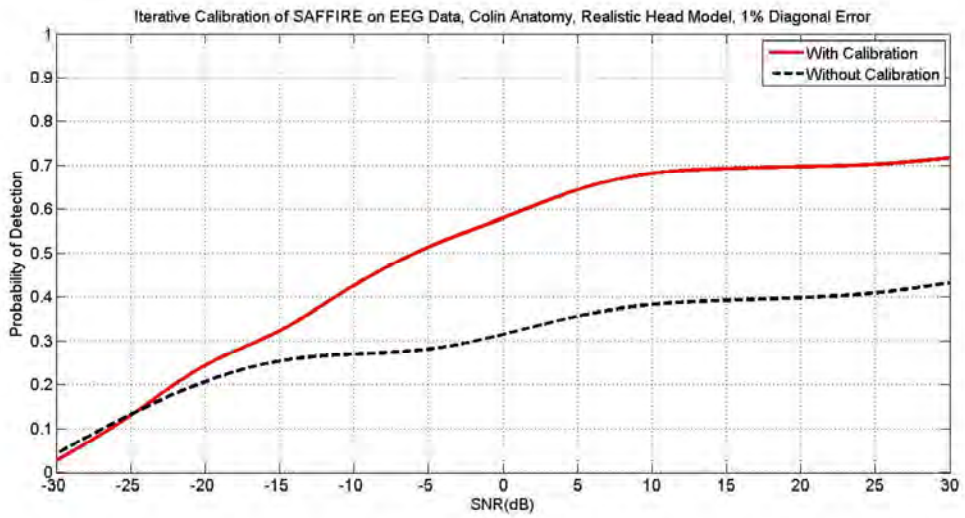

Figure 9.5: Effect of the Iterative Calibration of SAFFIRE on Probability of Detection of 2 Sources, from EEG data, 19 Electrodes, 1% Diagonal Modeling Errors

Figure 9.5 shows that without using the regularization terms (R_z) in SAFFFIRE, localization is poor for the two sources. A maximum probability of detection of about 0.4 is achieved for SNR as high as +30dB. With calibration, however, this figure rises to 0.7 for similar SNR. Lower SNRs result in lower detection obviously. The improvement in probability of detection is from 0.1 to 0.3 for SNR in range of -15 dB to +30 dB respectively. Figure 9.6 shows the MSE associated with the same experiment. The improvement in MSE is between 1-8 dB for SNR in the range of -15dB to +30 dB.

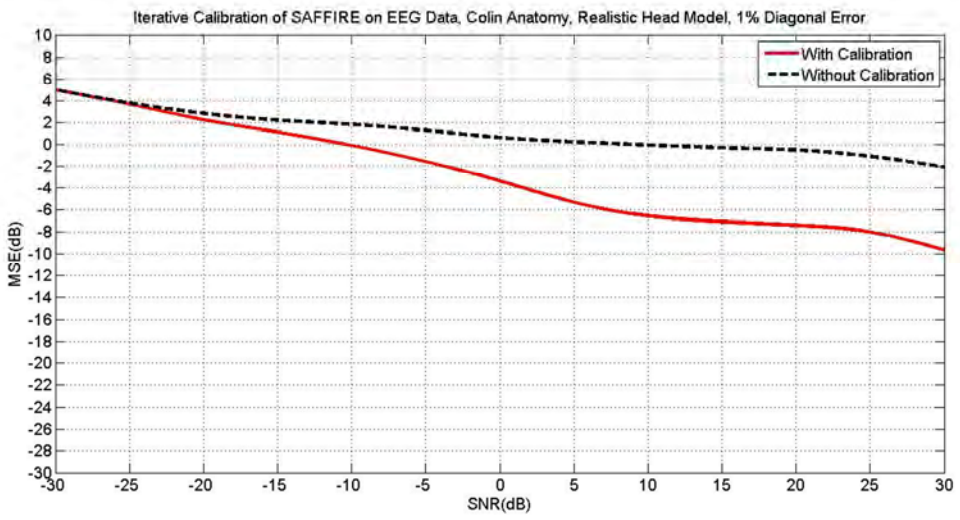

Figure 9.6 : Effect of the Iterative Calibration of SAFFIRE on MSE in localization of 2 Sources, from EEG data, 19 Electrodes, 1% Diagonal Modeling Errors

However, once the model error is changed to a more general case of non-diagonal errors, the results change. Figure 9.7 and Figure 9.8 reflect these findingd. In Figure 9.7 it is observed that the absence of the calibration term (R_z) results in almost zero detection of sources for all SNRs for non-diagonal model errors in the manifold. Inclusion of the R_z term improves the performance to some extent. The effectiveness of the calibration term becomes more pronounced as SNR increases; the maximum detection probability is 0.55 in this case.

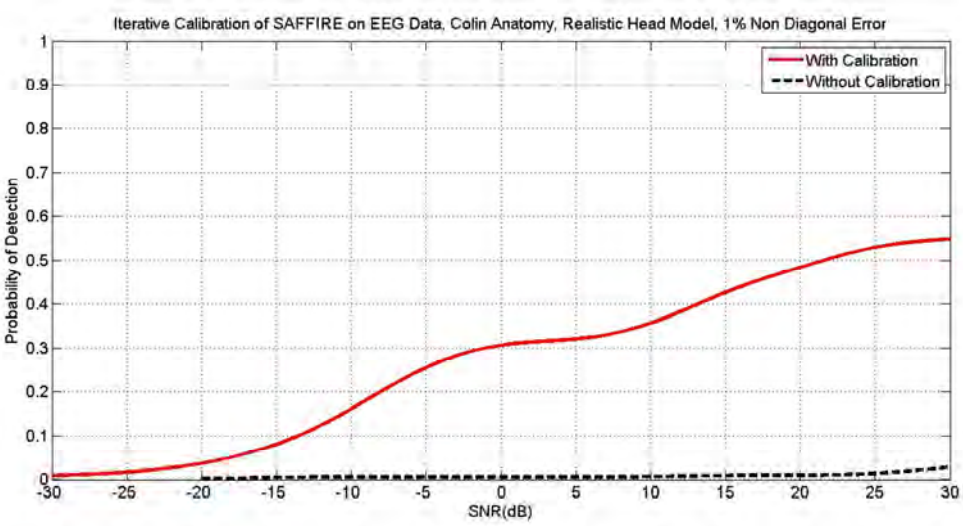

Figure 9.7: Effect of the Iterative Calibration of SAFFIRE on Probability of Detection of 2 Sources, EEG data, 19 Electrodes, 1% Non-Diagonal Modeling Errors

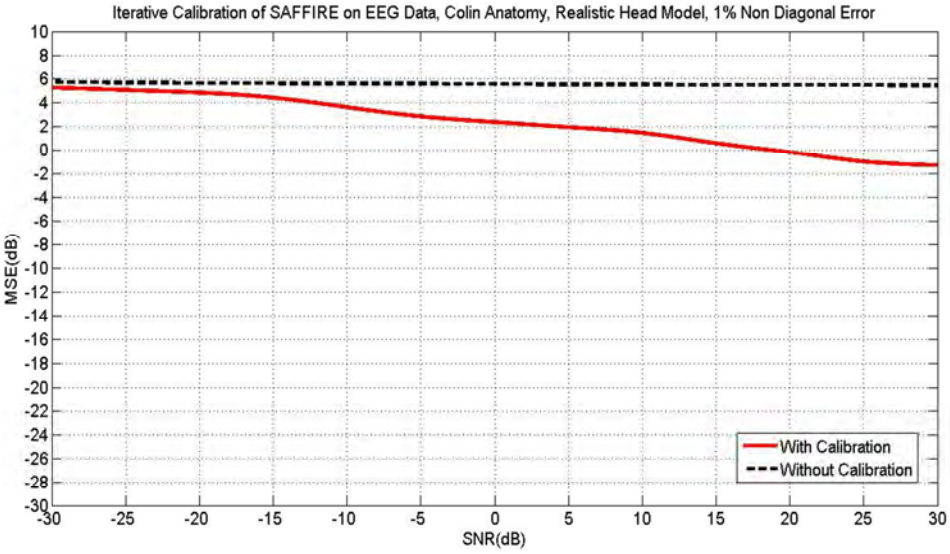

Figure 9.8: Effect of the Iterative Calibration of SAFFIRE on MSE in localization of 2 Sources, EEG data, 19 Electrodes, 1% Non-Diagonal Modeling Errors

Figure 9.8 demonstrates that the regularization term brings about 7 dB improvements in the MSE for high SNR, which is about 1dB less improvement compared to the diagonal error scenario.

9.2 Transfer Function Based Calibration Method

In this section, another calibration technique is applied to the case of brain signals collected from 19 EEG electrodes. This method utilizes a transfer function based approach and can be used for *external calibration* or *auto-calibration* [66].These terms will be introduced shortly. Note that the transfer function based calibration method can accommodate both diagonal and non-diagonal modeling errors.

External array calibration is used when the position of a number of sources is known; this information is used to estimate the relationship between the actual and theoretical array manifolds. External calibration can be used when one has access to exact location of adequate number of sources (typically more than the number of array elements). The disadvantage of this method is that any variations in the environmental conditions will require the calibration parameters to be updated. On the other hand, auto-calibration is based on a process of sequential optimization that uses signals of opportunity in the environment for two simultaneous purposes: (1) to update the calibration parameters; and (2) to refine the estimates of the source locations [66]. Hence, only approximate knowledge of the source locations is required in the latter technique in order to find the relationship between the nominal and actual array manifolds, as well as finding the exact location of the underlying sources.

In the application of brain source localization, the modeled array manifold is obtained from the *forward solution*, which depends on the head model and sensor array configuration. Known sources can be chosen in the functionally mapped parts of the brain, by creating evoked responses using pertinent stimulation types (auditory, visual, somatosensory). Actual manifold can be inferred from brain signal recordings.

In the following sections, the mathematical model used in the transfer function based calibration technique is explained for external and auto-calibration scenarios.

9.2.1 External Array Calibration

Suppose an N element sensor array is used to collect signals from K known and distinct sources. Let $\boldsymbol{v}_m$ and $\boldsymbol{z}_m$ represent the $N \times 1$ modeled and measured array steering vectors, respectively for source m , where $m = 1 \ldots K$, and $K \geq N$. Define [66]:

$$\boldsymbol{V} \triangleq [\boldsymbol{v}_1 \quad \boldsymbol{v}_2 \quad \ldots \quad \boldsymbol{v}_K] \tag{9.1}$$

$$\boldsymbol{Z} \triangleq [\boldsymbol{z}_1 \quad \boldsymbol{z}_2 \quad \ldots \quad \boldsymbol{z}_K] \tag{9.2}$$

The objective of calibration is to compute a calibration matrix $A \in \mathbb{C}^{N \times N}$ such that $\boldsymbol{Z} \approx \boldsymbol{A}\,\boldsymbol{V}$. In other words, one needs to find a calibration matrix that can yield a good approximation to the actual (measured) steering vector when it is applied to the modeled (nominal) steering vector. One way to quantify the goodness of this approximation is using the least squares criterion [66]:

$$\boldsymbol{J}_{LS} \triangleq \sum_{m=1}^{K} \|\boldsymbol{z}_m - \boldsymbol{A}\boldsymbol{v}_m\| \tag{9.3}$$

One approach to compute the calibration matrix is to minimize the least-squares cost function [66]:

$$\underset{\boldsymbol{A}}{\operatorname{argmin}}\, \boldsymbol{J}_{LS} = \underset{\boldsymbol{A}}{\operatorname{argmin}} \|\boldsymbol{Z} - \boldsymbol{A}\boldsymbol{V}\|_F^2 \tag{9.4}$$

where the subscript F denoted the Frobenius norm. The optimal solution for the calibration matrix is found by taking the derivate of the cost function with respect to $\boldsymbol{A}$ and equating that to zero [66]:

$$\frac{\partial \boldsymbol{J}_{LS}}{\partial \boldsymbol{A}} = \frac{\partial}{\partial \boldsymbol{A}}\, tr\,\{(\boldsymbol{Z} - \boldsymbol{A}\boldsymbol{V})^T \times (\boldsymbol{Z} - \boldsymbol{A}\boldsymbol{V})\} = 2(\boldsymbol{Z} - \boldsymbol{A}\boldsymbol{V})\boldsymbol{V}^T \tag{9.5}$$
$$= 0$$

Thus,

$$\boldsymbol{A} = \boldsymbol{Z}\,\boldsymbol{V}^T(\boldsymbol{V}\boldsymbol{V}^T)^{-1} = \boldsymbol{Z}\boldsymbol{V}^{\#} \tag{9.6}$$

where $\boldsymbol{V}^{\#} = \boldsymbol{V}^T(\boldsymbol{V}\boldsymbol{V}^T)^{-1}$ is the pseudo-inverse of $\boldsymbol{V}$.

The calibration matrix minimizes the distance between the measured and modeled steering vectors, and improves localization of techniques based on DOA estimation.

9.2.2 Array Self-Calibration (auto-calibration)

In this approach, using approximate locations of adequate sources ($K \geq N$), signals of opportunity are used for simultaneous localization of sources and update of the calibration parameters. Hence, the calibration matrix estimate is constructed from the set of actual steering vectors ($\boldsymbol{Z}$) and modeled steering vectors of the source location estimates $\widehat{\boldsymbol{V}}$ at each iteration [66]:

$$\boldsymbol{A} = \boldsymbol{Z}\widehat{\boldsymbol{V}}^{\#} \tag{9.7}$$

A tolerance should be defined for the change in Frobenius norm of the calibration matrix to stop the iterations. The following flow chart summarizes the stages included in array auto-calibration.

If it is assumed that manifold perturbations can be adequately modeled by correcting each sensor by a constant, then the calibration matrix takes on a simple diagonal structure. A more general calibration matrix has non-diagonal form and accounts for more complicated modeling errors. Both of the above calibration matrix forms (diagonal and non-diagonal) are applied to EEG manifolds in the following sections, and the results are quantified in terms of probability of detection and MSE for a calibrated EEG array of 19 electrodes compared to an un-calibrated array of the same size.

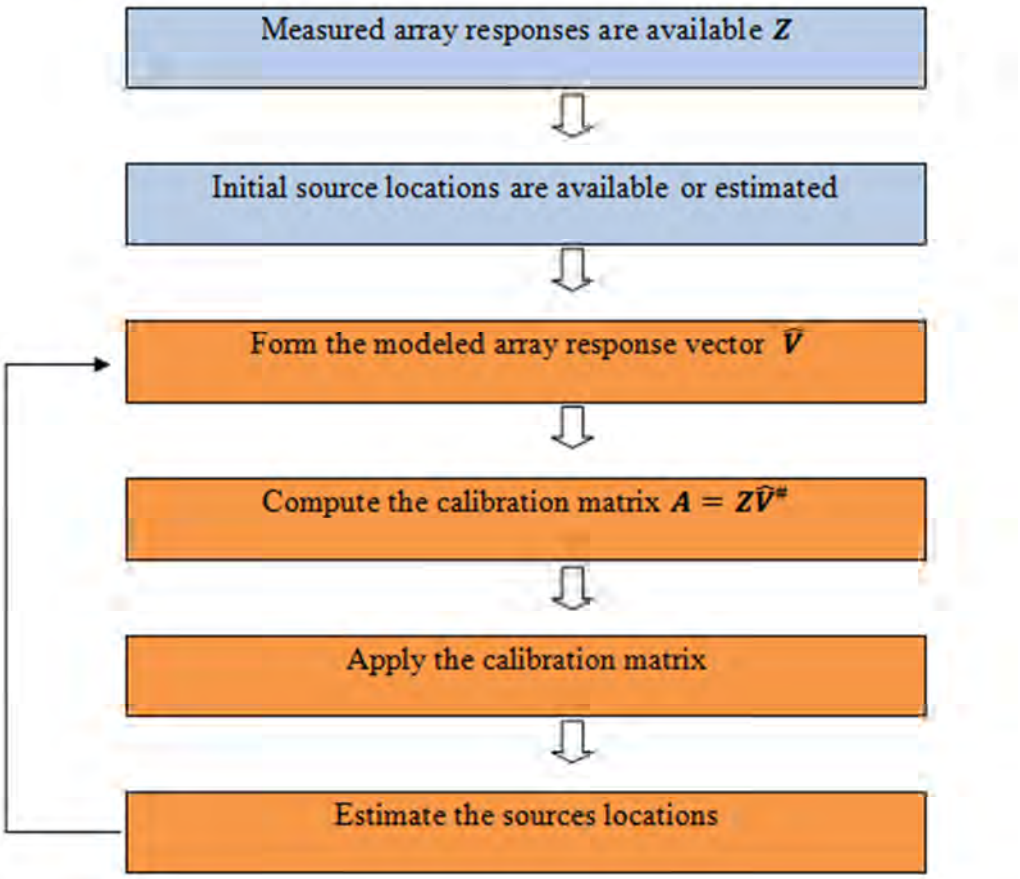

Figure 9.9: Flow-chart depicting iterative stages of autocalibration [66]

9.2.3 Performance on EEG data (19 electrodes)

Synthetic EEG data is generated for Colin anatomy using realistic head model. Two sources with relative distance of 8cm are activated in the brain. Random samples are picked from a zero mean Gaussian distribution with standard deviation 30nA.m and assigned as the waveforms of the two sources. Only 3 data samples are used in the SAFFIRE for localization. Since the array size is very small (19), a small region of the cortex (one fourteenth) containing the two sources is included in the iterations of SAFFIRE. One percent diagonal and non-diagonal errors are induced on the array manifold. Figure 9.10 and Figure 9.11 show the results for diagonal error case, in terms of probability of detection and MSE.

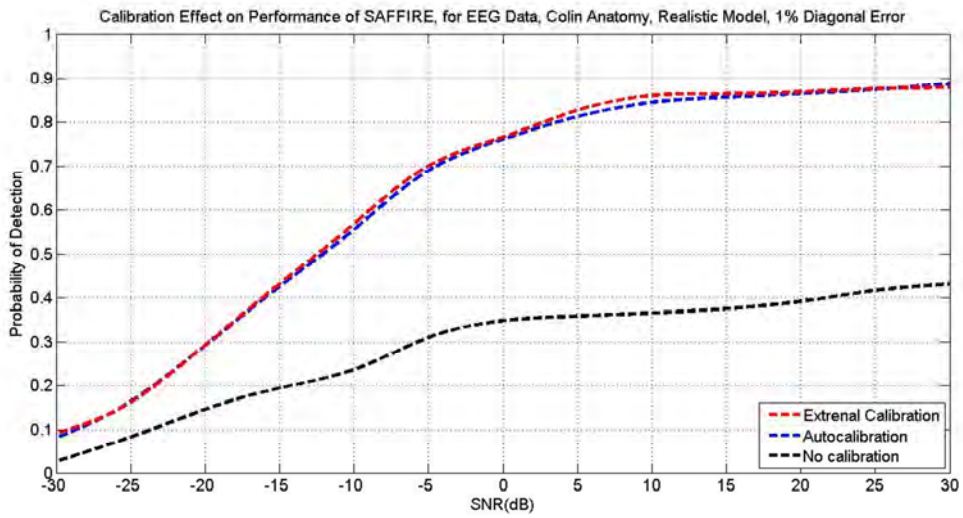

Figure 9.10: Effect of the Transfer Function Based Calibration on Probability of Detection of 2 Sources, EEG data, 19 Electrodes, 1% Diagonal Modeling Errors

Figure 9.10 shows considerable improvement in probability of detection when the array is calibrated. Note that external calibration offers the same performance that having exact knowledge of the array manifold would. Autocalibration follows the external calibration closely in this case. Detection reaches about 0.9 for high SNR. Calibration has resulted in 0.07-0.45 improvement in detection for SNR in the range of -30dB to +30dB. The maximum improvement in probability of detection using this calibration technique is 0.15 higher compared to the maximum progress offered by the iterative calibration of SAFFIRE for the same experiment setup (Figure 9.5).

Figure 9.11 demonstrates the improvement in MSE resulting from the transfer function based calibration technique. MSE improves 2-16 dB for SNR between -20 to +30 dB. The maximum improvement is 8dB more in this technique than what iterative calibration of SAFFIRE offers for the same scenario (Figure 9.6).

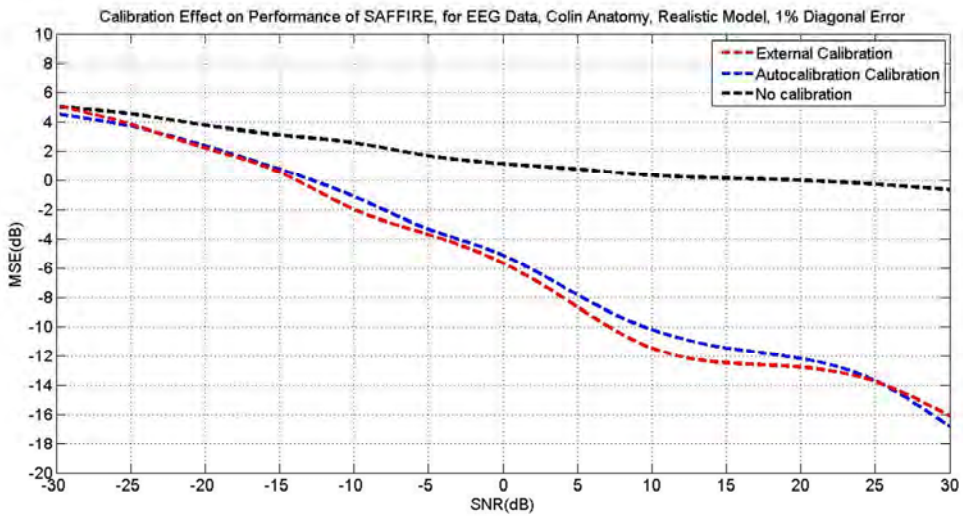

Figure 9.11: Effect of the Transfer Function Based Calibration on MSE for localization of 2 Sources, EEG data, 19 Electrodes, 1% Diagonal Modeling Errors

Once the error model is changed to the more general case of non-diagonal errors, the advantage of this calibration technique becomes even more pronounced. Figure 9.12 and Figure 9.13 show the effect of calibration on localization of the same two sources from EEG data collected from 19 electrodes. One percent non-diagonal error has been induced on the array manifold.

Figure 9.12 suggests that without calibration, non-diagonal errors render SAFFIRE incapable of any localization. With calibration, however, detection varies between 0.1 and 0.9 for SNR in range of -30dB to +30dB. The maximum detection in this case is 0.35 higher than what iterative calibration of SAFFIRE could offer for non-diagonal errors (Figure 9.7).

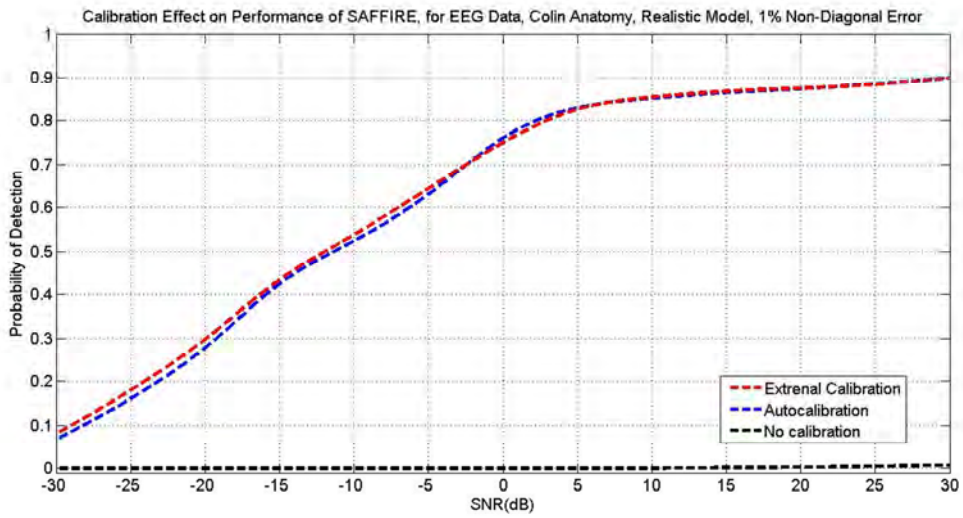

Figure 9.12: Effect of the Transfer Function Based Calibration on Probability of Detection of 2 Sources, EEG data, 19 Electrodes, 1% Non-Diagonal Modeling Errors

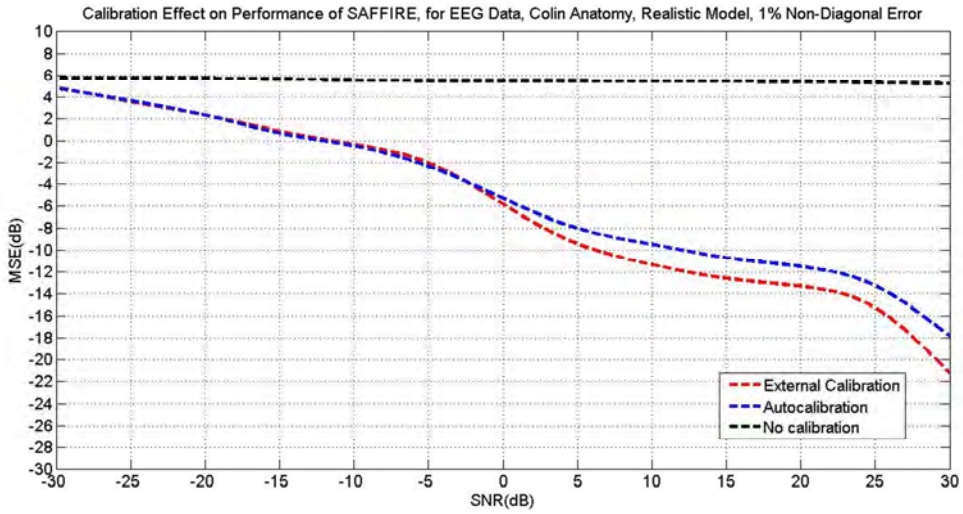

Figure 9.13: Effect of the Transfer Function Based Calibration on MSE for localization of 2 Sources, EEG data, 19 Electrodes, 1% Non-Diagonal Modeling Errors

Figure 9.13 shows the improvement in performance in terms of MSE. MSE improves 1-25 dB for SNR between -30dB and +30dB. Maximum improvement is 18 dB more than maximum improvement using SAFFIRE's calibration for non-diagonal errors (Figure 9.8).

CHAPTER 10

SOURCE RECONSTRUCTION

In this chapter, the sources correctly localized using the SAFFIRE are mapped into the brain for visualization, and comparison of the accuracy and resolution with another technique (WMNE). WMNE is based on the minimum norm estimate (MNE) technique which has a similar filter bank derivation as the SAFFIRE, except that MNE is not iterative, hence the lower resolution [58]. Weighted MNE (WMNE) is a modification of MNE that tries to remove the superficial source bias in MNE results.

In this chapter the localization results of SAFFIRE are demonstrated on MRI images, and compared visually with WMNE results.

10.1 Mapping the Sources Recovered from MEG Signals

In this section, the result of localization of sources from MEG signals is demonstrated. SAFFIRE results are compared with the results of WMNE method.

Figure 10.1 shows the 4 proximate sources of section 7.1 correctly localized from MEG signal on Colin anatomy. Though the distance between any two of the sources is only 3-5mm, the sources have been resolved using SAFFIRE.

Figure 10.2 shows the same 4 sources localized using WMNE. Even though higher SNR was provided in this case and a 60% hard threshold was applied after the localization to improve the resolution of WMNE, still the result is far inferior to that of SAFFIRE.

10.2 Mapping the Sources Recovered from EEG Signals

The same four sources were localized using SAFFIRE from EEG signals. The correctly localized sources appear in Figure 10.3. Figure 10.4 shows the result of applying WMNE to EEG signals arising from the same four proximate sources. High SNR has been provided for WMNE and 70% hard threshold has been applied as well.

Still, the results are imprecise and inaccurate. In fact, the advantage of employing SAFFIRE seems more pronounced on EEG data, compared to MEG.

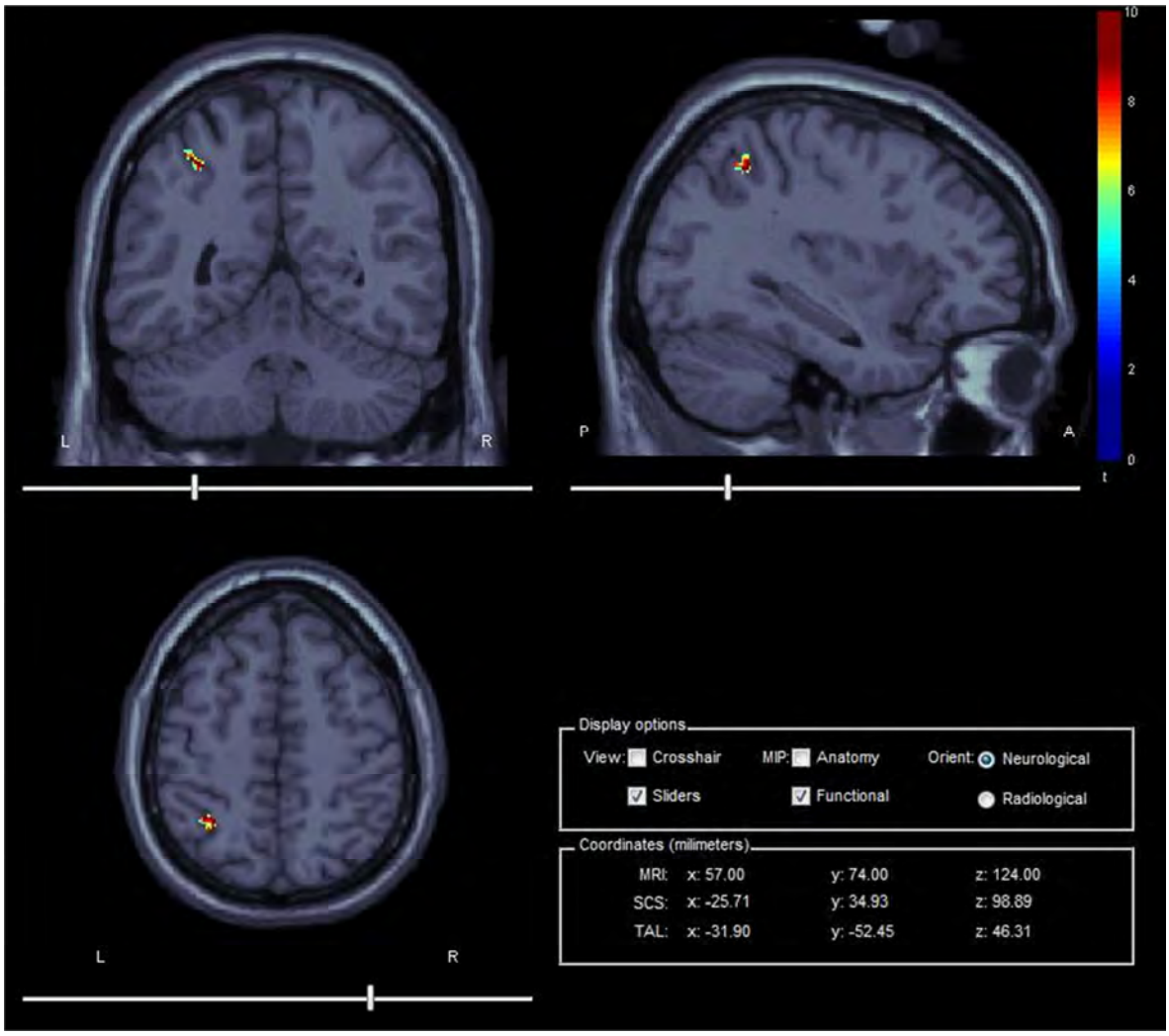

Figure 10.1: Four proximate sources correctly recovered using SAFFIRE, from MEG signals, mapped onto cortex and visualized on MRI images

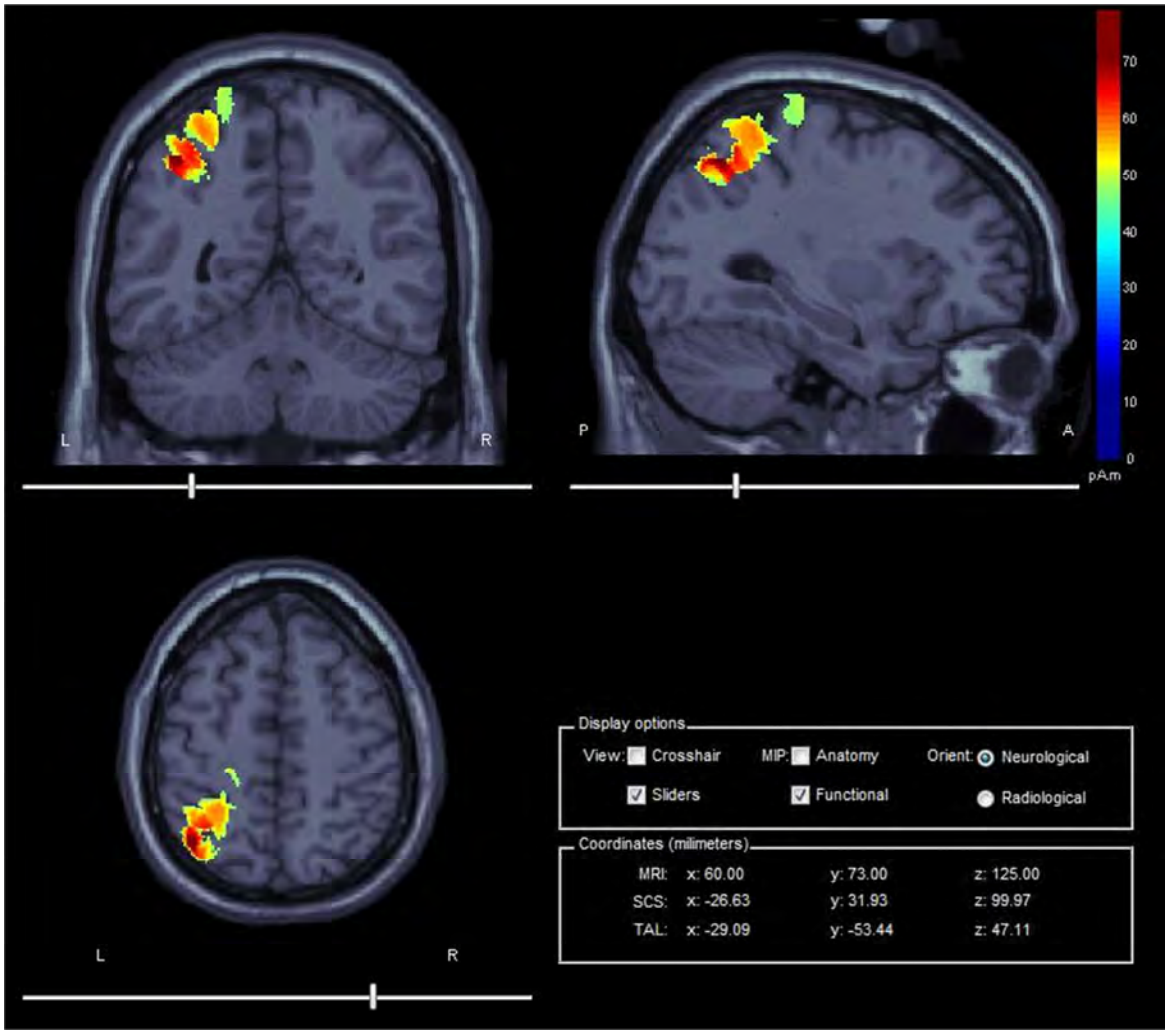

Figure 10.2: Localization results of WMNE for 4 proximate sources, using MEG signals, mapped onto cortex and visualized on MRI images

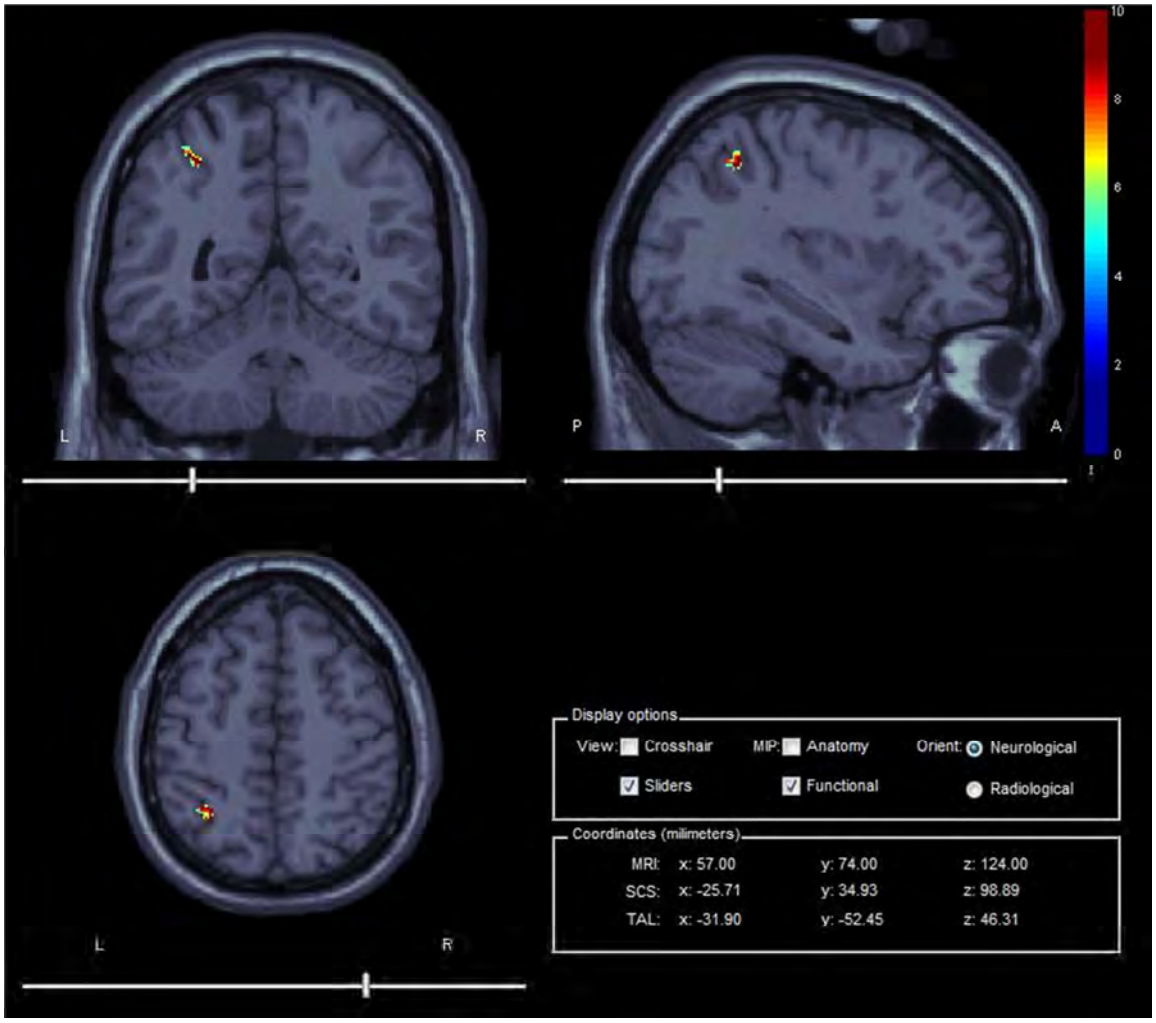

Figure 10.3: Four proximate sources correctly recovered using SAFFIRE, from EEG signals, mapped onto cortex and visualized on MRI images

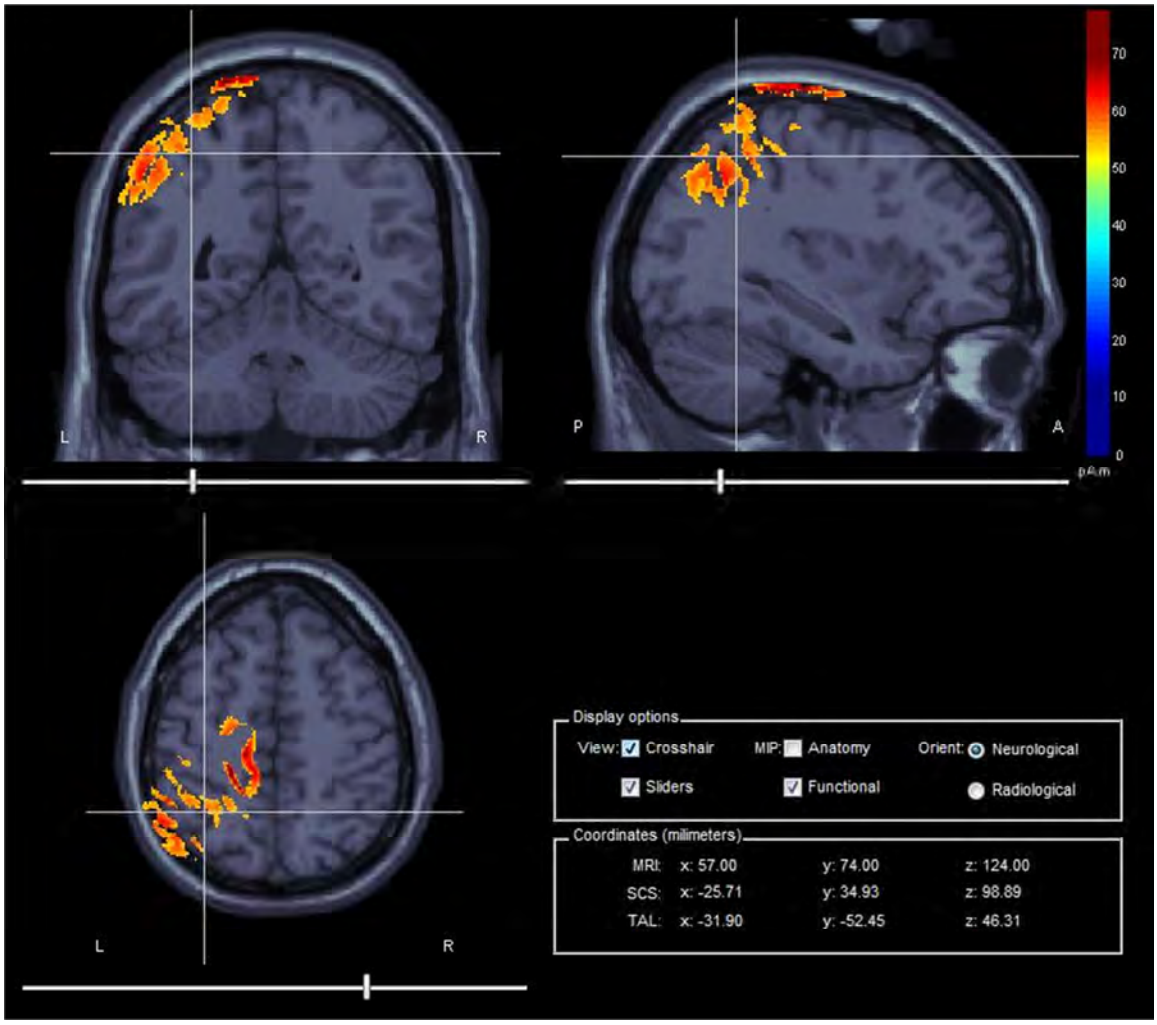

Figure 10.4: Localization results of WMNE for 4 proximate sources, using EEG signals, mapped onto cortex and visualized on MRI images

10.3 Waveform Reconstruction

Throughout this report, only the location of the recovered sources were reported for different cases. However, SAFFIRE is capable of reconstructing the amplitude of the sources as well. Once the recursions of SAFFIRE come to a stop, the final filter can be applied to the acquired brain signals (MEG/EEG) to reconstruct the source waveforms in time. Since the columns of the lead field matrix had been normalized before being utilized in SAFFIRE (see section 6.5.3.) the recovered source amplitudes need to be de-normalized by the norms of their corresponding steering vectors. Figure 10.5-Figure 10.8 show the waveforms of the four sources reconstructed from 40 data samples, and compared to the original waveforms.

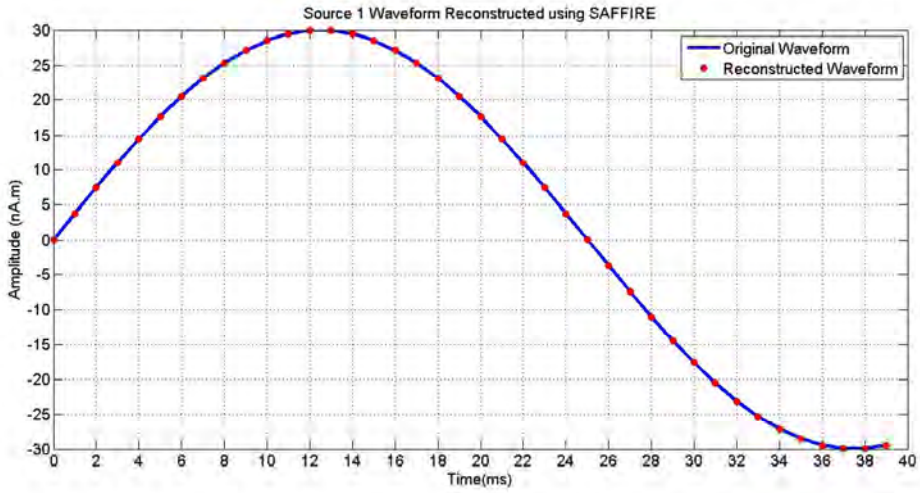

Figure 10.5: Waveform of source 1, reconstructed from SAFFIRE

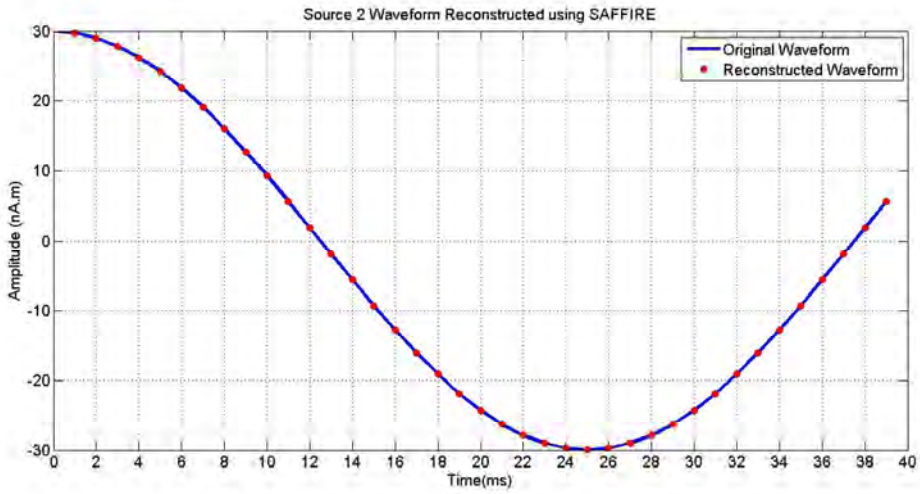

Figure 10.6: Waveform of source 2, reconstructed from SAFFIRE

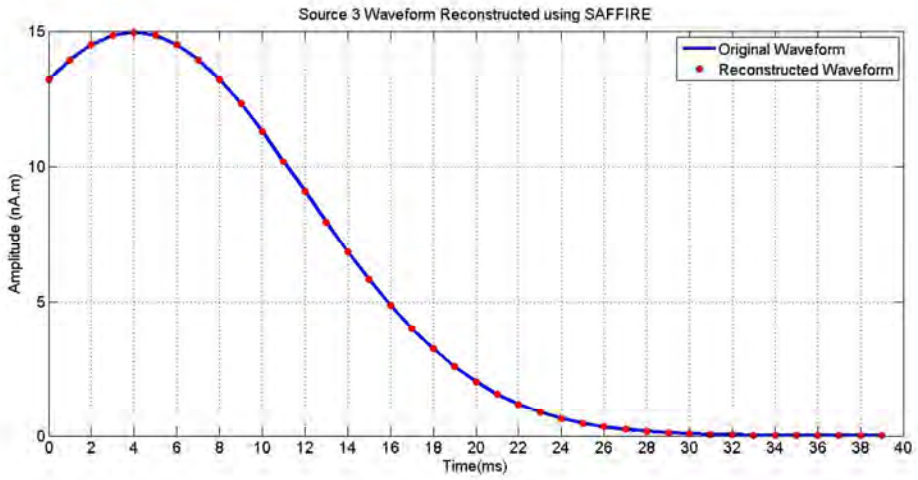

Figure 10.7: Waveform of source 3, reconstructed from SAFFIRE

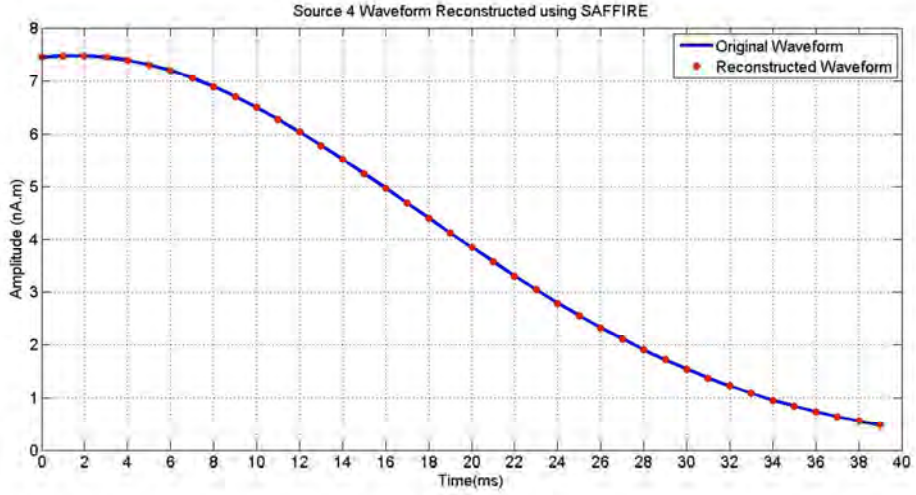

Figure 10.8: Waveform of source 4, reconstructed from SAFFIRE

CHAPTER 11

CONCLUSIONS AND FUTURE WORK

11.1 Conclusions:

In this thesis, a high resolution DOA technique (called SAFFIRE) originating from the RADAR field was used for the biomedical application of brain source localization. This algorithm is based on a recursive implementation of the minimum mean-square error (MMSE) estimation. The performance of this method was verified for synthetic MEG and EEG recordings for different head models on two different head anatomies. This technique does not require formation of a sample covariance matrix (SCM) or any eigen decomposition. It was shown through extensive simulations on MEG and EEG signals that this method can offer very high spatial resolution from very small sample support. It also provides a good extent of robustness against temporal correlation between sources. The SAFFIRE can also determine the model order automatically, reconstruct the waveform in time, and account for mild modeling errors.

Moreover, the effect of forward model uncertainties was investigated for EEG application. The simulations suggest that a rather accurate characterization of the skull thickness and conductivity is required for correct localization of brain sources from EEG signals. A more specific observation was that overestimation of the skull thickness and conductivity is a safer approach than underestimating their values.

Furthermore, the effect of modeling errors on the performance of SAFFIRE was investigated. Later, two calibration techniques were implemented to improve localization in the presence of modeling errors. Once the first calibration technique (iterative calibration of SAFFIRE) was applied to MEG and EEG signals for dense arrays (of size 180 and 128 respectively) with the same amount of imposed modeling error (1%), it was observed that EEG array responded better to calibration. In a sense, EEG signals seem to have been less sensitive to slight modeling errors than MEG recordings. Improvement of performance was quantified in terms of probability of detection and mean square error for

a practical range of signal to noise ratios. Also it was also noticed that the effectiveness of the calibration term becomes more pronounced as SNR increases

However, once the model error was changed to a more general case of non-diagonal errors, the effectiveness of SAFFIRE's iterative calibration term declined, especially when applied to a smaller array size (19 EEG electrodes). Hence, another calibration method was implemented for this case. This transfer-function-based calibration method outperforms the iterative calibration of SAFFIRE for diagonal and non-diagonal model error forms.

Finally, the localized sources from EEG and MEG signals were mapped onto the brain. The spatial resolution of the SAFFIRE was compared against that of weighted minimum norm estimate technique (WMNE). It was observed that SAFFIRE offers much higher spatial resolution compared to WMNE, for much smaller sample support and SNR. Additionally, the advantage of employing SAFFIRE over WMNE seems even more pronounced on EEG data, compared to MEG. Finally the source waveforms were reconstructed in time and compared against the original waveforms. Source reconstruction was achieved with high resolution in space and time using SAFFIRE.

11.2 Future Work

This research work can be extended in many ways. First, more realistic head models can be obtained from software that offer finite element method (FEM) computations of the head geometry. Using such models, anisotropy and inhomogeneousness of different head layers can be accounted for in forward solutions. In addition other parts of the brain such as the cerebrospinal fluid (CSF) can be added to the head layers for more realistic models.

Another area that can be improved is the assumptions made about the dipole orientation and location. In this thesis (and many other researches) the direction of the current dipole (corresponding to a collection of pyramidal neurons firing at the same time) is assumed to be normal to the local cortex surface. This assumption is physiologically justified due to the fact that pyramidal neurons constitute 80% of cortical neurons and their anatomical arrangement is normal to the local cortex layer. However, a

more comprehensive study can be done if such restriction is not imposed on the orientation of the modeled sources. As for the location, neural activity is assumed to be originating from the cortex of the brain, because it contains most of the neurons in the brain and it is closer to the skull. In reality, however, deeper structures of the brain also generate fields that contribute to the recorded brain signals. Localizing these deeper sources is another active topic in this field.

Moreover, Brain source localization using the SAFFRIE can be performed using several arrays of sensors, with different number of electrodes. The spatial resolution can be compared to determine whether investing in a denser recorder is worth the cost.

Also, new approaches have emerged that include exploiting EEG and MEG signals simultaneously for brain source localization, which is costly, but may be worth the investment. These methods can be further investigated.

Another area that can benefit from more exploration is simultaneous optimization of source location and conductivity profile. To this end, also the transfer function based calibration introduced in this thesis can be applied to rectify the effect of forward model uncertainties.

Finally, the best way to verify the finding of this thesis and similar research work is to test the methods on real MEG/EEG recordings using evoked response experiments.

REFERENCES

[1] S. Baillet, J. C. Mosher, and R. M. Leahy, “Electromagnetic brain mapping,” *IEEE Signal Process. Mag*., vol. 18, no. 6, pp. 14–30, Nov. 2001.

[2] “Neuroimaging,” in *Wikipedia, the Free Encyclopedia* [online], Available: http://en.wikipedia.org/wiki/Neuroimaging, [20 May 2011].

[3] S. Moehrs, “Bioelectric field simulation and visualization: anisotropic conductivities for the skull and brain white matter,” M.S. thesis, Dept. Computaional Eng., Friedrich-Alexander Univ., Erlangen-Nuremberg, Germany, 2003.

[4] S. D. Blunt, T. Chan, and K. Gerlach, “Robust DOA estimation: The reiterative super-resolution (RISR) algorithm,” *IEEE Trans. Aerosp. Electron. Syst*., vol. 47, pp. 332–346, Jan. 2011.

[5] M. Popescu, S.D. Blunt, and T. Chan, "Magnetoencephalography Source Localization using the Source Affine Image Reconstruction (SAFFIRE) Algorithm," *IEEE Trans. Biomed. Eng.*, vol. 57, pp. 1652-1662, July 2010.

[6] L. O. Tanzer, “Numerical modeling in electro and magnetoencephalography,” Ph.D. dissertation, Dept. Eng. Physics and Math., Biomedical Eng. Lab., Helsinki Univ. of Technology, Espoo, Finland, 2006.

[7] “Neuron,” in *Wikipedia, the Free Encyclopedia* [online], Available: http://en.wikipedia.org/wiki/Neuron [1 Jan 2012].

[8] “Action potential,” *in Wikipedia, the Free Encyclopedia* [online], Available: http://en.wikipedia.org/wiki/Action_potential [20 May 2011]

[9] “Postsynaptic potential,” *in Wikipedia, the Free Encyclopedia* [online], Available: http://en.wikipedia.org/wiki/Postsynaptic_potential [20 May 2011]

[10] H.J. Wieringa, “MEG, EEG and the integration with magnetic resonance images,” Ph.D. dissertation , Biomagnetic Centre Twente, Univ. of Twente , Enschede, The Netherlands, 1993.

[11] S. Baillet. (2010). “Physiological sources of electromagnetic fields,” [online], Available:http://www.mcw.edu/MEG/AboutMEG/MEGPrinciples/Physiologicalsourcesofelectromagneticfields.htm [8 Jan 2012]

[12] “Brain: functional areas,” *in Encyclopedia Britannica* [online], Available: http://www.britannica.com/EBchecked/media/100577/Functional-areas-of-the-human-brain [8 Jan 2012]

[13] “The brain from top to bottom,” [online], Available: http://thebrain.mcgill.ca/flash/i/i_02/i_02_cl/i_02_cl_vis/i_02_cl_vis.html#3 [8 Jan 2012]

[14] C. Braun, “Physiological and physical basis of magnetoencephaolography,” Center for Mind/Brain Sciences, Dept. of Cognitive and Educational Sciences, Univ. of Trento, Italy.

[15] “Magnetoencephalography” *in Wikipedia, the Free Encyclopedia* [online], Available: http://en.wikipedia.org/wiki/Magnetoencephalography [8 Jan 2012]

[16] S. Tong and N.V.Thacor, *Engineering in Medicine & Biology- Quantitative EEG Analysis Methods and Clinical Applications*, Boston/London: Artech House, 2009.

[17] S.Tissari, “Neuromagnetic source localization using anatomical information and advanced computational methods,” Ph.D. dissertation, Dept. Eng. Physics. Maths., Helsinki Univ.of Technology, Espoo, Finland, 2003.

[18] J. Malmivuo, R. Plonsey, *Bioelectromagnetism: Principles and Applications of Bioelectric and Biomagnetic Fields*, Oxford, NY: Oxford University Press, 1995. [online].Available: http://www.bem.fi/book/ [10 Dec 2011]

[19] “Electroencephalography,” *in Wikipedia, the Free Encyclopedia* [online]. Available: http://en.wikipedia.org/wiki/Electroencephalography [20 May 2011]

[20] “Basic principles of magnetoencephalography,” [online]. Available: http://web.mit.edu/kitmitmeg/whatis.html [20 May 2011]

[21] T. Herdman, “Dipole modeling applied in cognitive neuroscience,” presented at 15th Annual Meeting of the Organization for Human Brain Mapping, San Francisco, CA, June 18-23, 2009.

[22] F.T. Ulaby, E. Michielssen, and U. Ravaioli, *Fundamentals of Applied Electromagnetics*, Upper Saddle River, NJ: Prentice Hall, 2010.

[23] “Dipole,” *in Wikipedia, the Free Encyclopedia* [online]. Available: http://en.wikipedia.org/wiki/Dipole [8 Jan 2012]

[24] M. S. Hämäläinen and J. Sarvas, "Realistic conductivity geometry model of the human head for interpretation of neuromagnetic data," *IEEE Trans. Biomed. Eng.*, vol. BME-36, pp. 165-171, Feb. 1989.

[25] M.X. Huang, J.C. Mosher and R.M. Leahy, "A sensor-weighted overlapping-sphere head model and exhaustive head model comparison for MEG", *Phys. Med. Biol.*, vol. 44, no. 2, pp. 423-440, Feb. 1999.

[26] J. Sarvas, "Basic mathematical and electromagnetic concepts of the biomagnetic inverse problems," *Phys. Med. Biol.*, vol. 32, no. 1, pp. 11–22, Jan. 1987.

[27] J.C. Mosher, "From scalp to source estimates: imaging & localizing," *megcommunity.org*, Human Brain Mapping MEG/EEG Course. 2008. [online].Available: http://megcommunity.org/images/stories/Teaching_materials/HBM_MEGcourse_2008/mosher_hbm_meg_course2008.pdf [8 Jan 2012].

[28] R. Grech,T. Cassar, J. Muscat , K. P. Camilleri, S.G. Fabri, M. Zervakis, P. Xanthopoulos, V. Sakkalis, and B. Vanrumste, "Review on solving the inverse problem in EEG source analysis," *J. Neuroeng. Rehabil.*, vol. 5, p. 25, Nov. 2008.

[29] C. Lederman, A.A. Joshi, I.D. Dinov, J.D. Van Horn, L.A.Vese, and A.W. Toga, "Tetrahedral mesh generation for medical images with multiple regions using active surfaces," *Proc. IEEE Int. Symp. Biomed. Imaging*. *Rotterdam, 2010*, pp. 436–439.

[30] M. Hämäläinen, R. Hari, R. Ilmoniemi, J. Knuutila, and O. V. Lounasmaa, "Magnetoencephalography - theory, instrumentation, and applications to noninvasive studies of the working human brain," *Reviews of Modern Physics*, vol. 65, no.2, pp. 413-497, Apr. 1993.

[31] J.T. Cacioppo, L.G. Tassinary, and G.G. Berntson, *Handbook of Psychology*, NY: Cambridge University Press, 2007.

[32] F. Darvas, D. Pantazis, E. Kucukaltun-Yildirim, and R.M. Leahy, "Mapping human brain function with MEG and EEG: methods and validation." *J. Neuroimage*, vol. 23 Suppl. 1: pp. 289-99. 2004.

[33] D. Cheyne, J. Verba, "Biomagnetism" in *Encyclopedia of Medical Devices and Instrumentation*, Hoboken, N.J.: Wiley-Interscience, 2006.

[34] R. Grech,T. Cassar, J. Muscat , K. P. Camilleri, S.G. Fabri, M. Zervakis, P. Xanthopoulos, V. Sakkalis, and B. Vanrumste, "Review on solving the inverse problem

in EEG source analysis,*" J. Neuroengineering and Rehabilitation*, vol. 5, p. 25, Nov. 2008.

[35] F. Luan, C. Lee, J. Choi, and H. Jung, "A Comparison of regularization techniques for magnetoencephalography source reconstruction," *IEEE Trans. Magn.*, vol. 46, pp. 3209 - 3212, Aug. 2010.

[36] M. Hämäläinen and R. Ilmoniemi, "Interpreting magnetic fields of the brain: minimum norm estimates," Tech. Rep. TKK-F-A559, Helsinki University of Technology, Espoo, Finland, 1984.

[37] J. Foutz, A. Spanias, and M. K. Banavar, *Narrowband Direction of Arrival Estimation for Antenna Arrays*, Morgan and Claypool Publishers, 2008.

[38] S. Baillet, K. Friston, and R. Oostenveld, "Academic software applications for electromagnetic brain mapping using MEG and EEG," *Computational Intelligence and Neuroscience*, vol. 2011, July 2011.

[39] "Simbio," *Medical Physics Group,* Department of Diagnostic and Interventional Radiology at the Friedrich-Schiller University of Jena, Germany, [online], Available: https://www.mrt.uni-jena.de/simbio/index.php/Main_Page [8 Jan 2012]

[40] C. Wolters. "Simbio: General information." Personal email (Nov. 1, 2011).

[41] A. Gramfort, T. Papadopoulo, E. Olivi, and M. Clerc, **"**OpenMEEG: opensource software for quasistatic bioelectromagnetics,*" Biomed. Eng. Online*, vol. 9, no.45, Sept. 2010.

[42] F.Tadel, S. Baillet, J.C. Mosher, D. Pantazis, and R. M. Leahy, "Brainstorm: A user-friendly application for MEG/EEG analysis," *Computational Intelligence and Neuroscience*, vol. 2011, Article ID 879716, 2011.

[43] A. C. Evans, D. L. Collins, and B. Milner, "An MRI-based stereotactic atlas from 250 young normal subjects", *J. Society for Neuroscience Abstracts*, vol. 18, p. 408, 1992.

[44] P. Berg and M. Scherg, "A fast method for forward computation of multiple-shell spherical head models," *Electroenceph. Clin. Neurophysiol.*, vol. 90, pp. 58–64, 1994.

[45] L.A. Geddes and L.E. Baker, "Specific resistance of biological material – a compendium of data for biomedical engineer and physiologist," *Medical & Biological Eng.*, vol. 5, no. 3, pp. 271-293, 1967.

[46] S. Rush and D. A. Driscoll, “Current distribution in the brain from surface electrodes,” *Anesth. Analg.*, vol. 47, no.6, pp.717-723 , 1968.
[47] D. Cohen and B.N. Cuffin, “Demonstration of useful differences between magnetoencephalogram and electroencephalogram,” *Electroencephalogr. Clin. Neurophysiol.*, vol. 56, no.1, pp. 38–51, 1983.
[48] S. Homma , T. Musha , Y. Nakajima , Y. Okamoto , S. Blom , R. Flink , and K.E. Hagbarth, “ Conductivity ratios of the scalp-skull-brain head model in estimation of equivalent dipole sources in human brain,” *Neurosci Res* , vol. 22, no.1, pp. 51-55, 1995.
[49] J.D. Kosterich, K.R. Foster, and S.R. Pollack, “Dielectric properties of fluid saturated bone—the effect of variation in conductivity of immersion fluid,” *IEEE Trans Biomed Eng.*, vol. 31, no. 4, pp. 369–374, 1984.
[50] R. A. Oostendorp, J. Audet, and C. J. Eaves, “High-resolution tracking of cell division suggests similar cell cycle kinetics of hematopoietic stem cells stimulated in vitro and in vivo,” *Blood*, vol. 95, no.1, pp.855–862, Feb. 2000.
[51] T.C. Ferree, K.J. Eriksen, and D.M. Tucker, “Regional head tissue conductivity estimation for improved EEG analysis,” *IEEE Trans. Biomed. Eng.*, vol. 47, no. 12, pp.1584-1592, Dec. 2000.
[52] H. Hallez, B. Vanrumste, P.Van Hese, Y. D'Asseler, I. Lemahieu, and R.Van de Walle, “ A finite difference method with reciprocity used to incorporate anisotropy in electroencephalogram dipole source localization,” *Physics in Medicine and Biology*, vol. 50, pp. 3787-3806, 2005.
[53] S. Gonçalves , D.C. de Munck , J.P. Verbunt , R.M. Heethaar, and F.H. da Silva , “In vivo measurement of the brain and skull resistivities using an EIT-based method and the combined analysis of SEF/SEP data,” *IEEE Trans. Biomed. Eng.*, vol. 50, no.9, pp.1124-1128, July 2003.
[54] Y. Lai, W. van Drongelen, L. Ding, K.E. Hecox, V.L. Towle, D.M. Frim, and B. He, “In vivo human skull conductivity estimation from simultaneous extra- and intra-cranial electrical potential recordings,” *Clinical Neurophysiology*, vol. 116, no. 2, pp. 456-465, 2005.

[55] Y.C. Zhang, W. van Drongelen, and B. He, “Estimation of in vivo human brain-to-skull conductivity ratio with the aid of intracranial electrical simulation”, *Applied Physics Letters*, vol. 89, no. 22, 2006.

[56] B.W. Connors and M.J. Gutnick, “Intrinsic firing patterns of diverse neocortical neurons,” *Trends. Neurosci.*, vol. 13, no.3, pp. 99-104, March 1990.

[57] W.J**.** Gao and Z.H. Zheng, **“**Target-specific differences in somatodendritic morphology of layer V pyramidal neurons in rat motor cortex,” *J. Comp. Neurol.*, vol. 476, no.2, pp. 174–185, Aug. 2004.

[58] M. S. Hämäläinen and R. J. Ilmoniemi, “Interpreting magnetic fields of the brain: minimum norm estimates,” *Med. Biol. Eng. Comput.*, vol. 32, no.1, pp. 35-42, Jan. 1994.

[59] J. Wallerius, L. J. Trejo, R. Matthew, R. Rosipal, and J.A. Caldwell, “Robust feature extraction and classification of EEG spectra for real-time classification of cognitive state,” *11th HCI Int. Conf, Las Vegas, Nevada, July 2005.*

[60] K.Wendel and J. Malmivuo, “Correlation between live and post mortem skull conductivity measurements,” *in Proc. 28th IEEE EMBS Ann. Int. Conf., Aug. 30-Sept. 3, 2006, N.Y., USA*, vol. 1, no. 2, pp. 4285-4288.

[61] K. Wendel, J. Väisänen, G. Seemann, J. Hyttinen, and J. Malmivuo, "The influence of age and skull conductivity on surface and subdermal bipolar EEG leads,"*Comp. Intell. Neurosci.*, vol. 2010, Article ID 397272 , Jan. 2010.

[62] R. Hoekema, G.J.M. Huiskamp, G. H. Wieneke, F. S. S. Leijten, C.W.M. van Veelen, P.C. van Rijen, and A.C. van Huffelen, “Measurement of the conductivity of skull, temporarily removed during epilepsy surgery,” *Brain Topography*, vol. 16, no. 1, pp. 29–38, 2003.

[63] S. Lew, C.H. Wolters, A. Anwander, S. Makeig, and R.S. MacLeod, “Low resolution conductivity estimation to improve source localization," *in New Frontiers in Biomagnetism: Proc. 15th Int. Conf. Biomagnetism, Vancouver, BC, Canada, August 21-25, 2006.* International Congress Series, vol. 1300, pp.149-152, 2007.

[64] C.H. Wolters, S. Lew, R.S. MacLeod, and M.S. Hamalainen, ”Combined EEG/MEG source analysis using calibrated finite element head models,” *in Proc. 44th Ann. Meeting, DGBMT, Rostock Warnem¨unde, Germany, Oct.5- 8, 2010.*

[65] B. R. Yitembe, G. Crevecoeur, R. Van Keer, and L. Dupr´e, “Reduced conductivity dependence method for increase of dipole localization accuracy in the EEG inverse problem,” *IEEE Trans. Biomed. Eng.*, vol. 58, no. 5, pp. 1430 – 1440, Jan. 2011.
[66] H. S. Mir, J.D. Sahr, G. F. Hatke, and C. M. Keller, “Passive direction finding using an airborne sensor array in the presence of manifold perturbations,” *IEEE Trans. Signal Process*., vol. 55, no.1, pp. 2486 - 2496, Jan. 2007

VITA

Tahereh Sadat Zarghami was born on July 16, 1985, in Tehran, Iran. She was admitted to the Exceptional Talents' High School (Farzanegan) in Iran in 1999. She got her pre-university certificate from the same institute in 2003. The same year she passed the competitive entrance exam of university in Iran and was admitted to Tehran Polytechnic (Amirkabir) University in the field of Biomecial Engineering. She ranked third in her class at the end of her first year of education. In 2004 her family moved to UAE and Tahereh joined American University of Sharjah (AUS). She graduated cum laude in 2008 with a Bachelor of Science degree in Electrical Engineering, and a minor in Mathematics. Tahereh returned to AUS in 2010 to pursue her Masters degree. She received a graduate teaching assistantship package from the Electrical Department. In 2012 she was awarded the Master of Science degree in Electrical Engineering from AUS.